

**Monte Carlo Study of the Magnetic Flux  
Lattice Fluctuations in High- $T_c$   
Superconductors**

by

Cédric Bény

A thesis  
presented to the University of Waterloo  
in fulfillment of the  
thesis requirement for the degree of  
Master of Science  
in  
Physics

Waterloo, Ontario, Canada, 2005

©Cédric Bény 2005

## AUTHOR'S DECLARATION FOR ELECTRONIC SUBMISSION OF A THESIS

I hereby declare that I am the sole author of this thesis. This is a true copy of the thesis, including any required final revisions, as accepted by my examiners.

I understand that my thesis may be made electronically available to the public.

## Abstract

By allowing to measure the magnetic field distribution inside a material, muon spin rotation experiments have the potential to provide valuable information about microscopic properties of high-temperature superconductors. Nevertheless, information about the intrinsic superconducting properties of the material is masked by random thermal and static fluctuations of the magnetic field which penetrates the material in the form of vortices of quantized magnetic flux. A good understanding of the fluctuations of those vortices is needed for the correct determination of intrinsic properties, notably the coherence length  $\xi$ , and the field penetration depth  $\lambda$ . We develop a simulation based on the Metropolis algorithm in order to understand the effect, on the magnetic field distribution, of disorder- and thermally-induced fluctuations of the vortex lattice inside a layered superconductor.

Our model correctly predicts the melting temperatures of the  $\text{YBa}_2\text{Cu}_3\text{O}_{6.95}$  (YBCO) superconductor but largely underestimates the observed entropy jump. Also we failed to simulate the high field disordered phase, possibly because of a finite size limitation. In addition we found our model unable to describe the first-order transition observed in the highly anisotropic  $\text{Bi}_2\text{Sr}_2\text{CaCu}_2\text{O}_{8+y}$ .

Our model predicts that for YBCO, the effect of thermal fluctuations on the field distribution is indistinguishable from a change in  $\xi$ . It also confirms the usual assumption that the effect of static fluctuations at low temperature can be efficiently modeled by convolution of the field distribution with a Gaussian function. However the extraction of  $\xi$  at low fields requires a very high resolution of the field distribution because of the low vortex density.

## **Acknowledgements**

I would like to thank my supervisor Michel Gingras for his advice, enthusiasm and involvement in this project and also for allowing me to come back here in Waterloo where I am having a great scientific experience. I also wish to thank my co-supervisor Thomas Devereaux for our discussions, his accessibility and for his patience toward my enquiries. I enjoyed working in this group thanks to the friendly atmosphere created by all its members.

# Contents

<b>1</b>	<b>Introduction</b>	<b>1</b>
1.1	Theory . . . . .	3
1.1.1	The penetration depth . . . . .	3
1.1.2	The coherence length . . . . .	4
1.1.3	Magnetic vortices . . . . .	6
1.1.4	The flux line lattice . . . . .	9
1.1.5	Layered superconductors . . . . .	13
1.1.6	Muon Spin Rotation technique . . . . .	15
<b>2</b>	<b>Questions</b>	<b>21</b>
2.1	Goals . . . . .	30
<b>3</b>	<b>Model</b>	<b>33</b>
3.1	The penetration depth . . . . .	35
3.2	Disorder . . . . .	35
3.2.1	Disorder strength . . . . .	38
3.2.2	Disorder lengthscales . . . . .	39
3.3	Magnetic field . . . . .	42
3.3.1	General expression . . . . .	42
3.3.2	Vortex lattice . . . . .	47
3.3.3	Thermal fluctuations average . . . . .	47
3.4	Properties of the model . . . . .	49
3.4.1	Scaling . . . . .	49

3.4.2	Continuous lines regime . . . . .	56
3.4.3	2D Boson model equivalent . . . . .	57
3.4.4	Rescaling . . . . .	58
3.4.5	Logarithmic interaction regime . . . . .	60
<b>4</b>	<b>Simulation</b>	<b>61</b>
4.1	Correlation times . . . . .	61
4.2	Simulation times scaling . . . . .	64
4.3	Multihistogram method . . . . .	64
4.4	Observables . . . . .	66
4.4.1	Bragg peaks . . . . .	66
4.4.2	Hexatic order parameter . . . . .	67
4.4.3	Magnetic field calculation . . . . .	68
4.5	Disorder Implementation . . . . .	69
4.6	Tabulation of the interactions . . . . .	71
<b>5</b>	<b>Results I (clean)</b>	<b>73</b>
5.1	Decoupled lines . . . . .	73
5.2	Decoupled layers . . . . .	74
5.2.1	Conversion to other parameters . . . . .	85
5.3	Melting with constant $\lambda$ . . . . .	86
5.3.1	Three types of transitional behaviours . . . . .	87
5.3.2	Layer decimation . . . . .	92
5.3.3	Order of the transition . . . . .	96
5.3.4	Re-entrant melting . . . . .	99
5.4	On the number of layers . . . . .	102
5.5	Melting of the full clean system . . . . .	104
5.5.1	Entropy jump . . . . .	114
5.5.2	Field distribution (clean system) . . . . .	116
<b>6</b>	<b>Results II (dirty)</b>	<b>129</b>
6.1	Decoupled layers . . . . .	129

6.2	The full dirty system . . . . .	133
6.2.1	Field distribution (dirty system) . . . . .	140
<b>7</b>	<b>Conclusions</b>	<b>143</b>
7.1	Avenues for future work . . . . .	146
<b>A</b>	<b>Multihistogram method, derivation</b>	<b>149</b>
A.1	Bayesian statistical inference . . . . .	149
A.2	Derivation . . . . .	151



# List of Figures

1.1	Generic Phase Diagram of a Type II Superconductor . . . . .	11
1.2	An artist's impression of the vortex and pancake lattice . . . . .	14
1.3	$\mu$ SR experiment setup . . . . .	16
1.4	Field distribution of a perfect lattice . . . . .	19
2.1	Sonier's experiments . . . . .	23
2.2	Tentative Phase Diagram of a clean High- $T_c$ Superconductor . . . . .	27
2.3	Tentative Phase Diagram of a disordered High- $T_c$ Superconductor . . . . .	29
3.1	Interaction between pancakes . . . . .	34
3.2	Experimental $\lambda(T)$ for YBCO and BSCCO . . . . .	35
3.3	Bragg glass lengthscales estimation . . . . .	41
3.4	Layer decimation . . . . .	51
3.5	Layer decimation, interactions . . . . .	55
3.6	Replacing piles by continuous lines . . . . .	56
3.7	Relation between $b,t$ and $B,T$ . . . . .	59
4.1	Time series for the 2D system . . . . .	62
4.2	Time series for the 3D system . . . . .	63
5.1	Free line . . . . .	74
5.2	2D phase diagram . . . . .	76
5.3	2D phase diagram; observables . . . . .	77
5.4	2D transition scaling in the logarithmic regime . . . . .	80
5.5	2D transition scaling in the exponential regime . . . . .	81

5.6	2D phase transition histograms . . . . .	82
5.7	$\psi_6$ correlation function . . . . .	84
5.8	2D phase diagram, adapted to YBCO parameters . . . . .	85
5.9	8 layers melting . . . . .	88
5.10	Line wandering exponent through 3D melting . . . . .	89
5.11	Layer decoupling at high field (clean system) . . . . .	91
5.12	Dependance of observables on the number of layer . . . . .	92
5.13	Dependance of transition temperature on the number of layer . . . . .	93
5.14	100 layers melting . . . . .	94
5.15	Test of layer decimation . . . . .	95
5.16	3D transition histograms . . . . .	96
5.17	3D transition scaling . . . . .	97
5.18	Observables versus temperature for 3D melting with $n = 5$ . . . . .	98
5.19	Simulation snapshot prior to dubious reentrant melting . . . . .	100
5.20	Observables at extremely low field: reentrant melting? . . . . .	101
5.21	Simulation validity regimes for YBCO and BSCCO . . . . .	105
5.22	Phase diagram for YBCO from simulation and experiments . . . . .	106
5.23	Dependence of $T_m$ on $\lambda$ . . . . .	107
5.24	Observables versus temperature for 3D melting . . . . .	108
5.25	Phase diagram for BSCCO . . . . .	109
5.26	Entropy jump in YBCO . . . . .	110
5.27	Energy histograms, calculation of the entropy jump . . . . .	111
5.28	Heat capacity peaks, calculation of the entropy jump . . . . .	112
5.29	Observables for the series used to compute $\Delta S$ . . . . .	113
5.30	Observables for the clean simulation used to compute $n(B)$ . . . . .	118
5.31	$\alpha$ , clean system, comparison to experiment . . . . .	119
5.32	Fitting method . . . . .	120
5.33	Fitted field distributions (clean system) . . . . .	122
5.34	Fitted field distributions, zoom (clean system) . . . . .	123
5.35	Magnetic field distribution across the melting transition . . . . .	124
5.36	Result of fitting the field for the clean system . . . . .	125

5.37	Comparison between $\lambda_{\text{eff}}$ and experiments . . . . .	126
6.1	Order parameter for the dirty 2D system . . . . .	130
6.2	Observables for the dirty 2D system prior to annealing . . . . .	131
6.3	Annealing, order parameters . . . . .	133
6.4	Observables at t=4K, dirty system . . . . .	134
6.5	Field distribution at 4K (dirty system) . . . . .	135
6.6	Fitted parameters . . . . .	136
6.7	Fitted parameters, compared to experiments . . . . .	137
6.8	Position correlation function (dirty system) . . . . .	138

# Chapter 1

## Introduction

Superconductivity is a widespread low-temperature property of matter. It has been observed in many metals and compounds of various nature. Its actual and potential applications drive research toward finding superconductors working under wider conditions, notably higher temperatures. It is conjectured that a variety of different microscopic phenomena could be the cause of superconductivity, even though only one of them is well understood through the Bardeen-Cooper-Schrieffer (BCS) theory [1] which applies mostly to elemental metals. Superconductivity is not understood in the copper-oxide compounds (cuprates) which show the highest superconducting temperatures yet observed. For instance the most studied cuprates are  $\text{YBa}_2\text{Cu}_3\text{O}_{7-y}$  (YBCO),  $\text{Bi}_2\text{Sr}_2\text{CaCu}_2\text{O}_{8+y}$  (BSCCO) and  $\text{La}_{2-x}\text{Sr}_x\text{CuO}_4$  (LSCO). Many experiments and theoretical work are devoted to the understanding of the mechanisms underlying this exotic superconductivity.

Aside from predicting the basic properties of superconductivity like the Meissner effect (expulsion of the magnetic field) and the zero resistivity, the BCS theory makes important predictions on the dependence of two phenomenological observables on the magnetic field and temperature. The coherence length  $\xi$  and the field penetration depth  $\lambda$  are the typical distances over which respectively the local order parameter for superconductivity and the magnetic field can substantially vary. Observing variations of these parameters as function of average magnetic field or temperature which depart from the BCS behaviour can give important information about alternatives to the BCS theory.

Both parameters can be measured through various experimental methods. One way

to obtain them is to measure their effects on the magnetic field structure inside the superconductor. High-temperature superconductors in the presence of a magnetic field are pierced by non-superconducting tubes carrying magnetic flux. Each of those vortices imposes strong variations of the magnetic field whose features can reveal information about the physics underlying superconductivity. In particular those features can reveal the coherence length  $\xi$  and the field penetration depth  $\lambda$ .

Muon-spin rotation ( $\mu$ SR) experiments allow to measure those local variations of the magnetic field inside the superconductor. Unfortunately, the information about  $\xi$  and  $\lambda$  is hidden in the overall magnetic field distribution together with the particular geometry of the flux lattice, including the effects of its static and dynamical fluctuations. Such fluctuations have been studied primarily because the thermodynamics and pinning of the flux lattice is important for understanding the overall qualitative properties in a magnetic field and in particular the effective macroscopic conductivity of these materials. In this work we have another motivation for understanding those fluctuations, for this knowledge is needed for a quantitatively accurate analysis of the  $\mu$ SR experiments. Notably, those experiments have observed unconventional variations of the vortex core radius and field penetration depth as a function of field and temperature. We want to develop a realistic simulation of a disordered high-temperature layered superconductor in order to reproduce and understand the important features of the phase diagram of the flux lattice, as well as the effect of the lattice's fluctuations on the magnetic field distribution as the system approaches highly disordered phases.

In the rest of this chapter we introduce the basic notions that will be used in the rest of this document. In Chapter 2 we expose the problems that we want to address and review the current knowledge about the phase diagram associated with the flux lattice. Chapter 3 describes the model used and the basic properties that we can deduce analytically. In Chapter 4 we explain some tricky technical aspects of the simulation implementing the model. In chapter 5 we present the results obtained for simulations which do not include a model of intrinsic disorder, which is left to Chapter 6. We conclude in Chapter 7.

## 1.1 Theory

Superconductivity is a thermodynamic state of matter characterized by its electromagnetic properties. A superconductor has no resistivity and expels the magnetic field from its bulk (Meissner effect). The magnetostatic phenomenology is well described by replacing Ohm's law by the London equations for the microscopic electric field  $\mathbf{E}$ , magnetic field  $\mathbf{B}$  and current density  $\mathbf{J}$  [2].

$$\mathbf{E} = \Lambda \frac{\partial}{\partial t} \mathbf{J} \quad (1.1)$$

$$\mathbf{B} = -\Lambda \mathbf{curl} \mathbf{J} \quad (1.2)$$

$$(1.3)$$

where  $\Lambda$  is a constant. This pair of equations together with Maxwell's equations correctly describes the main properties of superconductors. Equation 1.1 describes perfect conductivity since a non-zero electric field accelerates electrons instead of just maintaining a steady current. Equation 1.2 is related to the screening of the magnetic field (Meissner effect) as the following analysis indicates.

### 1.1.1 The penetration depth

We consider a superconductor inside an applied magnetic field. At the interface between the vacuum and the superconductor, for the situation to be steady, the charges must circulate parallel to the surface. A simple ansatz is that of a current density uniform under the surface but with an intensity decaying within the material. Because the fields must be continuous this will always be true close enough to a continuous surface. Through Equation 1.2 this implies that the magnetic field must also be parallel to the surface but perpendicular to the current density. Furthermore, from  $\mathbf{curl} \mathbf{B} = \mu_0 \mathbf{J}$  and Equation 1.2, we deduce  $\mathbf{B} = -\frac{\Lambda}{\mu_0} \mathbf{curl} \mathbf{curl} \mathbf{B}$ , which can be rewritten in terms of the magnetic field magnitude as a function of the distance to the interface within the superconductor as  $B(x) = \frac{\Lambda}{\mu_0} \frac{d^2}{dx^2} B(x)$ . Therefore the field decays inside the superconductor on a lengthscale

$$\lambda = \sqrt{\frac{\Lambda}{\mu_0}}. \quad (1.4)$$

$\lambda$  is called the penetration depth.

The above considerations are not enough to justify London's equations. Both equations 1.1 and 1.2 can be derived by assuming that superconductivity is a property of a quantum mechanical ground state. In the absence of an applied field one expect that the ground state of quantum mechanical carriers of mass  $m$  and charge  $q$  interacting with a classical vector potential  $\mathbf{A}$  have to have a zero canonical momentum  $\langle \hat{\mathbf{p}} \rangle = \langle m\hat{\mathbf{v}} + q\mathbf{A} \rangle = 0$  so that  $\mathbf{v} = \langle \hat{\mathbf{v}} \rangle = -q\mathbf{A}/m$ . Therefore  $\mathbf{J} = nq\mathbf{v} = -nq^2\mathbf{A}/m$ , where  $n$  is the density of carriers. Taking the curl on both sides yields the second London equation. Taking the time derivative on both sides yields the first London equation provided an adequate choice of gauge  $\text{div}\mathbf{A} = 0$  (the London gauge). Therefore

$$\Lambda = \frac{m}{nq^2}. \quad (1.5)$$

The London equations can also be written

$$\boxed{\mathbf{J} = -\frac{1}{\lambda^2\mu_0}\mathbf{A}} \quad (1.6)$$

### 1.1.2 The coherence length

The London theory cannot be used to model the thermodynamics of the transition between a superconductor and a normal conductor. In order to go further one has to introduce a complex order parameter  $\psi(x)$  whose modulus squared gives a local density of carriers  $n(x) = |\psi(x)|^2$ . The field is governed by an equation which reduces to the London equations when  $n(x)$  is constant. In such case the constant value of  $n(x)$  is the density of carriers as introduced in the discussion in Section 1.1.1.

The spacial distribution of the field  $\psi$  is governed by the variational free energy [3]

$$f = \alpha|\psi|^2 + \frac{\beta}{2}|\psi|^4 + \frac{1}{2m} |(-i\hbar\nabla + q\mathbf{A})\psi|^2 + \frac{1}{2\mu_0}(H - \mathbf{curl}\mathbf{A})^2 \quad (1.7)$$

where  $H$  the imposed external magnetic field. The form of this free energy was introduced by Ginzburg and Landau (GL) prior to the BCS theory explaining superconductivity at a microscopic level. It is derived by symmetry arguments with the assumption of a second

order transition and for temperatures close to the transition temperature. Like the London equations it makes few microscopic assumptions.

In the absence of electromagnetic field or gradient the free energy reduces to

$$f = \alpha|\psi|^2 + \frac{\beta}{2}|\psi|^4$$

which has a single minimum at  $\psi = 0$  if  $\alpha > 0$  and degenerate minima with  $|\psi_\infty|^2 \doteq |\psi|^2 = -\alpha/\beta$  when  $\alpha < 0$ . We call this  $\psi_\infty$  (infinity) because it is the asymptotic value of the order parameter that we expect to find in the bulk of the superconductor far from disturbances caused by boundaries.

The minimum free energy is given by variations of the spatial integral of  $f$  with respect to the variables  $\psi$  and  $\mathbf{A}$ . This gives respectively the two Ginzburg-Landau equations

$$\alpha\psi + \beta|\psi|^2\psi + \frac{1}{2m}(-i\hbar\nabla + q\mathbf{A})^2\psi = 0 \quad (1.8)$$

$$-\frac{q}{m}|\psi|^2(\hbar\nabla \arg \psi + q\mathbf{A}) = \frac{1}{\mu_0}\mathbf{curl\,curl\,A}. \quad (1.9)$$

as well as boundary conditions that we will not discuss here. See Ref. [4] for more details. The field  $\arg \psi$  at position  $\mathbf{x}$  is the *argument* of the complex number  $\psi(\mathbf{x})$ . It is also called the *phase* of the order parameter  $\psi$  at position  $\mathbf{x}$ . It can be defined as a real number such that  $\psi(\mathbf{x}) = |\psi(\mathbf{x})|\exp(i \arg \psi)$ . This definition is ambiguous since multiple of  $2\pi$  can be freely added to  $\arg \psi(\mathbf{x})$  without changing  $\psi(\mathbf{x})$ . In Equation 1.9 it is assumed that a choice has been made such that the field  $\arg \psi$  is continuous, otherwise the gradient would not be defined everywhere.

If we want to define a current density  $\mathbf{J}$  through its effect on the field  $\mathbf{B}$  via the Maxwell equation  $\mu_0\mathbf{J} = \mathbf{curl\,B} = \mathbf{curl\,curl\,A}$  then Equation 1.9 defines what the current density is in terms of the field  $\psi$ :

$$\mathbf{J} = -\frac{q}{m}|\psi|^2(\hbar\nabla \arg \psi + q\mathbf{A}) \quad (1.10)$$

Equation 1.9 embodies the inhomogeneous (magnetostatic) Maxwell equations in this theory. The homogeneous ones are guaranteed by the fact that we are using a vector potential.

The first equation can be linearized for small variations around the bulk  $\psi_\infty$  and for zero field, yielding

$$\nabla^2 g = \frac{4m\alpha}{\hbar^2}g$$

where  $g(\mathbf{x}) = 1 - \psi(\mathbf{x})/\psi_\infty$ . A solution with translational symmetry in two directions perpendicular to the direction of component  $x$  is

$$g(x) = g(0) e^{-\frac{2\sqrt{m\alpha}}{\hbar} x}$$

Therefore the order parameter varies over a typical lengthscale

$$\boxed{\frac{\xi}{\sqrt{2}} = \frac{\hbar}{2\sqrt{m\alpha}}} \quad (1.11)$$

which defines the coherence length  $\xi$ .

Since when  $\psi$  is homogeneous ( $\psi = \psi_\infty = -\alpha/\beta$ ) we recover London's equations, we can relate  $\lambda$  to  $\alpha$  by comparing equations 1.6 and 1.10:

$$\lambda^2 = -\frac{m\beta}{\mu_0 q^2 \alpha} \quad (1.12)$$

At the transition,  $\alpha = 0$  implies that the coherence length  $\xi$  and the penetration depth  $\lambda$  must diverge.

### 1.1.3 Magnetic vortices

The lengthscale  $\lambda$  and  $\xi$  are important for characterizing the superconductor near a normal ( $\psi = 0$ ) region. Indeed if  $\xi/\sqrt{2} > \lambda$  then, at the interface between the superconductor and the normal material, the order parameter rises more slowly than the magnetic field decays, which means that there is a region with low order parameter and high field, and therefore a higher local free energy density than in the bulk. Hence such interfaces cost energy and are not favoured when the total free energy is minimized. This characterizes type I superconductors. Conversely boundaries are favoured when  $\xi/\sqrt{2} < \lambda$ , defining the type II superconductors (see Ref. [5] for more details). Here we are interested in extreme type II superconductors for which  $\lambda \gg \xi$ .

Let us integrate Equation 1.9 over a closed loop  $\partial\Omega$ . Continuity of the phase of the order parameter requires that there exists an integer  $N$  such that

$$\oint_{\partial\Omega} \nabla \arg \psi \cdot d\mathbf{s} = 2\pi N \quad (1.13)$$

therefore (1.9) yields

$$\oint_{\partial\Omega} \mathbf{A} \cdot d\mathbf{s} = -\frac{1}{q} \oint_{\partial\Omega} \frac{m}{q|\psi|^2} \mathbf{J} \cdot d\mathbf{s} + \Phi_0 N \quad (1.14)$$

or, using Stokes' theorem

$$\int_{\Omega} \mathbf{B}(\mathbf{x}) \cdot d\mathbf{a} = - \int_{\Omega} \mathbf{curl} \left[ \frac{m\mathbf{J}(\mathbf{x})}{q^2 n(\mathbf{x})} \right] \cdot d\mathbf{a} + \Phi_0 N \quad (1.15)$$

with

$$\Phi_0 \doteq \frac{2\pi\hbar}{2e}$$

defining the fluxoid quantum. We used  $q = 2e$ ; the charge of the carriers is twice the charge of the electron. The integral of  $B$  is the total magnetic flux through the surface  $\Omega$ . If London's equations are valid ( $\psi(\mathbf{x})$  constant on  $\Omega$ ) we get the case  $N = 0$  as shown by Equation 1.13. Equation 1.15 shows that the only contribution to the magnetic flux from the order parameter's phase comes from  $N$ . Therefore variations in the phase can only make the total magnetic flux inside a loop deviate by integer multiple of  $\Phi_0$ . This is usually interpreted by stating that, if there is a local disturbance somewhere in the superconductor which is otherwise uniform, the magnetic flux inside a loop encircling the disturbance will asymptotically tend to an integer multiple of  $\Phi_0$  as the radius grows, for the term depending on  $\mathbf{J}(\mathbf{x})$  in 1.14 will tend to zero. However it is not obvious, without seeing an actual solution for those fields, why this term should vanish.

Since normal-superconducting interfaces can be favoured in a type II superconductor, then a sufficiently strong field will penetrate inside the superconductor and locally destroy superconductivity in order to create a maximum of such surfaces. The way in which this can happen is constrained by the flux quantization.

Equation 1.15 is satisfied by any field  $\mathbf{B}$  satisfying the local equation

$$\mathbf{B}(\mathbf{x}) = -\mu_0\lambda^2 \mathbf{curl} \mathbf{J}(\mathbf{x}) + \Phi_0 N \delta(\mathbf{r}) \hat{\mathbf{z}} \quad (1.16)$$

where  $\hat{\mathbf{z}}$  is a unit vector and  $\mathbf{r} = \mathbf{x} - (\mathbf{x} \cdot \hat{\mathbf{z}}) \hat{\mathbf{z}}$  the distance between  $\mathbf{x}$  and the line of direction  $\hat{\mathbf{z}}$  passing through the origin.

This models the case where a flux  $N\Phi_0$  is allowed to penetrate by destroying superconductivity only on a line of direction  $\hat{\mathbf{z}}$ . This is a sensible ansatz only when the lengthscale  $\xi$  over which the order parameter can vary is much shorter than  $\lambda$ :  $\xi \ll \lambda$ .

Using Maxwell's equation  $\mathbf{curl} \mathbf{B} = \mu_0 \mathbf{J}$ , we get

$$\lambda^2 \mathbf{curl} \mathbf{curl} \mathbf{B}(\mathbf{x}) + \mathbf{B}(\mathbf{x}) = N\Phi_0 \delta(\mathbf{r}) \hat{\mathbf{z}}.$$

Through a vector identity and  $\mathbf{div} \mathbf{B}(\mathbf{x}) = 0$ , this is equivalent to

$$-\lambda^2 \nabla^2 \mathbf{B}(\mathbf{x}) + \mathbf{B}(\mathbf{x}) = N\Phi_0 \delta(\mathbf{r}) \hat{\mathbf{z}}. \quad (1.17)$$

The Fourier transform

$$\lambda^2 \mathbf{k}^2 \mathbf{B}(\mathbf{k}) + \mathbf{B}(\mathbf{k}) = N\Phi_0 \delta(k_z) \hat{\mathbf{z}}$$

can be easily solved:

$$\mathbf{B}(\mathbf{k}) = \frac{N\Phi_0 \hat{\mathbf{z}}}{1 + \lambda^2 \mathbf{k}^2} \delta(k_z). \quad (1.18)$$

(Because of the Fourier transform, the delta function over  $\mathbf{r}$  in Equation 1.17 has been replaced by a constant. Also, a delta function over  $z$  appeared because of the independence of the right-hand side of 1.17 on  $z$ .) The inverse Fourier transform of Equation 1.18 is expressed with the zero-order Hankel function of imaginary argument, also called the zeroth-order modified Bessel function of the second kind  $K_0$  [5]:

$$\boxed{\mathbf{B}(\mathbf{x}) = \frac{N\Phi_0}{2\pi\lambda^2} K_0\left(\frac{r}{\lambda}\right) \hat{\mathbf{z}}} \quad (1.19)$$

where  $r = |\mathbf{x}|$ .

This function  $K_0(x)$  has simple limiting behaviours. When  $x$  is small it behaves like a logarithm function

$$K_0(x) \sim -\ln(x) \quad \text{when } x \ll 1. \quad (1.20)$$

When  $x$  is large it behaves mainly like an exponential function

$$K_0(x) \sim \frac{\exp(-x)}{x} \quad \text{when } x \gg 1. \quad (1.21)$$

The field structure described by Equation 1.19 is called a *vortex*. We will always implicitly assume  $N = 1$ . It carries a quantum of magnetic flux  $\Phi_0$  in the direction  $\hat{\mathbf{z}}$  and

has a cylindrical symmetry along  $\hat{\mathbf{z}}$ . This magnetic flux is maintained by a current density given by

$$\mathbf{J}(\mathbf{x}) = \frac{\Phi_0}{2\pi\mu_0\lambda^2} K_1\left(\frac{r}{\lambda}\right) \hat{\theta}$$

which revolves around the vortex center at  $r = 0$ .  $K_1$  is the first-order modified Bessel function of the second kind. It is linked to  $K_0$  through  $K_1(x) = -\frac{d}{dx}K_0(x)$ .

Later we will introduce another kind of vortex which has roughly the same structure but which is almost two-dimensional as it does not extent in the  $\hat{\mathbf{z}}$  direction. The word vortex will be used for both. Alternatively, when the distinction must be made clear, the above type of vortex will be called a vortex line for its cylindrical elongated shape while the new kind will be called a vortex pancake. Typically pancakes will form a pile on top of each other so as to make a shape looking approximatively like a vortex line (Section 1.1.5).

### 1.1.4 The flux line lattice

The vortex field 1.19 is a solution to the London and Maxwell equations which are linear. Adding source terms on the right hand side of Equation 1.16 can be solved by adding translated solutions of the type 1.19 [5]. Each added solution is said to describe an additional, independent vortex in the system.

One can show that there are temperatures and fields for which a type II superconductor reaches its ground state by allowing only vortices of minimum flux quantum  $N = 1$  [5]. Those vortices feel a repulsive interaction between each other. The interaction energy can be derived from the expression of the field energy plus the kinetic energy of the current:

$$U(\mathbf{u}) = \frac{1}{2} \int \left[ \frac{1}{\mu_0} \mathbf{B}^2(\mathbf{x}) + \mu_0 \lambda^2 \mathbf{J}^2(\mathbf{x}) \right] d\mathbf{x}$$

The second term is the kinetic energy density  $n\mathbf{v}^2(\mathbf{x})/2m$  where  $\mathbf{v}$  is derived from  $\mathbf{J}(\mathbf{x}) = nq\mathbf{v}(\mathbf{x})$  and  $\lambda$  introduced using equations 1.4 and 1.5.

Let us suppose that we have a field sum of the field of two vortices, both in the  $\hat{\mathbf{z}}$  direction but with one of them displaced by  $\mathbf{u}$ :  $B_{\text{tot}}(\mathbf{x})\hat{\mathbf{z}} = B(\mathbf{x})\hat{\mathbf{z}} + B(\mathbf{x} - \mathbf{u})\hat{\mathbf{z}}$ . Then the total energy is

$$U_{\text{tot}}(\mathbf{u}) = U_0 + \int \left[ \frac{1}{\mu_0} B(\mathbf{x})B(\mathbf{x} - \mathbf{u}) + \mu_0 \lambda^2 \mathbf{J}(\mathbf{x}) \cdot \mathbf{J}(\mathbf{x} - \mathbf{u}) \right] d\mathbf{x}$$

where  $U_0$  contains the terms which do not depend on  $\mathbf{u}$ . One recognizes a convolution. We would like to express this in Fourier space. First we note that if the integral is extended to infinity in the  $\hat{\mathbf{z}}$  direction then the result will be infinite, but if we cut it off the convolution theorem does not hold anymore in this direction. Therefore we apply the convolution only in the perpendicular direction. Given that the system is symmetric with respect to translations along  $\hat{\mathbf{z}}$  we can already guess that the integral along this direction will just make the energy proportional to the line segment length  $d$ . The rest is performed in two dimension in terms of  $\mathbf{k}_\perp = \mathbf{k} - (\mathbf{k} \cdot \hat{\mathbf{z}})\hat{\mathbf{z}}$ . Therefore, in terms of Fourier components with respect to  $\mathbf{u}$ , the interaction energy is

$$U(\mathbf{k}_\perp) = \frac{d}{\mu_0} B^2(\mathbf{k}_\perp) + d\mu_0\lambda^2 \mathbf{J}^2(\mathbf{k}_\perp)$$

with  $\mathbf{J}(\mathbf{k}) = \frac{1}{\mu_0} \mathbf{k} \times \mathbf{B}(\mathbf{k})$ , this becomes

$$U(\mathbf{k}_\perp) = \frac{d}{\mu_0} B^2(\mathbf{k}_\perp) (1 + \lambda^2 \mathbf{k}_\perp^2).$$

Using expression 1.18 for  $B(\mathbf{k})$ :

$$U(\mathbf{k}_\perp) = \frac{d}{\mu_0} \frac{\Phi_0^2}{1 + \lambda^2 \mathbf{k}_\perp^2}.$$

Going back to spatial components we get

$$U(\mathbf{u}) = \frac{d\Phi_0^2}{2\pi\mu_0\lambda^2} K_0 \left( \frac{|\mathbf{u}|}{\lambda} \right). \quad (1.22)$$

Because the fields add linearly, one can check that an arbitrary number of vortices will all interact through this same pair potential.

The ground state of this interaction is an hexagonal lattice of parallel vortex lines (Abrikosov lattice [5]). Since each vortex carries a fixed amount of magnetic flux, then the lattice constant  $a_0$ , the shortest separation between vortex lines, is directly related to the average magnetic field  $B$  inside the superconductor via

$$\boxed{\Phi_0 = \frac{\sqrt{3}}{2} B a_0^2} \quad (1.23)$$

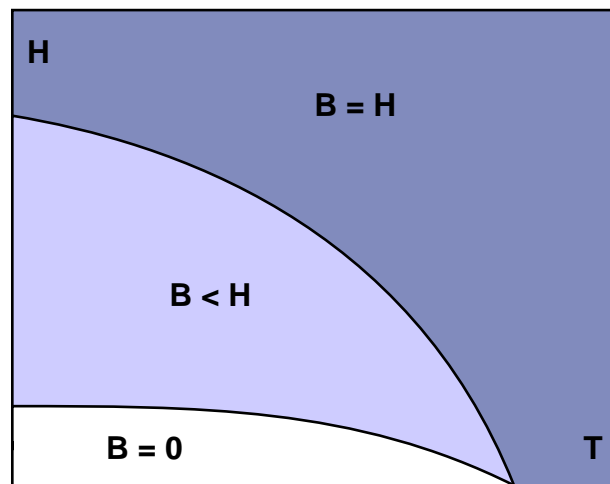


Figure 1.1: Generic Phase Diagram of a type II superconductor (labels assume  $\mu_0 = 1$ ).  $H$  is the external imposed magnetic field and  $B$  is the average induction field inside the superconductor. For a high-temperature superconductor the Meissner phase with  $B = 0$  occupies a very small portion of the phase diagram compared to the area spanned by the mixed phase  $B < \mu_0 H$ , so that we can assume  $B \approx \mu_0 H$  within the mixed phase.

Figure 1.1 shows the schematic generic phase diagram of type II superconductors. Small magnetic fields are fully expelled from the superconductor in the Meissner phase (white area). At higher values of the external field  $H$ , in the mixed phase, the magnetic field is allowed to enter the material and forms the Abrikosov lattice. The value of the external field which marks the transition between the Meissner and the mixed phase is the lowest critical field  $H_{C1}(T)$ . The field which mark the transition between the mixed phase and the normal (non-superconducting) phase is the upper critical field  $H_{C2}$ .

$H_{C1}$  is the field at which the energy gained from creating a vortex is just zero. The two competing contributions to the free energy are the energy gained by the introduction of the field associated with a vortex of length  $L$ :  $H_{C1}\Phi_0L$  and the energy lost by destroying superconductivity inside the vortex core as well as the energy of the fields an current around the vortex:  $\epsilon_1L$ . Therefore

$$H_{C1} = \frac{\epsilon_1}{\Phi_0}$$

But we do not know the core energy  $\epsilon_1$  per unit of vortex length. In the case of an extreme type II superconductor, the core energy can be neglected and  $\epsilon_1$  computed solely from the energy of field and currents [5]. This gives

$$H_{C1} \simeq \frac{\Phi_0}{\mu_0\lambda^2} \ln \frac{\lambda}{\xi}.$$

However this analysis is not correct for highly anisotropic superconductors [6] (see Section 1.1.5). For instance, at zero temperature for  $\text{YBa}_2\text{Cu}_3\text{O}_{7-y}$  (YBCO),  $\lambda \simeq 1300\text{\AA}$  [7] and  $\xi \simeq 20\text{\AA}$  [8] so that  $\mu_0H_{C1} \simeq 0.5 T$ . But experiments show much lower values of  $H_{C1}$ , for instance  $\mu_0H_{C1} \simeq 0.02T$  has been measured in [7].

The higher critical field  $H_{C2}$  can be computed by a linearized version of the GL equations 1.8 and 1.9. Indeed close to  $H_{C2}$  the order parameter  $\psi$  must be close to zero so that the higher order term  $|\psi|^4$  which makes the equations non-linear can be neglected. The result [5] is

$$H_{C2}(T) = \frac{\Phi_0}{2\pi\xi^2(T)}$$

This can be understood in the following way. Since  $\xi$  is the distance over which the order parameter can vary, and because the order parameter is always zero inside a vortex, then all superconducting regions must disappear when the average distance between vortices is

of the order of  $\xi$ . Using Equation 1.23 this argument directly gives the above relation up to a prefactor near unity. Because it depends on the physics close to the superconducting transition where the GL equations are the most reliable, the above expression reliably links  $\xi$  to  $H_{C2}$ .

### 1.1.5 Layered superconductors

Copper-oxide high temperature superconductors have highly anisotropic properties. They are composed of layers of copper-oxide planes which are believed to be the support of superconductivity. A model for those materials is that of a stack of thin superconducting layers separated by insulating material (The Lawrence-Doniach Model). The layers still interact via the Josephson effect [5] related to the tunneling of the complex order parameter through the insulating barrier. The Ginzburg Landau free energy (Equation 1.7) has to be modified in order to account for the anisotropy of this structure [3]:

$$f = \alpha|\psi|^2 + \frac{\beta}{2}|\psi|^4 + \frac{1}{2m_z} \left| \left( -i\hbar \frac{\partial}{\partial z} + q\mathbf{A}_z \right) \psi \right|^2 + \frac{1}{2m_\perp} |(-i\hbar\nabla_\perp + q\mathbf{A}_\perp)\psi|^2 + \frac{1}{2\mu_0} (H - \mathbf{curl} \mathbf{A})^2.$$

Through Equations 1.12 and 1.11, the masses  $m_z$  and  $m_\perp$  give rise to anisotropic penetration depths and coherence lengths. The anisotropy is quantified by the dimensionless parameter

$$\gamma^2 = \frac{m_\perp}{m_z}.$$

If we write  $\lambda_\perp$  and  $\lambda_z$  respectively for the penetration depth parallel and perpendicular to the layers (and similarly for  $\xi_\perp$  and  $\xi_z$ ) then we have

$$\gamma = \frac{\lambda_z}{\lambda_\perp} = \frac{\xi_\perp}{\xi_z} \gg 1.$$

In fact there can also be an important anisotropy between two directions inside a plane. For YBCO this anisotropy can reach 30% [9]. But we will not address this question here, and assume that  $\lambda_\perp$  and  $\xi_\perp$  are isotropic.

In the rest of the paper we consider a magnetic field applied perpendicular to the superconducting layers. Because  $\xi_z$  is much shorter than the spacing between layers the vortex cores are broken into ‘‘pancakes’’, one in each layer that the vortex crosses. But

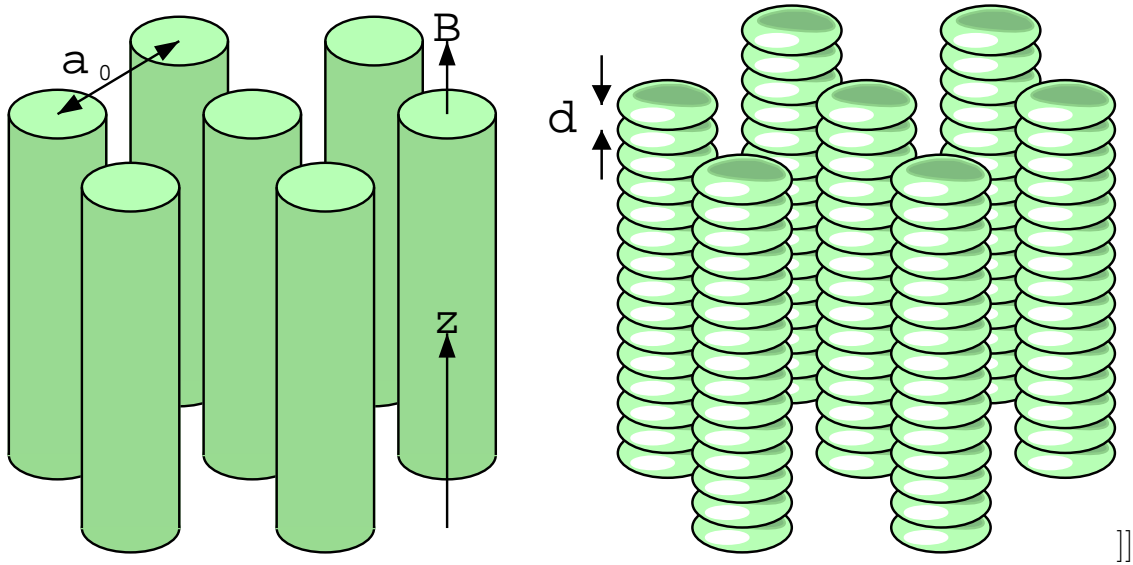


Figure 1.2: Artist's impression of the vortex line lattice (left) and pancake lattice in a layered superconductor (right). In the layered superconductor the vortex lines are replaced by *piles of pancakes*. The objects represented could symbolize the vortex core region over which the material is non-superconducting. On the other hand a surface of constant magnetic field would look like the left picture in both an isotropic and a layered superconductor because of the large value of  $\lambda$  compared to  $d$  (see Section 3.3).

since  $\lambda_z$  in turn is very large then the magnetic field around this point-like vortex is very close to that of the straight vortex line in an isotropic superconductor with penetration depth equal to  $\lambda_\perp$ : the field varies little between layers. In the rest of this document we will refer to  $\lambda_\perp$  and  $\xi_\perp$  respectively as  $\lambda$  and  $\xi$  because we will be concerned only by a field perpendicular to the layers for which those two quantities are the most important, as will be seen in Section 3.3.

When the pancakes are perfectly stacked into straight vortex lines perpendicular to the layers then the magnetic interaction between them is just equal to that derived above for vortices in an isotropic superconductor [10].

When the field is low, the pancakes belonging to different piles are far apart and interact weakly so that the coupling between pancakes in a pile is relatively strong and the piles behave like simple flux line in an isotropic superconductor. At high fields the effect is the converse and the layers become effectively decoupled.

### 1.1.6 Muon Spin Rotation technique

The  $\mu$ SR technique, for Muon Spin Rotation, Relaxation and Resonance, allows one to probe the magnetic field distribution inside a material, accounting for precise local variations of the field [11]. Muons are positively charged spin one-half particles (heavy leptons). They have a relatively short lifetime of 2.2 microseconds and decay into two neutrinos and one positron. The decay has the nice property that the positron is emitted with a higher probability in the instantaneous direction of the muon's spin at the time of desintegration. This means that detecting a positron at a certain position gives an indication—in a statistical sense—about the muon's spin direction at the time of the decay.

An experimental setup is schematically represented in Figure 1.1.6. Polarized muons are sent one by one into the sample. Since they are charged they interact with matter and gets immobilized somewhere inside the material, hopefully at random position<sup>1</sup>. Their spin precesses around the local magnetic field at a frequency proportional to the field's magnitude. When a muon decays, a positron is emitted with a higher probability in the

---

<sup>1</sup>It most likely binds to an oxygen atom, like a hydrogen ion [11]. But there is a high density of oxygen atoms in the lattice compared to the lengthscales  $\lambda$  or even  $\xi$ . Therefore the distribution must appear uniformly random.

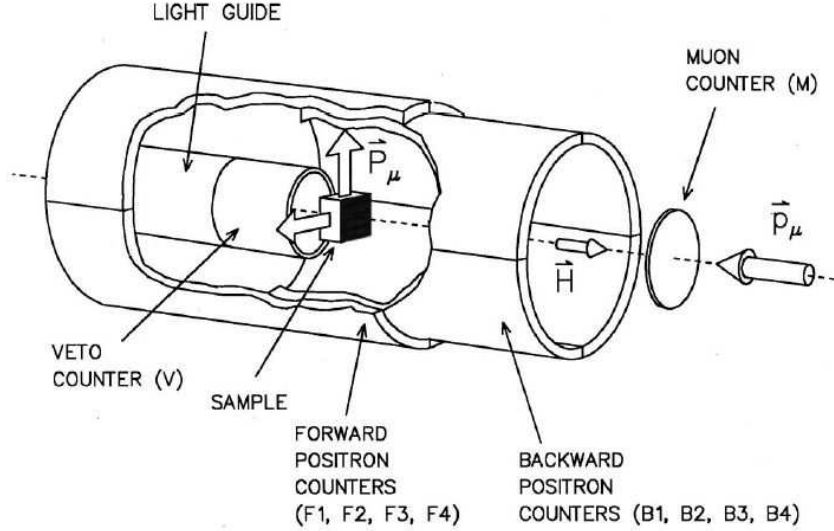


Figure 1.3: Schematic  $\mu$ SR experiment setup. The muons enter from the right. From Sonier *et al.* [11].

direction of the muon's spin. Therefore detection of the positron in a particular direction gives information about the spin direction at the moment of the decay.

Because the muon's rotation frequency is fixed by the local magnetic field amplitude, the probability for a positron detector in a particular direction to detect a positron is a periodic function of time. More precisely, the probability for a detection at a time  $t$  after the introduction of the muon is [11]

$$n(t) = N_0 e^{-t/\tau_\mu} (1 + A_0 p(t)) + C_0$$

where  $N_0$ ,  $A_0$  and  $C_0$  are constants,  $\tau_\mu$  is the lifetime of the muon and  $p(t)$  the spin component of the muon in this direction at the time  $t$ . This accounts for the probability distribution of emission of the positron as function of the direction away from the spin, as well as properties of the detectors. This formula can be inverted to obtain  $p(t)$ . Since this formula is linear in  $p(t)$ , then  $n(t)$  can be replaced by its average over many events  $N(t)$ , yielding an average of  $p(t)$  that we write as  $P(t)$ ; the  $\mu$ SR lineshape. In a magnetic field  $B$  the spin component is  $P(t) = \cos(\gamma_\mu B t + \phi)$  where  $\gamma_\mu/2\pi = 135.5342$  MHz/T [11].  $\gamma_\mu$

is the muon gyromagnetic ratio and  $\phi$  a constant. The lineshape is therefore

$$P(t) \propto \sum_i \cos(\gamma_\mu B(\mathbf{r}_i)t + \phi)$$

where  $B(\mathbf{r}_i)$  is the field at the position  $\mathbf{r}_i$  of the  $i$ th muon whose decay has been detected. For mathematical convenience we can replace  $P(t)$  by a complex function, implicitly assuming that we are referring to its real component. Alternatively the imaginary component can be interpreted as the lineshape extracted from another set of detectors 90 degrees away from the original ones [11]. This said, if we assume that the position  $r_i$  at which a muon lands is fully random, then we can replace the sum over events by an integral over space:

$$P(t) \propto \int e^{i\gamma_\mu B(\mathbf{x})t} d\mathbf{x}.$$

Given that the magnetic field distribution is

$$n(B) = \int \delta(B - B(\mathbf{x})) d\mathbf{x}$$

the lineshape can be expressed as

$$P(t) \propto \int_{-\infty}^{\infty} n(B) e^{i\gamma_\mu Bt} dB.$$

This means that  $P(t)$  is just the Fourier transform of  $n(B)$  and therefore the relation can be inverted:

$$n(B) \propto \int_{-\infty}^{\infty} P(t) e^{-i\gamma_\mu Bt} dt.$$

As it stands, this expression does not compare well to the result of the experiments. Random effects lead to a depolarization of the muon with time. For instance the muon's spin can interact with the nuclear magnetic fields. This effect can be handled by introducing a Gaussian prefactor in  $P(t)$  (see Ref. [12]):

$$P(t) \propto e^{-\frac{1}{2}\sigma^2 t^2} \int_{-\infty}^{\infty} n(B) e^{i\gamma_\mu Bt} dB. \quad (1.24)$$

This convolution results in the smearing of the field distribution. Indeed if the inverse Fourier transform is applied on this expression, then one gets a new effective ‘‘field distribution’’ given by the convolution of the original  $n(B)$  with a Gaussian:

$$\bar{n}(B) \propto \int dB' n(B') e^{\frac{\gamma_\mu^2}{2\sigma^2} (B-B')^2} \quad (1.25)$$

In addition it is assumed by experimentalists that other effects like the deviations of the lattice from the equilibrium hexagonal lattice [11] would also result in a convolution of the effective field distribution with a Gaussian. Let us call  $\sigma_{dip}$  the broadening parameter related to the nuclear field and  $\sigma_{dis}$  the one related to disorder in the vortex lattice. Both terms will combine together in quadrature, being independent broadening processes, in a single Gaussian term characterized by the parameter  $\sigma$  such that

$$\sigma^2 = \sigma_{dip}^2 + \sigma_{dis}^2$$

The final, broadened curve contains only information about the combined  $\sigma^2$ . Sonier [13] extracted the contribution of the nuclear moments from the fitted  $\sigma$  by assuming that  $\sigma_{dip}$  is the depolarization rate observed in the normal (non-superconducting) phase with the same  $\mu$ SR setup. Nevertheless this assumption probably neglects other effects such as the field variations caused by edge effects [14].

The question of whether or not the assumption that the parameter  $\sigma_{dis}$  accounts for the effect of the lattice fluctuations is one of the focus of this work and will be discussed in greater details in the next chapter.

Figure 1.4 shows the field distribution for a perfect lattice with the field profile given by Equation 1.19. This displays the typical feature of such a distribution. It is asymmetric, with a long tail extending to high fields. The peak corresponds to the saddle point at the midpoint between two vortices. The low field cutoff corresponds to the field minimum in the center of triangles formed by three neighbouring vortices. The high field cutoff corresponds to the maximum field in the vortex core and depends primarily on the cutoff  $\xi$ .

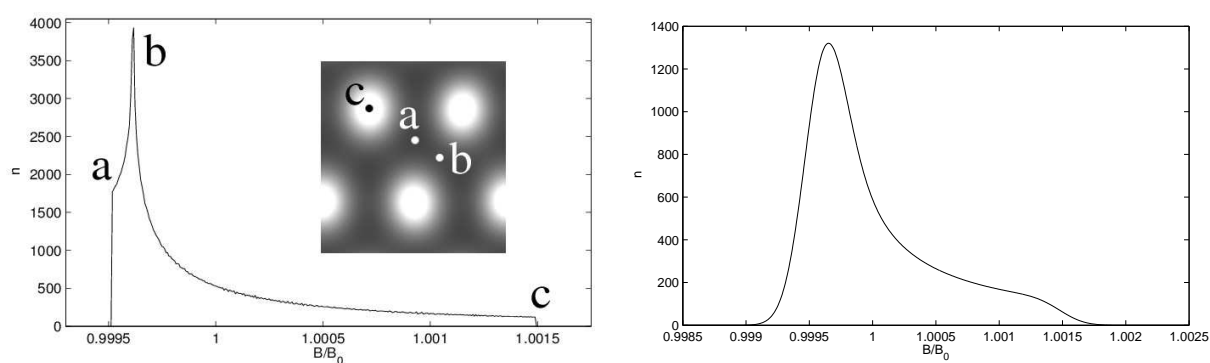


Figure 1.4: Field distribution for a perfect lattice for YBCO for average field  $B_0 = 10$  T respectively without and with a moderate Gaussian broadening. The field was numerically calculated from Equation 3.13. Notice the asymmetry of the curve and the three singularities. Inset: magnetic field intensity in a plane perpendicular to the field. The letters identify features of the field distribution to features of the lattice. The curve on the right is shown for providing an intuitive impression of the effect of the Gaussian broadening. The actual  $\sigma$  chosen is a typical value observed in the simulation (as in Section 6.2).



# Chapter 2

## Questions

Because it spans a wide range of applied magnetic field intensities and temperatures, the mixed phase of high temperature superconductors contains a phase diagram on its own. The unusual symmetries of the vortex “matter”, and the anisotropic layered structure of high- $T_c$  superconductors, give this diagram its complexity. In addition the disorder inside the underlying chemical lattice offers a way to study the interplay between static and thermal disorder on the vortex lattice. The properties of the vortex lattice has an important impact on the global properties of the superconductor of interest for an engineer, for its thermal fluctuations can destroy the infinite conductivity of the superconducting material [3].

Experimentally, the standard way to probe the magnetic field inside a material is to send in neutrons. Because they have no charge but a magnetic moment they can penetrate deep into the material and interact solely with the magnetic field. The wavelengths associated with the vortex lattice are bigger than other structures which can be studied with neutron scattering (like electronic spins ordering) and are therefore related to relatively small changes in the neutrons wavevectors. Therefore the technique adapted to the study of the vortex lattice is called Small Angle Neutron Scattering (SANS).

Another technique allows to observe the magnetic field structures directly in real space but only on the surface of the material. The Bitter decoration technique consists in laying magnetic particles on the surface and imaging their positions with an electron microscope [15]. The particles gather on different regions depending on the local magnetic field in-

tensity; revealing the surface field structure where the vortices emerge out of the material. Unfortunately it yields little information on the magnetic field variations between vortices. Furthermore it cannot provide a good indication of what happens in the bulk because of strong surface effects [16]. The same point is true of other surface imaging techniques like STS (Surface Tunneling Spectroscopy).

The  $\mu$ SR techniques distinguishes itself from a scattering experiment by the fact that the muons probe directly the local magnitude of the magnetic field instead of global periodic properties. It also differs from the Bitter decoration experiments because it probes directly the bulk of a sample. Furthermore it yields not only information on the positions of the vortices but also information on the way the magnetic field varies between vortices. The  $\mu$ SR technique has been used in order to extract both types of information. For instance Riseman *et al.* [17], Sonier *et al.* [18] and Kadono *et al.* [19] used the technique to measure variations of the magnetic field between vortices in a lattice, while Sonier *et al.* in Ref.[20] and Aegerter *et al.* [21] focused their interest on the vortex lattice configuration.

The  $\mu$ SR technique is comparable to the NMR (Nuclear Magnetic Resonance) technique, but NMR has the disadvantage that it is sensitive to the electric field and requires a Radio-Frequency field which is screened inside the material [18].

The reason why one is interested in the magnetic field variations around a vortex rather than in the position of the vortices is that this can yield important information on the microscopic physics underlying superconductivity. For instance the magnetic field structure can be parameterized by the parameters  $\lambda$  and  $\xi$  linked to the phenomenological Ginzburg Landau theory (Sections 1.1.1 and 1.1.2). In turns, the value of those parameters and their dependence on field and temperature depend on the microscopic theory. More generally the detailed shape of the magnetic field around a vortex, or the way this shape depends on the proximity of other vortices depends on the underlying microscopic physics. See for instance [18] for a discussion of the vortex core structure. Another parameter of interest that we will mention is the vortex core size defined as the distance between the center of the vortex and the points at which the screening supercurrent density is maximal, which corresponds to the distance where the rate of variation of the magnetic field (the current density) is maximal [18].

The standard predictions are given by the BCS s-wave theory which is characterized

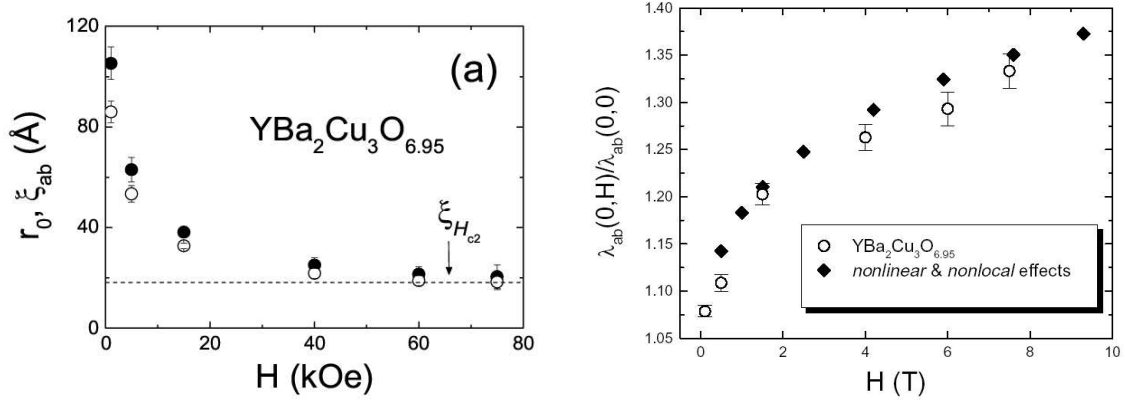


Figure 2.1: Experimental results extracted from Sonier’s 1999 paper [8]. They present non-trivial dependence of  $\lambda_{\text{eff}}$  and  $\xi_{\text{eff}}$ , as obtained from  $\mu\text{SR}$  experiments, on the magnetic field. Left figure: black circles represents the core radius  $r_{\text{eff}}$  and white circles the coherence length  $\xi_{\text{eff}}$ . Right figure: the black diamonds are from the theory by Amin *et al.* [23].

by an energy gap  $\Delta$  corresponding to the energy gained by electrons forming a *Cooper pair*, elementary superconducting carriers. Since the pair has a mass and a charge double of those of an electron, this theory enters the GL theory notably by setting  $q = -2e$  and  $m = 2m_e$ . It also predicts the dependence of the parameters  $\alpha$  and  $\beta$  on the field and temperature [5]. The theory is labeled “s-wave” because the gap  $\Delta$  around the Fermi surface is independent of the electron’s wave-vectors and therefore rotationally symmetric in  $k$ -space. Additionally the BCS theory can be modified so as to account for band structures of more complex symmetry, allowing for a gap which depends on the wave vector. The next simplest, most popular candidate for explaining the physics of the cuprate high temperature superconductors is the d-wave theory. Any symmetry more complex than the s-wave one may contain *nodes*: wave-vectors for which the gap is zero. Nodes are the cause of a much different physics as they allow for continuous quasi-particle excitation spectra and their signature can be detected in various experiments. For instance they induce a linear behavior of  $1/\lambda^2$  as function of low temperatures [17] [22], instead of a constant one as predicted by s-wave BCS [5]. More precise calculations also show that the nodes can lead to non-trivial dependences of  $\lambda$  on the magnetic field at low temperatures [23].

Sonier [8] used  $\mu$ SR to measure  $\lambda$  and observed a dependence of  $\lambda$  on the field  $B$  in YBCO similar to the prediction of Amin *et al.* [23] (Figure 2.1), right). Also Sonier [8] observed a large increase of  $\xi$  (figure (2.1, left) as well as of the vortex core radius in YBCO as the external magnetic field approaches  $H_{c1}$  from above. A similar increase has been found using the same technique in several other materials, reviewed in Ref. [18] (See Ref. [24] for a comparison to theory). This trend has also been observed with scanning tunneling microscope (STM) [25], but most evidences comes from  $\mu$ SR [18].

Because of the importance of the  $\mu$ SR technique for the above observations, it is important to understand whether the method used to extract  $\xi$  and  $\lambda$  from the  $\mu$ SR lineshape are reliable. In those experiments the two parameters, whose extracted values will be called  $\lambda_{\text{eff}}$  and  $\xi_{\text{eff}}$ , have been measured by fitting of the  $\mu$ SR lineshape with models parameterized by those two parameters.

However, the way by which one obtains those parameters starting from the  $\mu$ SR lineshape relies on nontrivial assumptions. Indeed many phenomena not directly related to  $\lambda$  or  $\xi$  define the lineshape. The most important contribution comes from the geometry of the vortex lattice. The above conclusions in Ref. [8] (as well as in Ref. [17], [19] and in general all measurements to date of  $\xi$  and  $\lambda$  using  $\mu$ SR), were derived by assuming that the vortices form an hexagonal lattice and that the deviations due to thermal fluctuations and disorder can be handled entirely by the single Gaussian broadening parameter  $\sigma$  as explained in Section 1.1.6. The work referenced by experimental  $\mu$ SR papers to justify this procedure is that of Brandt [26]. He studied the dependence of the field distribution features on various properties of the geometry of the flux lattice, including the effect of a certain type of disorder; mainly small uncorrelated fluctuations of stiff flux lines. His conclusion was that the effect of this type of disorder results in a ‘‘convolution’’ of  $n(B)$  with a Gaussian whose width is dependent on  $B$ . Strictly speaking this is not a convolution but a transformation defined by

$$\bar{n}(B) \propto \int e^{-B'^2/2\sigma^2(B)} n(B - B') dB'$$

where  $\bar{n}(B)$  is the disordered distribution while  $n(B)$  is the distribution for a perfect lattice. The function  $\sigma(B)$  is unknown. We found no detailed theoretical justification for the experimental practice consisting in replacing the function  $\sigma(B)$  by a constant  $\sigma$ .

Furthermore there are other types of fluctuations that one should take into account. The above result by Brandt was obtained considering only fluctuations of the vortex lines with respect to each other but no fluctuations of the vortex lines along the field direction (which is what we meant by the adjective “stiff”). Such alternative fluctuations can be important in a highly anisotropic layered superconductor. In another paper [27] Brandt studied the effect of fluctuations between pancakes of a layered superconductors, in different layers. He noticed that the effect can narrow the magnetic field distribution, in the sense of a reduction of the second moment  $\langle (B - \langle B \rangle)^2 \rangle$ , compared to the intrinsic width of the distribution derived from a perfect lattice. This is in contrast to his previous analysis concerning stiff lines where the disorder typically broadens the distribution, hence increasing its second moment.

In addition, one has to distinguish two types of fluctuations of the field. There are dynamical fluctuations on a timescale smaller than the muon’s lifetime ( $2.2 \mu\text{s}$ ) which are averaged prior to the extraction of the field distribution. The static spatial fluctuations, which can be caused by the pinning of the flux lattice by disorder in the underlying chemical structure of the material, as well as eventual fluctuations on a timescale longer than the muon lifetime, contribute in a very different way to the *effective* field distribution (defined as the Fourier transform of the  $\mu\text{SR}$  lineshape). As showed by Brandt, relative fluctuations between pancakes in the same layer lead to a broadening of the field distribution and fluctuations relative to pancakes in different layers can lead to a narrowing of the distribution. Also, as will be shown in Section 3.3.3, thermal fluctuations tend to narrow the field distribution.

The above analysis could be refined by studying the effect on the field distribution of static fluctuations caused by realistic disorders and with non-trivial correlations. An analytical calculation by Kohandel and Gingras [28] showed with a simple model that a disordered system in the experimentally observed Bragg glass phase (see below) can have an effect of same magnitude as a significant change in  $\lambda$ . This analysis concerns only the variance (second moment) of the magnetic field distribution which is absorbed by the fitting parameter  $\sigma$  in experiments, but the magnitude of the effect suggests that the question should be studied carefully, as other moments are also susceptible to vary.

It is important here to emphasize that  $\mu\text{SR}$  experiments have also been used to di-

rectly probe the geometry and fluctuations of the flux lattice rather than the properties of individual vortices as above, which proves that such effects exist [21][29][30].

For instance melting of the flux lattice, which corresponds to a destruction of the long range hexagonal order caused by thermal fluctuations, claims to have been observed in Ref. [21] using the skewness parameter

$$\alpha \doteq \frac{\langle (B - \langle B \rangle)^3 \rangle^{1/3}}{\langle (B - \langle B \rangle)^2 \rangle^{1/2}} \quad (2.1)$$

on the field distribution  $n(B)$  extracted from the  $\mu$ SR lineshape. (The average in this expression is over the measured distribution  $n(B)$ ). This parameter  $\alpha$  quantifies the asymmetry of the distribution. It is zero for a symmetric distribution and positive for the perfect lattice distribution (see Figure 1.4). In experiments it becomes negative at high temperatures. This is interpreted as a signature of the flux line lattice melting [21]. Variations in  $\alpha$  may imply deviations of the third moment, which cannot be accounted for by the parameter  $\sigma$ .

Such observations are not limited to thermal effects. Divakar *et al.* [29], using a  $\mu$ SR experiment on LSCO, deduced the existence of a transition between a quasi-ordered lattice of vortices (Bragg-glass) and a strongly disordered amorphous vortex glass [3] by observing an increase in the second moment of the field distribution.

Therefore, in order to validate the results of  $\mu$ SR experiments, both concerning the fluctuations of the vortex lattice and the field and temperature dependence of microscopic parameters, it is crucial to understand the extrinsic effects of thermal and spatial fluctuations of the vortex lattice on the magnetic field distribution.

In a high temperature superconductor, thermal agitation can melt the flux line lattice [3] [32]. Figure 1.1 shows a typical phase diagram. A transition indicative of the melting has indeed been observed in experiments (YBCO: [17][20][21][33], BSCCO: [34][35]) and in several simulations [36][37][38] as well as analytical calculations based on the Lindemann criterion [32][39][40], studies of the 2D boson model [41], a two-dimensional quantum-mechanical system equivalent to the continuous line model, and other models [42][43].

There has been a great amount of work dedicated to understanding the nature of the observed transition. For the three-dimensional system of flux lines, experiments and simulations are generally in favour of the existence of a first-order melting transition [38][44].

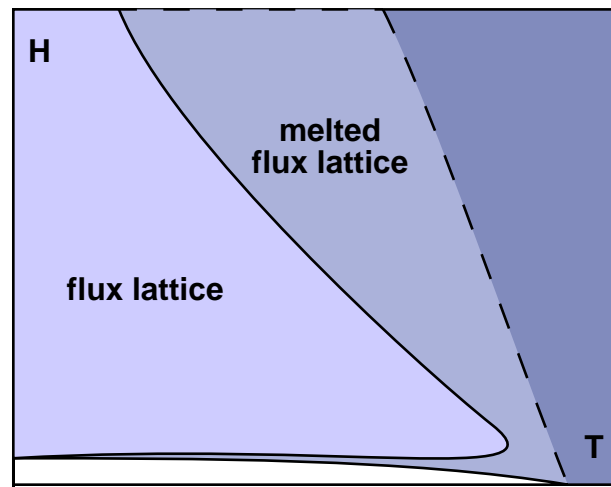


Figure 2.2: Cartoon phase diagram of a layered superconductor in the absence of disorder and in the regime where the description in terms of interacting classical flux lines is appropriate. The dark area on the right corresponds to the normal, non-superconducting phase and the white area at the bottom corresponds to the superconducting Meissner phase. The flux lattice is believed to melt both at low and high field under thermal agitation. At high fields (for  $a_0 < \gamma d$  [31]) the layers are effectively decoupled and the system melts into a “pancake liquid” while at lower field the system is melted into a system of entangled lines. At low fields ( $a_0 > \lambda$ ) the average distance between vortices enters the regime where the interaction energy 1.22 falls off exponentially, weakening the lattice and giving rise to the reentrant melting temperature.

Nevertheless there are still debates concerning the nature of the phases. For instance Yeo, Kienappel and Moore have argued on the basis of simulations that there is no solid-liquid transition but rather a first order liquid-liquid transition [38][45]. The main difference in their analysis comes from their use of spherical rather than toroidal boundary conditions. The problems in understanding this transition in general stems from the fact that there is no fully analytical model of melting, which forces one to rely heavily on simulations which are plagued by strong finite-size effects, and do not offer good qualitative understandings like analytical models.

Additionally a high-temperature superconductor always contains some random disorder. Apart from the difficulty of obtaining single crystals free of lattice defects, optimal superconductivity relies on non-stoichiometric doping which in itself may introduce disorder inside the material (Section 3.2). Disorder can make the detailed theoretical phase diagram of high-temperature superconductors very complex [39]. It is believed that disorder of the underlying lattice, or even weak disorder caused by doping, always destroy the long-range order of the flux line lattice [46]. Figure 2.3) shows a possible phase diagram with features that can be addressed by a flux line model. The idea is that the disorder is weak enough to not significantly perturbate the solid-liquid transition, except in the low field region where the lattice is supposed to become very fragile and melt at low temperature, as well as in high field (observed for  $B > 10$  (T) for YBCO [29][47] were the vortices become very close together such that small perturbations of their position have stronger effect on the hexagonal order. At high field and also perhaps at low fields, the system should get pinned into the disordered phase, leading to a “vortex glass” [3]. Experiments show that the first-order melting line ends at a tricritical point as the solid phase becomes disordered at high field [34][47].

At intermediate fields (which corresponds to the field probed in Sonier’s  $\mu$ SR experiments on YBCO [8]), the system is expected [48] to be in the most ordered phase allowed by a weak disorder which would be a “Bragg glass” as defined by Giamarchi and Le Doussal [46]. This phase is characterized by logarithmically diverging root-mean-square relative displacements between vortices. We will describe such a phase in more detail in Section 3.2. At higher field the pinning energy should overcome the interactions between vortices allowing defects to enter the vortex lattice [49]. This theory is consistent with an irre-

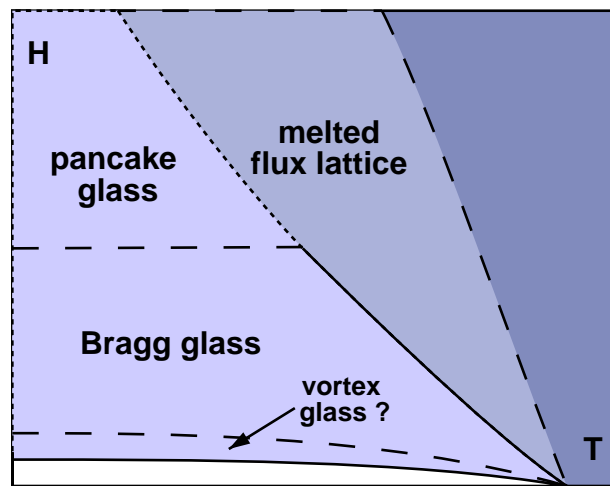


Figure 2.3: Tentative (Cartoon) Phase Diagram of a layered superconductor in the presence of disorder and in the regime where the description in terms of interacting classical flux lines is appropriate. The dark area on the right corresponds to the normal, non-superconducting, phase and the white area to the superconducting Meissner phase. The mixed phase is divided into a region in which the flux lattice is melted and one in which the flux lattice is partly ordered and partly pinned by the disorder. The relative strength of the pinning depends on the magnetic field. The disorder should be the weakest in intermediate magnetic fields, giving rise to a “Bragg glass” phase with logarithmically diverging root-mean-square relative displacement between vortices [46]. At high field ( $B > 10$  (T) for YBCO [29][47]) the pancakes are decoupled and the disorder destroys the lattice more easily.

versibility line in magnetisation experiments as in Kadowaki *et al.* [35] for BSCCO and Bouquet *et al.* [47] and Divakar *et al.* [29] for YBCO, in which it happens around 10 Tesla, somewhat lower than the decoupling field of 30 Tesla. It has also been studied numerically by Otterlo *et al.* [50].

## 2.1 Goals

The observations by Sonier [8] of variations in  $\xi$  and  $\lambda$  using  $\mu$ SR in YBCO under the assumption of an hexagonal lattice subject to small fluctuations were done at fields between 0.1 to 8 Tesla. This range spans most of the Bragg glass phase and may come close to two highly disordered regions, both at high and low field, where the assumption of small fluctuations around an hexagonal lattice are wrong.  $\mu$ SR experiments have also been used to measure temperature dependence of  $\lambda$  [8] in regimes where thermal fluctuations can become important as the melting transition is approached.

From another perspective, observation of broad features of the field distribution obtained from  $\mu$ SR experiments was used to identify the Bragg glass-vortex glass transition at around 10 Tesla in YBCO as well as the melting transition. We want to understand how efficient the broadening parameter  $\sigma$  is at quantitatively describing thermal and static fluctuations in the regimes of interest. We question to what extent the field and temperature dependence of the parameters  $\xi_{\text{eff}}$  and  $\lambda_{\text{eff}}$  observed in  $\mu$ SR experiments are real or partially due to a quantitatively inaccurate account of vortex lattice fluctuations.

Our aim in this work is to design a simulation able to reproduce the above phase diagrams, for the clean case as well as for the disordered case. Also the simulation should be able to compute the magnetic field inside the material, taking the vortex core into account (which has not been done before).

We choose the model introduced by Ryu [44], because it has been used before to describe flux lattice melting [44] as well as the glass transition [50], and also allowed to compute the field distribution at the melting transition [51]. We will first study carefully the properties of the chosen model analytically and numerically, determine the type of melting transitions it describes and compare thermodynamical data to experiments in YBCO. Other material like BSCCO are considered. Also we will obtain field distributions for the system without

disorder and apply the experimental fitting with broadening parameter  $\sigma$ . We will then compare the obtained fits  $\lambda_{\text{eff}}$  and  $\xi_{\text{eff}}$  to the values used in the simulation in order to test the experimental fitting method. We will also compute the second moment and skewness  $\alpha$  of the field distribution and compare them to experiments [21] [29].

Finally we will attempt to obtain the low temperature phase diagram in the disordered system, with field distribution as well, and apply the  $\mu\text{SR}$  fitting method to our results in order to test the conclusion drawn in experiments [8] [19].



# Chapter 3

## Model

We use the model introduced in Seungoh Ryu's Ph.D. thesis [37] and used by Ryu *et al.* in [44]. The vortex pancakes are treated like interacting classical point particles. In principle there should be two kind of interactions; an electromagnetic interaction between any two pancakes as well as a coupling between two pancakes in adjacent layers due to tunneling effects [37]. Because it is numerically too expensive to perform a sum over all pancake pairs in the volume, the electromagnetic interaction between pancakes in different layers is neglected. But it is not neglected by being set to zero. Instead the effective interaction used between two pancakes in the same layers is such that it assumes an infinite pile of pancakes below and above each other. From Clem's solution [10] we know that the interaction between pancakes in the same layer is essentially logarithmic. The cumulated interactions with the other pancakes in a perfectly aligned pile screen this interaction over a lengthscale  $\lambda$ . Therefore the effect of the out-of-plane electromagnetic interaction become important when the spacing between vortices is bigger than  $\lambda$ . But this is also the regime in which the vortex lines are expected to maintain their integrity (because the interlayer fluctuations are much smaller than the average spacing between vortices), hence justifying the approximation. (See also the discussion in Ryu's thesis [37], page 86).

The interaction energy between each two pancakes in the same layer and separated by a distance  $r$  is given by

$$U_1(r) = d\varepsilon_0 K_0(r/\lambda) \tag{3.1}$$

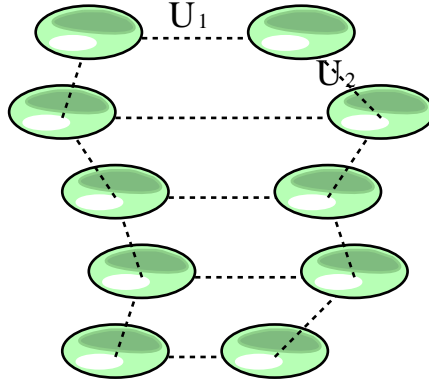


Figure 3.1: The dotted lines link interacting pairs of pancakes. The horizontal lines represent the interaction term 3.1 and the vertical lines represent the interaction terms 3.3.

where

$$\varepsilon_0 = \frac{\Phi_0^2}{2\pi\mu_0\lambda^2} \quad (3.2)$$

and  $d$  is the distance between two layers. This is the same expression as the interaction energy between two continuous flux lines on a distance  $d$ : Equation 1.22.

In addition to the electromagnetic interaction, the Lawrence-Doniach free energy (Section 1.1.5) provides a term coupling the phase of the superconductivity order parameter between two layers [52]. This gives rise to a coupling between pancakes in adjacent layers which is mainly harmonic for distances shorter than the *Josephson healing length*  $2r_g \simeq 2\gamma d$  [37] where  $\gamma$  is the anisotropy (Section 1.1.5). When the distance is larger, a Josephson vortex running parallel to the layers and linking the two pancakes can exist, with an energy proportional to its length [37]. This phenomenon is modeled by an interaction energy

$$U_2(r) = d\varepsilon_0 \frac{1 + \ln(\lambda/d)}{\pi} \times \begin{cases} \frac{r^2}{4r_g^2} - 1 & \text{if } r < r_g, \\ \frac{r}{2r_g} - 1 & \text{if } r > r_g. \end{cases} \quad (3.3)$$

where  $r$  is the relative distance between the two pancakes as projected on the layers. This interaction exists only for chosen pairs of vortices across two adjacent layers, effectively defining a pile of pancakes as a collection of pancakes in distinct layers each interacting through this term. Figure 3.1 represents which pairs of pancakes belonging to two different

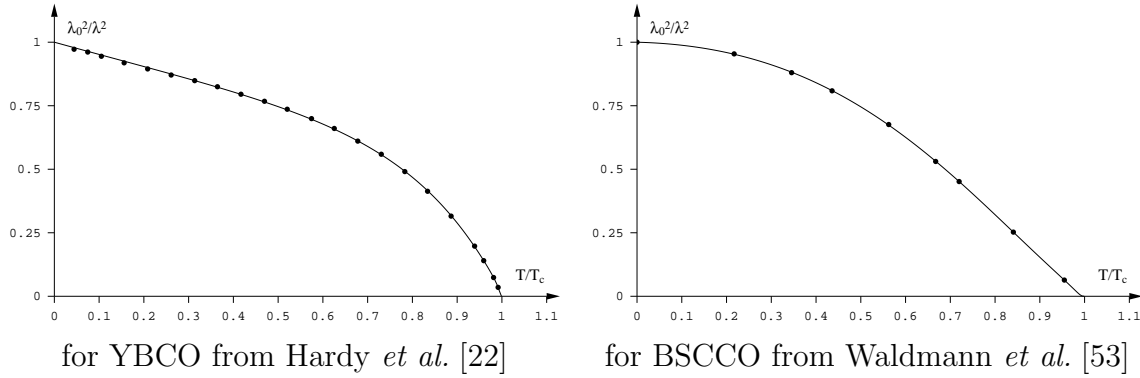


Figure 3.2: Experimental values for the dependence of the order parameter  $\lambda$  on the temperature at zero external field. Those graphs represent  $\lambda^2(0)/\lambda^2(T)$ . The dots are the experimental points and the line is a polynomial fit in log-log space and is the function actually used in our model.

piles are interaction via Equation 3.1 or 3.3.

### 3.1 The penetration depth

The penetration depth depends highly on the temperature since it diverges at the superconducting transition. The exact behaviour of the penetration depth in high-temperature superconductors is an intense subject of theoretical and experimental research because it is one of those features which indicates the existence of nodes in the energy Gap, and therefore the non s-wave nature of high-temperature superconductors. For our simulation we chose to use experimental data for our function  $\lambda(T)/\lambda(0)$ . Figure 3.2 shows the functions used for YBCO<sup>1</sup> and BSCCO.

### 3.2 Disorder

We focus on the disorder caused by defects correlated over a range smaller than the coherence length  $\xi_0$ . This is expected of oxygen vacancies [54][55]. For instance YBa<sub>2</sub>Cu<sub>3</sub>O<sub>7-y</sub>

---

<sup>1</sup>See “<http://www.physics.ubc.ca/supercon/datasets.html>” for measurements of  $\lambda$  for various doping on YBCO.

reaches its maximum superconducting temperature for a non-integer value  $y \simeq 0.05$ . This results in a random distribution of sites where an oxygen is missing from the unit cell of the stoichiometric material  $\text{YBa}_2\text{Cu}_3\text{O}_7$ . This creates a random pattern which can locally modify the superconducting properties of the material, effectively acting as disorder. Because this doping is needed in order to achieve an optimal superconducting temperature, such disorder will always be present even in the best crystal.

For instance, in the proximity of a site with higher or lower doping, superconductivity may be slightly less favoured in terms of free energy. Therefore energy can be gained by placing a non-superconducting vortex cores in such a region.

We assume that there is a large number of randomly distributed pinning centers each interacting with a vortex pancake according to a potential  $f(r)$ , where  $r$  is the in-plane vector separating the point defect and the vortex center. We assume no direct interaction between a defects and vortices belonging to different layers, for the pancake cores do not extend between layers ( $\xi_z < d$ ).

Prior to discussing the form of this function  $f$  (in Section 3.2.1), we want to show how the picture in terms of point defects translates to the framework used for instance by Giamarchi and Le Doussal [46] as well as Blatter *et al.* [56] and Otterlo *et al.* [50]. We model this disorder as a Gaussian random field. This assumes that there are always many pinning centers interacting with each vortex so that we can neglect the discrete nature of the disorder.

The approximation we make is to retain only the two point correlation function of the original model, effectively yielding a random field with a Gaussian probability distribution, as in Ref. [50].

The energy landscape experienced by a vortex at position  $(r, z)$  for  $N$  defects located at random positions  $(r_i, z_i)$  in a volume  $V = S \cdot L$  (with periodic boundary conditions), where  $L$  is a dimension perpendicular to the layers (in the  $z$  direction) is

$$V(r, z) = \sum_{i=1}^N f(r_i - r) \delta_{z_i, z}$$

where  $\delta$  is a Kroenecker delta function (it has no unit). We assume here that the  $z$  positions can take only  $L/d$  discrete values where  $d$  is the distance between layers. The two-point

correlation function is

$$\begin{aligned}
\langle V(0,0)V(r,z) \rangle &= \frac{d^N}{V^N} \int dr_1 \dots dr_N \sum_{z_1 \dots z_N} \sum_{ij} f(r_i) f(r_j - r) \delta_{z_i,0} \delta_{z_j,z} \\
&= \frac{d^N}{V^N} \int dr_1 \dots dr_N \left( \frac{L^{N-1}}{d^{N-1}} \delta_{z,0} \sum_i f(r_i) f(r_i - r) + \frac{L^{N-2}}{d^{N-2}} \sum_{i \neq j} f(r_i) f(r_j - r) \right) \\
&= \frac{d}{V^N} \left( V^{N-1} \delta_{z,0} N \int dr' f(r') f(r' - r) + dV^{N-2} (N^2 - N) \left[ \int dr' f(r') \right]^2 \right) \\
&= dn \delta_{z,0} (f \star f)(r) + (1 - N^{-1}) \langle V(r,z) \rangle^2
\end{aligned}$$

where  $n = N/V$  stands for the density of defects and  $\star$  the convolution operator

$$(f \star g)(x) \doteq \int dr f(r) g(x - r)$$

where the integration is taken over the full two-dimensional plane. We also introduced the average

$$\begin{aligned}
\langle V(r,z) \rangle &= \frac{d^N}{V^N} \int dr_1 \dots dr_N \sum_{z_1 \dots z_N} \sum_i f(r_i - r) \delta_{z_i,z} \\
&= dn \int dr' f(r').
\end{aligned}$$

Therefore the correlation for zero average is, in the limit of large  $N$ ,

$$\begin{aligned}
C(r,z) &= \langle V(0,0)V(r,z) \rangle - \langle V(0,0) \rangle \langle V(r,z) \rangle \\
&= dn \delta_{z,0} (f \star f)(r)
\end{aligned} \tag{3.4}$$

Another way to build the same random field is by convolution of a field with an uncorrelated Gaussian noise. Let  $\phi(r,z)$  be a Gaussian random field defined by  $\langle \phi(r,z) \rangle = 0$  and  $\langle \phi(r,z) \phi(r',z') \rangle = \delta(r - r') \delta_{z,z'}$ . We want to find a function  $g(r)$  such that

$$V(r,z) = \int dr' \phi(r',z) g(r' - r)$$

with the same correlation as above (the average  $\langle V \rangle$  is physically irrelevant)

$$\langle V(0,0)V(r,z) \rangle = dn \delta_{z,0}(f \star f)(r).$$

This yields

$$\delta_{z,0}(g \star g)(r) = dn \delta_{z,0}(f \star f)(r)$$

therefore we have

$$V(r,z) = \sqrt{dn} \int dr' \phi(r',z) f(r'-r). \quad (3.5)$$

### 3.2.1 Disorder strength

We follow the arguments of Blatter *et al.* [56] and assume that the disorder manifests itself through local fluctuations of the superconducting critical temperature, related to the parameter  $\alpha$  of the Ginzburg-Landau free energy 1.7. We model the interaction potential as

$$f(r) = f(0) \frac{2\xi^2}{r^2 + 2\xi^2} \quad (3.6)$$

so that

$$C(0,0) = 2\pi dn \xi^2 f(0)^2. \quad (3.7)$$

Blatter *et al.* introduce the dimensionless parameter  $\delta_\alpha$  such that

$$nf(0)^2 = \frac{\delta_\alpha}{4\pi\xi} \left( \frac{\Phi_0^2}{2\pi\mu_0\lambda^2} \right)^2.$$

Finally the expression for the disorder potential expressed as in Equation 3.5 in terms of a random field  $\phi$  is

$$V(r,z) = \sqrt{\frac{d\delta_\alpha}{4\pi\xi}} \left( \frac{\Phi_0^2}{2\pi\mu_0\lambda^2} \right) \int dr' \phi(r',z) \frac{2\xi^2}{(r'-r)^2 + 2\xi^2}$$

Blatter *et al.* give an estimate for  $\delta_\alpha$  for optimal doping and perfect crystals of YBCO or BSCCO (Equation 3.79 of their paper [56] )

$$\delta_\alpha \simeq \frac{\gamma}{1000} (1-t)^{-1/2}$$

where  $\gamma$  is the anisotropy ratio and  $t$  the reduced temperature relative to the superconducting transition temperature at zero field.

Their derivation goes roughly as follow. The microscopic derivation of the GL equations by Gor'kov [57] allows to express the superconducting transition temperature  $T_c$  as a function of the parameter  $\alpha$  entering the GL equations<sup>2</sup>. Therefore it relates the spatial RMS (Root Mean Square) fluctuations of the GL free energy induced by the fluctuations of  $\alpha$  to the spatial RMS fluctuations of  $T_c$ . Then they note that the spatial fluctuations of  $T_c$  must be a function of the spatial density of oxygen vacancies, but convoluted with a function of width  $\xi$ ; the lengthscale over which the superconducting order parameter can vary. The dependance of the overall transition temperature on the oxygen vacancies is known experimentally, as well as its derivatives with respect to the oxygen vacancy density. The total derivatives can be expanded in terms of partial spatial derivatives, allowing one to link the proportion of oxygen vacancies to the RMS fluctuations of  $T_c$ , and then back to fluctuations in free energy.

### 3.2.2 Disorder lengthscales

Giamarchi and Le Doussal [46] analytically studied the properties of a weakly pinned flux lattice. The phase they analyze has logarithmically decaying correlations and contains no lattice defect. Even though the system has no true long range order, a diffraction pattern would still display peaks which would experimentally appear similar to Bragg peaks. Such a “Bragg glass” is consistent with the experiments at intermediate fields [48]. The phase is characterized by two lengthscales related to the behaviour of the mean-square relative displacement

$$\delta u_{\perp}^2(r) = \left\langle (u(r) - u(0))^2 \right\rangle \quad (3.8)$$

as a function of distance. In the above expression,  $u(r)$  is the in-plane displacement of a vortex from its equilibrium position  $r$ . At small length scales an early analysis by Larkin [58] is valid and  $\delta u_{\perp}(r)$  grows linearly with the distance. But as  $\delta u_{\perp}(r)$  reaches the lengthscale at which the disorder forces are correlated, which is of the order of the

---

<sup>2</sup>This derivation is based on the s-wave BCS theory which may not apply for a high-temperature superconductor. However we are just interested in having an estimation of the order of magnitude for the disorder strength.

coherence length  $\xi$ , then the argument is not valid and the system enters a “random manifold” regime where  $\delta u_{\perp}(r)$  grows more slowly, like  $r^{1/3}$ . On much larger lengthscales this behaviour changes to an even slower logarithmic decay at a lengthscale  $R_a$ . Roughly  $R_a$  corresponds to the length at which  $\delta u_{\perp}(r)$  would be approximatively  $a_0$  if the Larkin regime was valid at this lengthscale. Assuming a random pinning potential, the scale  $R_a$  can be computed as [46]

$$R_a \simeq \frac{1}{\pi^4} \frac{C_{66}^{3/2} C_{44}^{1/2} a_0^4}{\rho_0^2 U_p^2 d \xi^2}$$

where the elastic constant  $C_{44}$  is the tilt modulus and  $C_{66}$  the shear modulus (both per unit length),  $d$  is the inter-plane distance,  $U_p d$  is the RMS fluctuations of the pinning landscape of in-plane correlation length  $\xi$ .  $\rho_0$  is the 2D density of vortex lines for spacing  $a_0$ . First we need to express  $U_p$  in terms of  $\delta_{\alpha}$  for which we have an estimate (from Equations 3.4 and 3.7):

$$U_p^2 = \frac{C(0,0)}{d^2} = \frac{\xi \delta_{\alpha}}{4d} \varepsilon_0^2$$

With proper values for the elastic constant and knowing

$$a_0^2 = \frac{2}{\sqrt{3}} \frac{\Phi_0}{B}$$

the expression for  $R_a$  reduces to

$$\frac{R_a}{a_0} = \left[ \frac{C}{B} \right]^{3/2} \frac{4d}{\xi \delta_{\alpha}}$$

where  $C$  is a (physically meaningless) constant with unit of field:

$$C^{3/2} \simeq \frac{\ln(\gamma d / \xi)^{1/2}}{2^{3/2} 3^{3/4} \pi^4} \frac{\Phi_0^{3/2}}{\gamma d \xi^2} \simeq 10^{-3} \frac{\Phi_0^{3/2}}{\gamma d \xi^2}$$

where  $\gamma$  is the anisotropy ratio.

Using the numerical values for YBCO

$$\gamma \simeq 8 \text{ [59]}, \quad d \simeq 12 \text{ \AA} \text{ [60]}, \quad \xi \simeq 20 \text{ \AA} \text{ [8]}$$

One gets

$$C^{YBCO} \simeq 3T$$

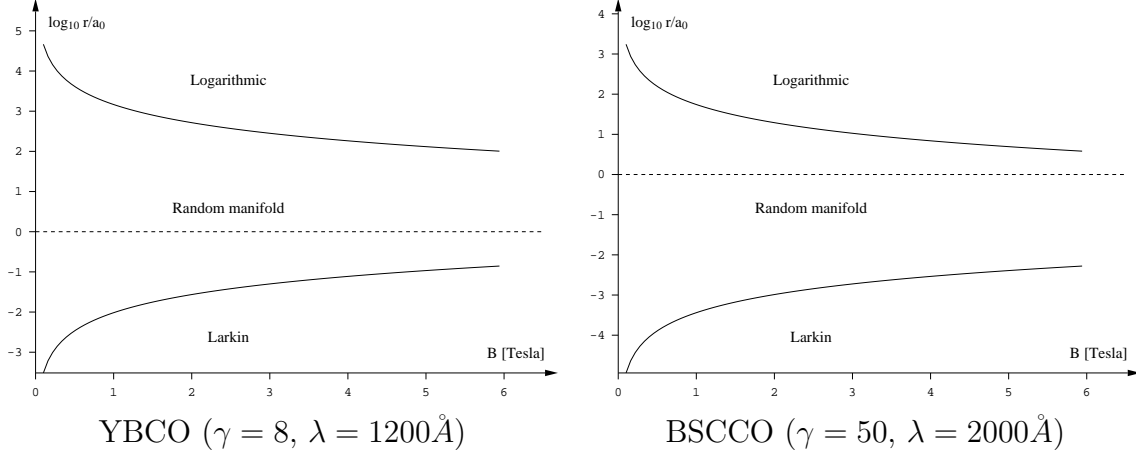


Figure 3.3: Estimation of the crossover length  $B_c$  and  $B_a$  for the Bragg glass phase for typical parameters in YBCO and BSCCO, according to the theory of Giamarchi and Le Doussal [46]. The lines separate lengthscales into three domains. The shortest domain is the one in which the Larkin regime is valid with linear growth of the mean-square relative displacement  $\delta u_{\perp}(r)$ . In the intermediate domain  $\delta u_{\perp}(r)$  grows also as a polynomial but much more slowly. Then at longer lengthscales  $\delta u_{\perp}(r)$  grows logarithmically.

We also introduce  $R_c(T, B)$ , the length scale below which the Larkin regime prevails.  $R_c(0, B)$  is the Larkin-Ovchinnikov length. At  $T = 0$  the mean square relative displacement between vortices separated by a distance  $R_c$ ;  $\delta u_{\perp}(R_c)$ , is of order

$$\delta u_{\perp}(R_c) \simeq \max(l_T^2, \xi^2)$$

where  $l_T$  is the range of the thermal fluctuations:

$$l_T^2 = 2\langle u^2 \rangle_T.$$

Le Doussal and Giamarchi give

$$\frac{R_c}{a_0} = C_s \frac{R_a}{a_0} \left( \frac{l_T^2 + \xi^2}{a_0^2} \right)^3$$

where  $C_s$  is some numerical constant whose value is  $C_s \simeq 1400$  [46].

Figure 3.3 shows the values of those two lengthscales relative to the lattice spacing  $a_0$  for different fields for YBCO. For all field intensities,  $R_c < a_0$ , which means that the Larkin regime does not exist. A typical simulation can handle about a hundred vortices and therefore cannot access lengthscale greater than  $10a_0$ . Hence a simulation will mostly probe the random manifold regime. Because such a state has no lattice defects and because periodicity is imposed by the finite simulation box, we expect to observe essentially a crystal. In principle the root-mean-square relative displacement function  $\delta u_{\perp}(r)$  should display the power-law behaviour of the random manifold regime.

### 3.3 Magnetic field

In this section we explain how the magnetic field can be calculated for an arbitrary configuration of the pancakes in view of building the field distribution. The expression that we obtain is an original result. It allows to efficiently compute the field taking a model of the vortex cores into account. (Clem [10] provides a model of the magnetic field which neglects the core). We also show how the ensemble average can be approximated at low temperature.

We want to compute the magnetic field at any point inside the simulation box assuming periodic boundary conditions in every directions. If we know the Fourier components  $\mathbf{b}(k)$  of the field around a single vortex and if the individual fields add linearly, then the total field at point  $x$  is

$$\mathbf{B}(x) \propto \sum_K \sum_{i=1}^N e^{-iK(x-r_i)} \mathbf{b}(K)$$

where the  $K$ 's are reciprocal vectors of the simulation cell and  $r_i$  is the position of the pancake  $i$  inside the simulation cell expressed in the real-space basis reciprocal to  $K$ .  $N$  is the number of pancakes in the simulation. This accounts for the contribution of all periodic images of the pancakes.

#### 3.3.1 General expression

We want to find some expression for the Fourier transform  $\mathbf{b}(k)$  of the field of a single vortex that accounts for the finite core size of the pancakes and give the simple limit for a

straight lines with a Gaussian cutoff: expression 1.19.

From the phase-dependent part of the GL equations, the field generated from a point source is given by [52]

$$\mathbf{A}(\mathbf{k}) + \lambda^2 \mathbf{k}^2 \mathbf{A}(\mathbf{k}) = id\Phi_0 \frac{\mathbf{k} \times \hat{\mathbf{z}}}{\mathbf{k}_\perp^2}$$

where  $\hat{\mathbf{z}}$  is the unit vector perpendicular to the layers and we used the notation  $\mathbf{k} = \mathbf{k}_\perp + k_z \hat{\mathbf{z}}$ . In order to model the finite core size we introduce a Gaussian cutoff in the source term, but only in the directions perpendicular to  $z$  since the core size along  $z$  is much smaller [10] (this will be motivated below).

$$\mathbf{A}(\mathbf{k}) + \lambda^2 \mathbf{k}^2 \mathbf{A}(\mathbf{k}) = id\Phi_0 \frac{\mathbf{k} \times \hat{\mathbf{z}}}{\mathbf{k}_\perp^2} e^{-\frac{1}{2}\xi^2 \mathbf{k}_\perp^2}.$$

Therefore

$$\mathbf{A}(\mathbf{k}) = id\Phi_0 \frac{e^{-\frac{1}{2}\xi^2 \mathbf{k}_\perp^2}}{1 + \lambda^2 \mathbf{k}^2} \frac{\mathbf{k} \times \hat{\mathbf{z}}}{\mathbf{k}_\perp^2}$$

the curl of which yields

$$\mathbf{b}(\mathbf{k}) = d\Phi_0 \frac{\mathbf{k}_\perp^2 \hat{\mathbf{z}} - k_z \mathbf{k}_\perp}{\mathbf{k}_\perp^2 (1 + \lambda^2 \mathbf{k}^2)} e^{-\frac{1}{2}\xi^2 \mathbf{k}_\perp^2}.$$

When computing the  $\mu$ SR lineshape we will neglect the components of the total field perpendicular to the applied field. In the case of the perfect lattice, we expect those components to be small because, by symmetry, they are given to vary only over a lengthscale  $d$  which is much smaller than the typical lengthscale  $\lambda$  over which a variation of the field can be significant. Furthermore this allows us to directly match the approximation made in the  $\mu$ SR discussion in Section 1.1.6 where one assumes that the field is everywhere parallel to the applied field. Therefore we focus on the  $z$  component of  $\mathbf{b}$ :

$$b_z(\mathbf{k}) = \frac{d\Phi_0}{1 + \lambda^2(k_z^2 + \mathbf{k}_\perp^2)} e^{-\frac{1}{2}\xi^2 \mathbf{k}_\perp^2}.$$

Let us convert the  $z$  component back to real space:

$$b_z(\mathbf{k}_\perp, z) = d\Phi_0 e^{-\frac{1}{2}\xi^2 \mathbf{k}_\perp^2} \int_{-\infty}^{\infty} \frac{dk_z}{2\pi} \frac{e^{-ik_z z}}{1 + \lambda^2(k_z^2 + \mathbf{k}_\perp^2)}.$$

We have to perform the integral

$$I = \int_{-\infty}^{\infty} dk \frac{e^{-ikz}}{A^2 + k^2}$$

Contour integration around the pole at  $z = iA$  yields

$$I = \frac{\pi}{A} e^{-A|z|}.$$

Therefore

$$b_z(\mathbf{k}_\perp, z) = \frac{d\Phi_0}{2\lambda\sqrt{1+\lambda^2\mathbf{k}_\perp^2}} e^{-\frac{1}{\lambda}\sqrt{1+\lambda^2\mathbf{k}_\perp^2}|z| - \frac{1}{2}\xi^2\mathbf{k}_\perp^2}. \quad (3.9)$$

In order to have an intuition of the resulting field, let us compute the field (in real space)  $B_z(\mathbf{r} = 0, z)$  for a single, isolated pancake, neglecting the cutoff  $\xi$  (setting  $\xi = 0$ ). This is

$$\begin{aligned} B_z(\mathbf{r} = 0, z) &= \int \frac{d\mathbf{k}_\perp}{4\pi^2} b_z(\mathbf{k}_\perp, z) \\ &= \frac{d\Phi_0}{4\pi\lambda} \int_0^\infty dk k \frac{e^{-\frac{|z|}{\lambda}\sqrt{1+\lambda^2k^2}}}{\sqrt{1+\lambda^2k^2}} \\ &= \frac{d\Phi_0}{4\pi\lambda^2|z|} e^{-|z|/\lambda}. \end{aligned} \quad (3.10)$$

We see that the field decays exponentially fast in the direction perpendicular to the layers. We note that, as a consistency check, this term is strictly equal to equation (25a) in Clem's paper [10].

Let us also check that, despite the approximation  $\xi_z = 0$ , the field divergence at  $z = 0$  in the above expression is eliminated by  $\xi$ :

$$\begin{aligned} B_z(\mathbf{r} = 0, z = 0) &= \int \frac{d\mathbf{k}_\perp}{4\pi^2} \frac{d\Phi_0}{2\lambda\sqrt{1+\lambda^2\mathbf{k}_\perp^2}} e^{-\frac{1}{2}\xi^2\mathbf{k}_\perp^2} \\ &= \frac{d\Phi_0 e^{\xi^2/2\lambda^2}}{\sqrt{2\pi}4\xi\lambda^2} \left[ 1 - \operatorname{erf}(\xi/\sqrt{2}\lambda) \right] \end{aligned} \quad (3.11)$$

where erf is the so-called error function; the indefinite integral of a normal Gaussian, set to equal zero at  $-\infty$ .

Also, because the field typically varies over a lengthscale  $\lambda \gg \xi_z$ , we expect the negligence of  $\xi_z$  to be harmless. We actually go further in allowing ourselves to neglect the effect on the field distribution of the variations of the field between two layers. Indeed this would be very costly to integrate numerically. We judge that we can neglect this effect because Equation 3.10 shows us that the field varies in the  $z$  direction only over a lengthscale  $\lambda \gg d$ .

Instead we will use the field averaged over a distance  $d$ . Therefore we have to analytically integrate expression 3.9 over the range  $z \in [z_0 - d/2, z_0 + d/2]$ . Furthermore we have to sum over all images coming from the periodic boundary conditions along  $z$ . Both operations are needed in order to ensure the proper average magnetic field for any configuration of the pancakes. Furthermore this yields the exact magnetic field for straight lines, as will be shown in the next section. For convenience we use  $\Delta \doteq \sqrt{1 + \lambda^2 \mathbf{k}_\perp^2}$  and we perform these calculations on the following factor of  $b_z$ ;

$$v(\mathbf{k}_\perp, z) = \frac{d}{2\lambda\Delta} e^{-\Delta|z|/\lambda}$$

Let's first do the averaging:

$$\begin{aligned} \bar{v}(\mathbf{k}_\perp, z - z_0) &= \frac{1}{d} \int_{z - \frac{d}{2}}^{z + \frac{d}{2}} v(\mathbf{k}_\perp, \zeta - z_0) d\zeta \\ &= \begin{cases} \Delta^{-2} \left(1 - e^{-\frac{d\Delta}{2\lambda}}\right) & \text{if } z = z_0, \\ \Delta^{-2} e^{-\Delta|z - z_0|/\lambda} \sinh\left(\frac{d\Delta}{2\lambda}\right) & \text{if } z \neq z_0. \end{cases} \end{aligned}$$

The sum over images yields

$$\begin{aligned} \bar{v}^s(\mathbf{k}_\perp, z) &= \sum_{n=-\infty}^{\infty} \bar{v}(\mathbf{k}_\perp, z - nL) \\ &= \begin{cases} \frac{1 - e^{-\delta L} - e^{-\delta \frac{d}{2}} + e^{-\delta(L - \frac{d}{2})}}{\Delta^2(1 - e^{-\delta L})} & \text{if } z = 0, \\ \frac{e^{-\delta(L - \frac{d}{2} - |z|)} + e^{-\delta(|z| - \frac{d}{2})} - e^{-\delta(L + \frac{d}{2} - |z|)} - e^{-\delta(|z| + \frac{d}{2})}}{2\Delta^2(1 - e^{-\delta L})} & \text{if } z \neq 0. \end{cases} \end{aligned}$$

with  $\delta = \Delta/\lambda$  and  $L$  the thickness of the simulation cell (its dimension perpendicular to the layers). This has been put in a form appropriate for numerical evaluation (it avoids excessively small or big intermediate results.)

From there we can construct the summed/averaged version of  $b_z$ :

$$\bar{b}_z^s(\mathbf{k}_\perp, z) = \Phi_0 \bar{v}^s(\mathbf{k}_\perp, z) e^{-\frac{1}{2}\xi^2 \mathbf{k}_\perp^2}$$

where  $z/d$  has to be an integer (we compute only the field within a layer). We get the total field at point  $z = \mathbf{r} + z\hat{\mathbf{z}}$  through

$$B_z(\mathbf{r}, z) = B_0 \frac{1}{n} \sum_{\mathbf{K}_\perp} \sum_{i=1}^N e^{-i\mathbf{K}_\perp(\mathbf{r}-\mathbf{r}_i)} \bar{v}^s(\mathbf{K}_\perp, z_i - z) e^{-\frac{1}{2}\xi^2 \mathbf{K}_\perp^2} \quad (3.12)$$

where  $\mathbf{r}_i$  and  $z_i$  are respectively the in-plane and out of plane components of pancake  $i$ ,  $n$  the number of pancakes in one layer, and

$$B_0 = \frac{2}{\sqrt{3}} \frac{\Phi_0}{a_0^2}$$

is the average magnetic field. This sum can be evaluated numerically with a cutoff on  $K_\perp$  corresponding to the desired spatial resolution

Because we summed over images in the  $z$  direction, those formula are most appropriate for a simulation with periodic boundary conditions along  $z$ . However the main reason why we performed this summation is to exactly recover the field for a perfect lattice in the case where the pancakes are all well aligned (see next section). In fact, when we dynamically average the field we will make use of open boundary conditions<sup>3</sup>. This means that the field we are computing seems periodic but with a discontinuity at the boundary images. In this case we will compute the field only in the layer which is in the middle of the sample, in order to be as far as possible from the discontinuities.

We would like to have an idea of the importance on the field distribution of the finite number of layers in the simulation. We can compute the contribution of the total field generated by a single pancake in a layer at a distance  $z$  away by integrating the Fourier transform of  $b_z(\mathbf{k}_\perp)$  (Equation 3.9) over all position  $\mathbf{r}$ :

$$\Phi(z) = \int d\mathbf{r} \int \frac{d\mathbf{k}_\perp}{4\pi^2} e^{-i\mathbf{k}_\perp \mathbf{r}} b_z(\mathbf{k}_\perp, z) = b_z(0, z) = \frac{d\Phi_0}{2\lambda} e^{-|z|/\lambda}$$

---

<sup>3</sup>This allows to observe the flux lattice melting with a fewer number of layers as periodic boundary conditions would artificially rigidify the lattice.

This means that the field generated at even 100 layers away for YBCO ( $z \simeq \lambda$ ) is still just one third of the total field generated in a given layer. However the field generated from different layers is smoother and therefore depends less on the position of the pancakes in that layer. Formula 3.10 shows that the field's maximum decays as  $e^{-z/\lambda}/z$  which falls more rapidly. At a distance  $z \simeq \lambda$  this is 0.5% smaller than the maximum field in the layer at which the field is evaluated (Equation 3.11). This means that a displacement in the position a pancake a hundred layers away will have an effect approximately two-hundred times smaller on the total magnetic field than the same displacement for a pancake in the layer where the field is evaluated.

### 3.3.2 Vortex lattice

When the pancakes are perfectly aligned and ordered in an hexagonal lattice one can apply formula 3.12 assuming that there is a single layer in the simulation cell:  $L = d$ ,  $N = 1$  and  $n = 1$ . This eliminates the sum over  $i$  and causes the sum over  $\mathbf{K}_\perp$  to be over the reciprocal vectors of the vortex lattice. The term  $\bar{v}_s$  reduces to

$$\bar{v}^s(\mathbf{k}_\perp, 0) = \frac{1 - e^{-\delta d} - e^{-\delta \frac{d}{2}} + e^{\delta \frac{d}{2}}}{\Delta^2 (1 - e^{-\delta d})} = \frac{1}{\Delta^2}$$

so that the total field is

$$B_z(\mathbf{r}, z) = B_0 \sum_{\mathbf{K}_\perp} \frac{e^{-\frac{1}{2}\xi^2 \mathbf{K}_\perp^2}}{1 + \lambda^2 \mathbf{K}_\perp^2} e^{-i\mathbf{K}_\perp \mathbf{r}} \quad (3.13)$$

where the sum is over the reciprocal vectors of the vortex lattice, including the term  $\mathbf{K}_\perp = 0$  (which, in fact, yields the average field). The Fourier components are exactly those given by Equation 1.18 for continuous vortex lines. This is the simplest model that has been used for  $\mu$ SR fitting.

### 3.3.3 Thermal fluctuations average

We can compute analytically the effect of averaged random fluctuations of straight vortex lines. Because we work in the limit where the fields of each vortex can be linearly superposed, it is sufficient to consider the average field of a single vortex. If  $\delta \mathbf{r}$  is the random

displacement variable around position  $\mathbf{r}$ , then Equation 3.13 yields

$$B_z(\mathbf{r}) = \Phi_0 \int \frac{d\mathbf{k}}{4\pi^2} e^{-i\mathbf{k}(\mathbf{r}+\delta\mathbf{r})} \frac{e^{-\frac{1}{2}\xi^2\mathbf{k}^2}}{1 + \mathbf{k}^2\mathbf{r}^2}$$

so that

$$\langle B_z(\mathbf{r}) \rangle = \Phi_0 \int \frac{d\mathbf{k}}{4\pi^2} e^{-i\mathbf{k}\mathbf{r}} \langle e^{-i\mathbf{k}\delta\mathbf{r}} \rangle \frac{e^{-\frac{1}{2}\xi^2\mathbf{k}^2}}{1 + \mathbf{k}^2\mathbf{r}^2}.$$

Let

$$\delta r^2 \doteq \langle (\mathbf{r} - \langle \mathbf{r} \rangle)^2 \rangle = \langle \delta\mathbf{r}^2 \rangle$$

be the first moment of the probability distribution for  $\delta\mathbf{r}$ . If the effective potential is smooth on the lengthscale  $\delta r$  (small higher-order derivatives), then it can be assumed to be essentially harmonic and the probability distribution Gaussian:

$$p(\delta\mathbf{r}) = \frac{1}{\pi\delta r^2} e^{-\delta\mathbf{r}^2/\delta r^2}.$$

Hence

$$\langle e^{-i\mathbf{k}\delta\mathbf{r}} \rangle = e^{-\delta r^2\mathbf{k}^2/4}$$

(it is just the Fourier transform of the Gaussian distribution). Therefore

$$\langle B_z(\mathbf{r}) \rangle = \Phi_0 \int \frac{d\mathbf{k}}{4\pi^2} e^{-i\mathbf{k}\mathbf{r}} \frac{e^{-\frac{1}{2}(\xi^2 + \frac{1}{2}\delta r^2)\mathbf{k}^2}}{1 + \mathbf{k}^2\mathbf{r}^2}. \quad (3.14)$$

Hence those fluctuations average as an effective coherence length  $\xi_{\text{eff}}$  defined by

$$\xi_{\text{eff}}^2 = \xi^2 + \frac{1}{2}\delta r^2. \quad (3.15)$$

We should stress that this results holds only for the distribution of the field averaged over those fluctuations. It does not hold for static spatial fluctuations. Therefore for a field distribution extracted from  $\mu\text{SR}$  experiment this effects is expected for thermal fluctuations on a timescale smaller than the muon's lifetime.

An analysis of the effects of thermal fluctuations on the field distribution which goes beyond this approximation can be found in [61]. But we will see in the result section that 3.15 is in general a good approximation.

## 3.4 Properties of the model

This model possesses a number of simple properties which can be analytically worked out and are of great help when we try to implement, understand and interpret the simulations. The most important point is to understand how many independent parameters the model possess, so as to avoid performing useless simulations for apparently different parameters which in fact describe the same system. The system that we are interested in is a priori parametrized by three parameters but we will see that in most of the regime that we are interested in, this number reduces to two parameters. We will even need only a single parameter in the whole range over which the interaction between vortices is approximately logarithmic, and the pancakes strongly coupled (Section 3.4.5). The analysis that we make below is specialized to this particular model, but it can be easily linked to the literature by the fact that whenever the discreteness of the layers can be neglected (see Section 3.4.2), our system is perfectly mapped by the 2D Boson model (Section 3.4.3).

### 3.4.1 Scaling

Let  $r_i^a$  be the position of the pancake in the layer  $i$  and in the pile  $a$ . We want to show that the system can be simplified under the assumption that the fluctuations

$$\delta u_n^2 = \langle (r_n^a - r_0^a)^2 \rangle \quad (3.16)$$

on the lengthscale corresponding to  $n$  layers are small compared to the smallest of the two main lengthscales of the system  $\ell_0 = \min(\lambda, a_0)$ :

$$\delta u_n \ll \ell_0. \quad (3.17)$$

The other lengthscales are  $\xi$  and  $r_g$ . The coherence length  $\xi$  does not enter our interaction model. The lengthscale  $r_g$  matters only in the condition of expression 3.3, which will render the following analysis valid only when, in addition,

$$\delta u_n \ll 2r_g. \quad (3.18)$$

The reason for these conditions will be made clear below.

Specifically  $\delta u_n$  must physically be bounded by the fluctuation of non-interacting lines which grows as  $\delta u_n \propto n^{1/2}$  (Section 5.1). The condition 3.17 is therefore always satisfied when

$$C \cdot n \ll \ell_0^2$$

for some constant  $C$  (an explicit expression is given in Section 5.1).

Namely, as will be shown, one can approximate those  $n$  layers with a single layer in the simulation provided a renormalization of the parameters of the system (Figure 3.4). We will often refer to this quantity  $n$  and call it the *number of virtual layers*.

The interaction energy between two pancakes of positions  $r_i^a$  and  $r_j^b$  is of the form

$$E(r_i^a, r_j^b) = U_1(r_i^a - r_j^b)\delta_{ij} + K \cdot (r_i^a - r_j^a)^2 \delta_{ab} \delta_{i(j+1)}.$$

where  $U_1$  was defined in Equation 3.1 and  $K = \varepsilon_1/d$  from Equation 3.3 with

$$\varepsilon_1 = \varepsilon_0 \frac{1 + \ln(\lambda/d)}{4\pi\gamma^2}. \quad (3.19)$$

We remind the reader that  $a$  and  $b$  label the pancake pile (vortex line) and  $i$  and  $j$  label the layer. The Kroenecker deltas come from the restrictions imposed on which pairs interact with which potential (see Figure 3.1). Referring back to Equation 3.3, this expression is valid only when  $r_i^a - r_j^a$  is smaller than  $2r_g$  as specified in the condition 3.18.

Therefore for a configuration  $r$  in  $N$  layers, with periodic boundary conditions along  $z$ , the total energy is

$$H_N(K, r) = \sum_{i=1}^N \left[ \sum_{a,b} U_1(r_i^a - r_i^b) + K \sum_a (r_i^a - r_{i+1}^a)^2 \right].$$

Where the periodic condition is set by defining  $r_{N+1}^a \doteq r_1^a$ . We uses here periodic boundary conditions in order to simplify the notation but everything that follows can be straightforwardly applied to open boundary conditions. From now on we group the layers by clusters of size  $n$ . This is done by writing each layer label as an integer  $k$  times  $n$  plus an integer  $j$  between 0 and  $n - 1$ .  $k$  therefore labels the cluster while  $j$  labels the position within the cluster.

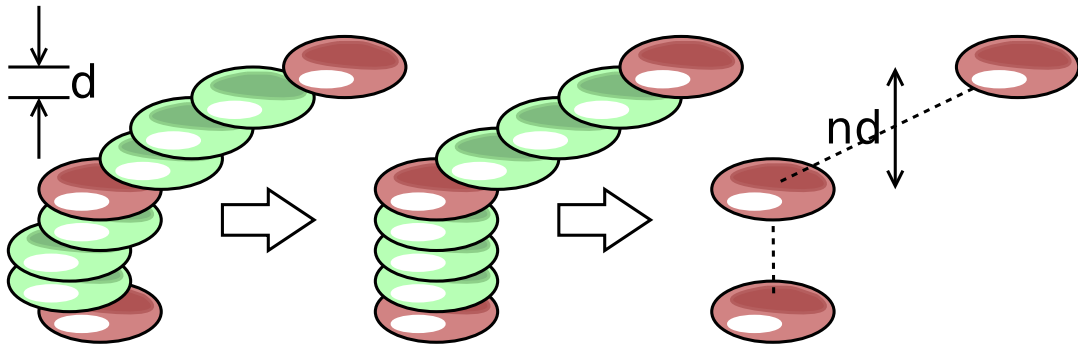


Figure 3.4: Process by which we neglect the fluctuations of intermediate layers, here shown for a single pile. The energy associated with the rightmost configurations of three pancakes is equal to that of the 9 pancakes in the middle, provided that we have correctly modified the constant  $\gamma$  defining the interlayer interaction energy (Equation 3.3). The middle configuration is itself an approximation of the more complex leftmost configuration (it is in fact the ground state of the system in which we fix the positions of the three red pancakes.) What is not shown here are the other piles which interact with this one through the constant  $\varepsilon_0$  (Equation 3.1) which has also to be changed appropriately when the six green pancakes are removed. This process is equivalent to that by which one would approximate a continuous elastic line by a discrete number of vortices linked by straight springs, as explained in Section 3.4.2

Assumption 3.17 which asserts a relative stiffness of the vortex lines over the scale of  $n$  layers allows to write

$$U_1(r_{nk+j}^a - r_{nk+j}^b) = U_1(r_{nk}^a - r_{nk}^b) + \mathcal{O}(\delta u_n/\ell_0)$$

when  $j < n$ . We therefore obtain that

$$H_N(K, u) = \sum_{k=1}^{\frac{N}{n}} \left[ \sum_{a,b} n U_1(r_{kn}^a - r_{kn}^b) + K \sum_{j=0}^{n-1} \sum_a (r_{nk+j}^a - r_{nk+j+1}^a)^2 \right] + \mathcal{O}(\delta u_n/\ell_0).$$

Let us suppose that we want to obtain the average of an observable  $A(r)$  which is approximately constant for fluctuations on the lengthscale  $\ell_0$  so that if properly normalized, say to  $A_n(r)$ , it takes the same value when evaluated on a coarse-grained version of the configuration. Therefore one needs to evaluate the partition function

$$Z_N(\beta, K) = \int \left[ \prod_a \prod_{i=1}^m dr_i^a \right] e^{-\beta H_N(K, r) + \alpha A(r)}$$

Replacing the Hamiltonian by the zeroth order term in  $\delta u_n/\ell_0$  and factoring out of the inner integrals the terms which depend only on the displacements  $r_{nk}^a$  in the layers of indices

multiple of  $n$ :

$$\begin{aligned}
 Z_N(\beta, K) &\simeq \int \left[ \prod_{a,k} dr_{nk}^a \right] e^{-\beta \sum_{k,a,b} n U_1(r_{kn}^a - r_{kn}^b) + \alpha A_n(r)} \prod_{a,k} \int \left[ \prod_{j=1}^{n-1} dr_{nk+j}^a \right] e^{-\beta K \sum_{j=0}^{n-1} (r_{nk+j}^a - r_{nk+j+1}^a)^2} \\
 &= \int \left[ \prod_{a,k} dr_{nk}^a \right] e^{-\beta \sum_k \left[ \sum_{a,b} n U_1(r_{kn}^a - r_{kn}^b) + \frac{K}{n} \sum_a (r_{kn}^a - r_{(k+1)n}^a)^2 \right] + \alpha A_n(r)} \\
 &\quad \times \prod_{a,k} \int \left[ \prod_{j=1}^{n-1} dv_j \right] e^{-\beta K \sum_{j=0}^{n-1} (v_j - v_{j+1})^2} \\
 &= [W_n(\beta K)]^{\frac{M}{n}} \int \left[ \prod_{a,k} dr_{nk}^a \right] e^{-\beta \sum_k \left[ \sum_{a,b} n U_1(r_{kn}^a - r_{kn}^b) + \frac{K}{n} \sum_a (r_{kn}^a - r_{(k+1)n}^a)^2 \right] + \alpha A_n(r)} \\
 &= [W_n(\beta K)]^{\frac{M}{n}} \int \left[ \prod_a \prod_{i=1}^{\frac{N}{n}} dr_i^a \right] e^{-n \beta H_{\frac{N}{n}}(K/n^2, u) + \alpha A_n(r)} \\
 &= [W_n(\beta K)]^{\frac{M}{n}} Z_{\frac{N}{n}}(n \beta, K/n^2)
 \end{aligned} \tag{3.20}$$

where  $M$  is the total number of pancakes in the system, and

$$W_n(\beta) = \int \left[ \prod_{j=1}^{n-1} dv_j \right] e^{-\beta \sum_{j=0}^{n-1} (v_j - v_{j+1})^2}$$

with  $v_0 = v_n = 0$ , is the partition function for a discrete harmonic string of length  $n$  with both ends fixed.

Therefore

$$\boxed{\langle A \rangle = \frac{\partial}{\partial \alpha} \ln Z_N(\beta, K) \Big|_{\alpha=0} \simeq \frac{\partial}{\partial \alpha} \ln Z_{\frac{N}{n}}(n \beta, K/n^2) \Big|_{\alpha=0}} \tag{3.21}$$

We still have to specify what  $A_n(r)$  should be as a function of  $A(r)$ . A general case is when  $A$  is of the form

$$A(r) = \frac{1}{N} \sum_{i=1}^N A(r_i)$$

which means that  $A$  is computed independently in each layer and then averaged over all layers. In the case the coarse-grained version is

$$A_n(r) = \frac{1}{N/n} \sum_{k=1}^{N/n} A(r_{nk}).$$

Because the system is symmetric with respect to translations in the  $z$  direction, those two observables are strictly equal on average. In this work we will encounter many observables of this form; for instance the hexatic order parameter  $\psi_6$  (Section 4.4.2), the Bragg peak intensity (Section 4.4.1), the root-mean-square pancake position fluctuations  $\delta r \doteq \sqrt{\langle (r_i^a - \langle r_i^a \rangle)^2 \rangle}$  (for any  $a$  or  $i$ ), as well as correlations between those quantities.

More general observables are more tricky to coarse-grain. In this work we will not attempt to compute the magnetic field distribution in the context of this approximation. Another important observable is the relative root-mean-square position fluctuations between layers;  $\delta u_n^2 \doteq \langle (r_n^a - r_0^a)^2 \rangle$  (for any  $a$  or  $i$ ). Clearly  $\delta u_m$  with  $m < n$  cannot be coarse-grained because it measures the fluctuations that we are neglecting.

An important point to make here is that Equation 3.21 is not directly valid when the observable is the energy. Indeed the energy is given by varying  $-\beta$  which enters the term  $W_n(\beta)$ . Therefore we have instead

$$\begin{aligned} \langle E \rangle &= -\frac{\partial}{\partial \beta} \ln Z_N(\beta, K) \simeq -\frac{\partial}{\partial \beta} \left[ \frac{M}{n} \ln W_n(\beta) + \ln Z_{\frac{N}{n}}(n\beta, K/n^2) \right] \\ &= \frac{n-1}{n} M k_B T - \frac{\partial}{\partial \beta} \ln Z_{\frac{N}{n}}(n\beta, K/n^2) \end{aligned} \quad (3.22)$$

where  $M$  is the total number of pancakes in the system. Therefore one just has to add this correction of  $\frac{n-1}{n} M k_B T$  coming from the neglected fluctuations.

Before further analyzing the result 3.21 we need to examine what the dimensionless relevant parameters of the problem are. The imposed constant density is characterized by the lengthscale  $a_0$ . The dimensionless parameter characterizing the interaction length is therefore  $a_0/\lambda$ . From 3.1 and 3.3, the interaction is defined by

$$U_1(r) = d \varepsilon_0 K_0(r/\lambda) \quad (3.23)$$

and

$$K = \varepsilon_1/d \quad (3.24)$$

where  $\varepsilon_0$  was defined as

$$\varepsilon_0 = \frac{\Phi_0^2}{2\pi\mu_0\lambda^2} \quad (3.25)$$

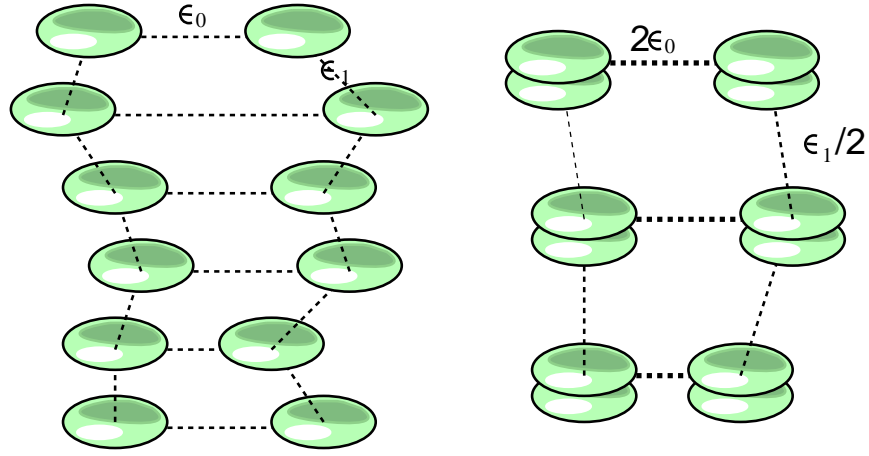


Figure 3.5: Rescaling of the interactions 3.27 with  $n = 2$ . The pancakes on the right are shown doubled in order to illustrate that they represent two pancakes.

and  $\varepsilon_1$  as

$$\varepsilon_1 = \varepsilon_0 \frac{1 + \ln(\lambda/d)}{4\pi\gamma^2}. \quad (3.26)$$

We have shown above that the average of any well-behaved observable is invariant under the transformation sending  $\beta$  to  $n\beta$ ,  $K$  to  $K/n^2$ , and  $N$  to  $N/n$ . Referring back to the full expression of the partition function in Equation 3.20 one can check, using Definitions 3.23 and 3.24, that  $Z$  can be expressed as a function of  $\beta d\varepsilon_0$  and  $\beta\varepsilon_1/d$  rather than  $\beta$  and  $K$ . Therefore the transformation is equivalent to

$$\begin{aligned} \varepsilon_0 &\rightarrow n\varepsilon_0 \\ \varepsilon_1 &\rightarrow \varepsilon_1/n \\ N &\rightarrow N/n. \end{aligned} \quad (3.27)$$

Therefore the effect of the elastic coupling  $\varepsilon_1$  between layers is to effectively strengthen the interactions between pancakes of the same layer by clustering the pancakes in a same stack over a greater lengthscale (Figure 3.5).

The system can be characterized by three dimensionless parameters:  $a_0/\lambda$ ,  $\beta d\varepsilon_0$  and  $\beta\varepsilon_1\lambda^2/d$ . For the last one we could have chosen to use  $a_0$  instead of  $\lambda$  but  $\lambda$  is more convenient for what follows. Since we now have this additional degree of freedom  $n$  under

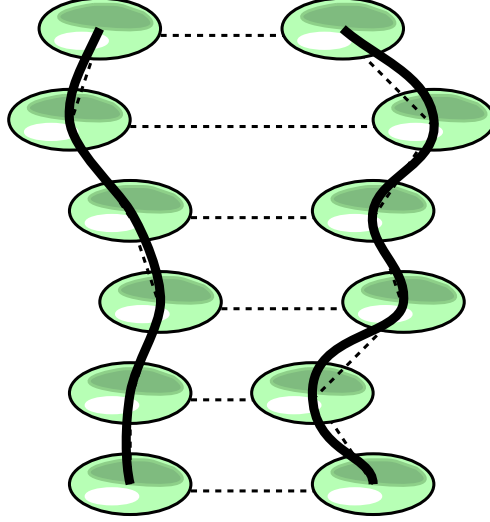


Figure 3.6: Replacing pancake piles by continuous vortex lines.

which the system is effectively invariant, the two last dimensionless parameters really represent a single pertinent parameter invariant under the above transformation:

$$\boxed{\eta^2 = \beta^2 \varepsilon_0 \varepsilon_1 \lambda^2}$$

or

$$\eta = \frac{\beta \varepsilon_0 \lambda}{\gamma} \frac{1}{2\pi} \sqrt{1 + \ln(\lambda/d)} \propto \frac{\beta}{\lambda \gamma} \sqrt{1 + \ln(\lambda/d)}$$

This means that as long as the system is in a regime where the fluctuations between two consecutive layers are much smaller than  $\lambda$  there are only two relevant parameters which can be chosen to be  $\eta$  and  $\lambda/a_0$ .

### 3.4.2 Continuous lines regime

The property defined by Equation 3.21 can be interpreted in a different way. The transformation is equivalent to

$$\begin{aligned} d &\leftrightarrow n d \\ N &\leftrightarrow N/n \end{aligned} \tag{3.28}$$

for an integer  $n \ll \ell_0^2/C$ , and with the change *not* performed for the instance of  $d$  inside the logarithm<sup>4</sup>. Note that the sample thickness  $L = Nd$  is unchanged. If we start with a system with a given spacing  $d$  we can assume that it behaves the same as a system with *more* layers separated by a new spacing  $d'$ . In this case we have  $d' = d/n$ . Now the condition for this to work is just

$$\delta u_1 \ll \min(\lambda, a_0, 2r_g) \quad (3.29)$$

were  $\delta u_1^2 = \langle (r_1^a - r_0^a)^2 \rangle$  is the fluctuations between two consecutive layers separated by the distance  $d$  and  $\ell_0 = \min(a_0, \lambda)$ . Under this condition we can let  $n$  tend to infinity so that the lines become continuous and the Hamiltonian

$$H = \int_{-L/2}^{L/2} dz \left[ \sum_{a,b} \varepsilon_0 K_0 (|r_z^a - r_z^b|/\lambda) + \varepsilon_1 \sum_a (\partial_z r_z^a)^2 \right] \quad (3.30)$$

(were  $\varepsilon_1$  is as defined above with the original  $d$ ). The distance  $d$  essentially disappears (Figure 3.6).

Within this formulation the irrelevance of the ratio between  $\varepsilon_0$  and  $\varepsilon_1$  is revealed by a change of integration variable  $z \rightarrow \alpha z$  for any number  $\alpha$ , which does not change the value of the integral in the limit  $L \rightarrow \infty$ .

### 3.4.3 2D Boson model equivalent

Nelson [62] noticed that the continuous line model is strictly equivalent to a system of interacting two-dimensional bosons.

By using the imaginary time path-integral expression for the partition function of the quantum mechanical system it is easy to check that the expression for the average of an observable is formally identical in both pictures provided that the observable considered treats the time in the boson picture as the  $z$  component in the vortex picture, and the positions of the particles at a given time as the positions of the vortices at a given  $z$ . To complete the identification one has to substitute the bosons worldlines for vortices,  $\hbar$

---

<sup>4</sup>as shown in what follows this transformation allows to totally eliminate  $d$  except from within the logarithm through the dimensionless factor  $\lambda/d$  whose value then becomes the only trace left of the system's initial discreteness

for the inverse temperature  $\beta$ , and  $\beta$  in the quantum model for the thickness  $L$  of the three-dimensional sample.

Therefore a system with infinitely many layers corresponds to the ground state of the bosons. We emphasize that the mean energy in the boson picture has nothing to do with the energy of the vortices.

This may seem computationally advantageous because we deal with a (complex) distribution on the position of  $n$  particles rather than a distribution on the configurations of  $n$  lines. Nevertheless the distribution on the configuration space of  $n$  lines is explicitly given by the Boltzmann weight while the wavefunction of the  $n$  particles has to be obtained by a process of minimization of the energy in the quantum problem.

### 3.4.4 Rescaling

In Section 5.3 we will explore the properties of the system in function of two parameters which will be called  $b$  and  $t$ . They can be interpreted respectively as the average magnetic field and temperature for a system with the same parameters as YBCO at  $T = 0$  ( $\lambda = 1200\text{\AA}$ ,  $\gamma = 7.5$ ,  $d = 11.4\text{\AA}$ ). The difference with the complete model for YBCO is that  $\lambda$  will be kept constant (instead of being temperature-dependant). The reason for this is that it is easier to work with, and interpret the results for, a system with a Hamiltonian which does not depend on the temperature. Whenever this system is effectively in the continuous line regime, where only two parameters are relevant (Section 3.4.2), then the results can be translated in terms of a real field  $B$  and a real temperature  $T$  for a system with any parameters, even a temperature-dependant and field-dependant  $\lambda$ .

Let us assume that  $(b, t)$  is a point of the phase diagram with interesting features (like a phase transition) obtained with constant unprimed parameters  $\gamma, d, \lambda$ . Then the corresponding point  $(B, T)$  for primed parameters  $\gamma', d', \lambda'(B, T)$  is given by solving the coupled equations

$$\begin{aligned} b\lambda^2 &= B\lambda'^2(B, T) \\ \frac{T\gamma'\lambda'(B, T)}{\sqrt{1 + \ln(\lambda'(B, T)/d')}} &= \frac{t\gamma\lambda}{\sqrt{1 + \ln(\lambda/d)}}. \end{aligned} \quad (3.31)$$

The solutions are easily found numerically as needed. This notably allows us to run

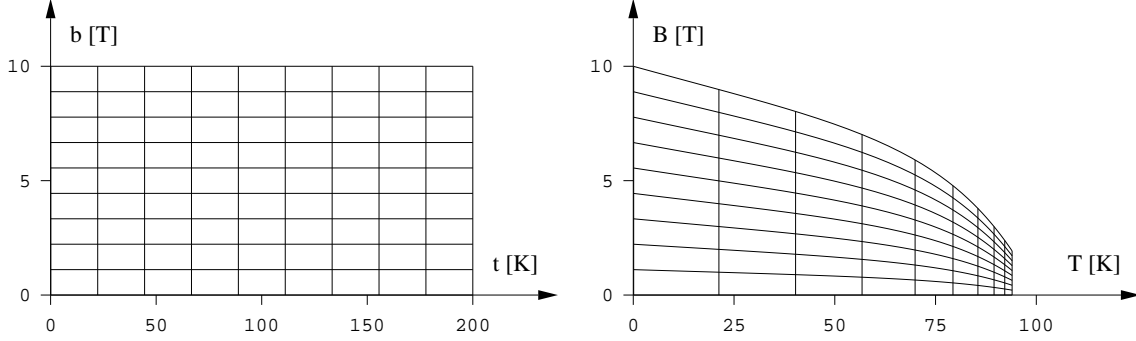


Figure 3.7: Relation between  $b, t$  and  $B, T$  for parameters appropriate for YBCO ( $T_C = 100K$ , and  $\lambda(T)/\lambda(0)$  as in Figure 3.2).

simulations and interpret the results without prior assumption of what the function  $\lambda(B, T)$  should be.

From now on we will call respectively small  $b$  and small  $t$  the parameters corresponding to the average magnetic field and temperature for a model in which  $\lambda$  is fixed at a constant value  $\lambda_0$  ( $\xi$  here is irrelevant because it does not enter the Hamiltonian defined by equations 3.1 and 3.3). In terms of the physical  $B$  and  $T$  those parameters are (this is just a special case of Equation 3.31)

$$b = B \frac{\lambda^2}{\lambda_0^2} \quad (3.32)$$

$$t = T \frac{\lambda}{\lambda_0} \sqrt{\frac{1 + \ln(\lambda_0/d)}{1 + \ln(\lambda/d)}} \quad (3.33)$$

where  $\lambda$  stands for  $\lambda(B, T)$ , dependence which makes the inverse expressions non-trivial. Figure 3.7 demonstrates how a grid in the  $b$ - $t$  plane transforms into to  $B$ - $T$  plane.

### 3.4.5 Logarithmic interaction regime

When the average distance  $a_0$  between the pancakes is much smaller than  $\lambda$ , the potential  $K_0$  (Equation 3.1) can be approximated by a logarithm. The Hamiltonian has the form

$$H = \int_{-L/2}^{L/2} dz \left[ - \sum_{a,b} \varepsilon_0 \ln(|r_z^a - r_z^b|/\lambda) + \varepsilon_1 \sum_a (\partial_z r_z^a)^2 \right]$$

Therefore multiplying all in-plane positions components by a constant scale  $s$  adds an  $s^2$  term in front of the second term and simply factors out as a constant in the logarithmic term. Therefore the Hamiltonian is effectively invariant under the new transformation

$$\begin{aligned} a_0/\lambda &\rightarrow s a_0/\lambda \\ \varepsilon_1 &\rightarrow \varepsilon_1/s^2. \end{aligned}$$

This fact is demonstrated here for the continuous Hamiltonian but it works in exactly the same way for the original Hamiltonian. The above rescaling is independent from the one previously studied (which can take the form 3.27 or 3.28).

In the continuous line regime this links the two parameters  $\eta$  and  $\lambda/a_0$  so that the only relevant parameter left is

$$\Gamma \doteq \eta a_0/\lambda = \beta \sqrt{\varepsilon_0 \varepsilon_1} a_0 = \frac{\beta a_0 d \Phi_0^2}{8\pi^2 \gamma \mu_0 \lambda^2} \sqrt{1 + \log \lambda/d}$$

For instance, if there is a transition at temperature  $t_0 \sim 1/\beta$  and field  $b_0 \sim 1/a_0^2$  then the transition in fact exists for any set of parameters for which  $\Gamma$  has the same value as that with  $b_0$  and  $t_0$ . In terms of just  $b$  and  $t$  this defines a transition line in the  $b - t$  parameter space

$$\boxed{t^2 b = t_0^2 b_0 = \text{cte.}} \quad (3.34)$$

that is  $b \propto t^{-2}$ . This is consistent with the scaling deduced from Equation 5.3 of Ref. [56].

# Chapter 4

## Simulation

All our results are based on averaging observables over the Boltzmann ensemble derived from the Hamiltonian defined by 3.1 and 3.3 with the addition of the disorder field defined in Section 4.5. We obtain those averages by the mean of the Metropolis algorithm, as in Ref. [37]. We used only a single type of Monte Carlo move: the random displacement of a single pancake. Each pancakes always interact with the same two neighbour pancakes in a pile through expression 3.3. Therefore there is no *reconnection moves* which would allow a pancakes to change pile. We do not believe that this is a problem for two reasons. The first one is that we are not specifically interested in a phase where the layers are totally decoupled, as will be made more clear in the result section. The second reason is that this does not restrict the configuration space that we explore. Indeed in a Monte Carlo simulation there is no “time” and therefore no track of the position of an individual particle. The aim of the simulation is only to generate a good sample of static configurations.

Here we will call a Monte Carlo step the *trial* move of as many pancakes as there is in the system, as is traditional.

### 4.1 Correlation times

Figure 4.1 shows microscopic energy values as function of Monte Carlo steps for a system with only a single layer, just at a melting transition; where the dynamic is the slowest. The large oscillations indicate that the system flips from the liquid to the solid phase. This can

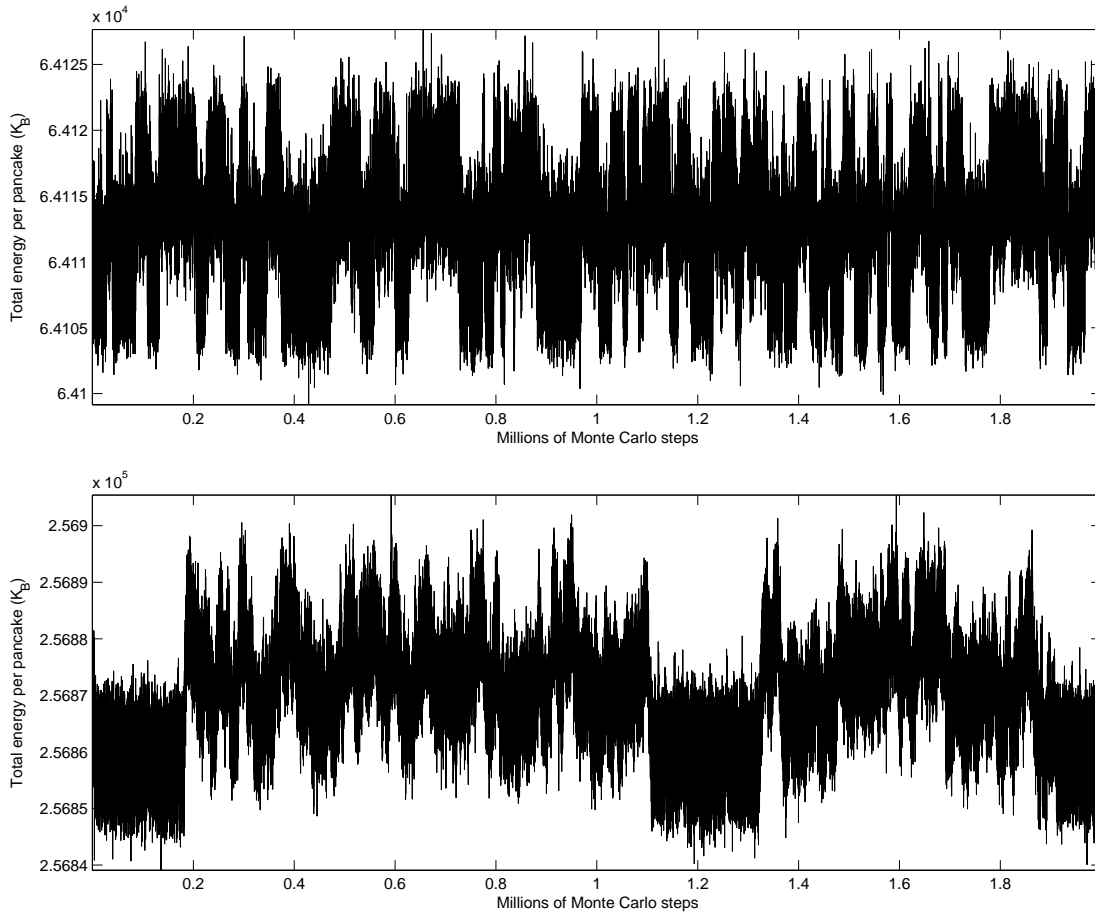


Figure 4.1: Energy time series for the two dimensional system of  $10 \times 10$  pancakes (top) and  $20 \times 20$  (bottom) very close to the transition temperature. In both cases we clearly see the jumps in energy associated with the passage from the liquid to the solid configurations. For the smallest system (top) the jumps happen on a time scale of  $10^5$  Monte Carlo iterations, while it takes  $10^6$  iterations for the large system.

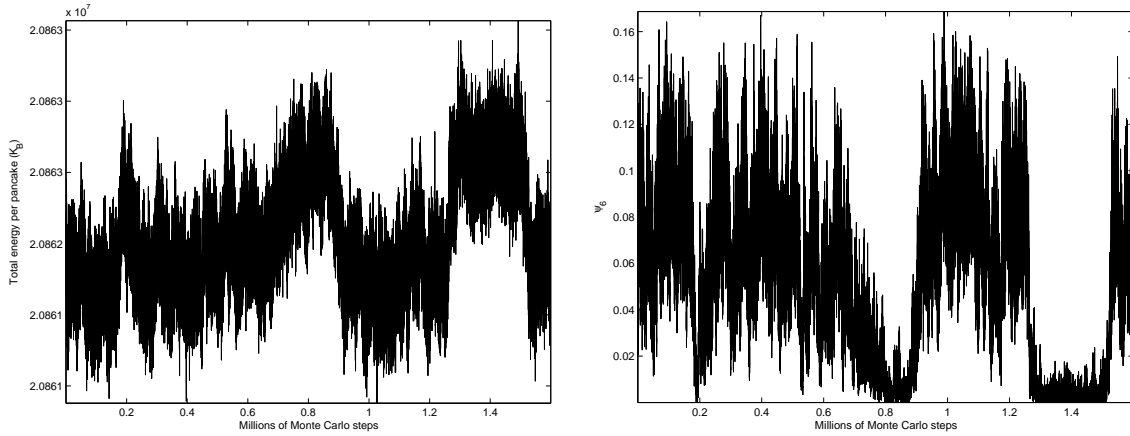


Figure 4.2: Energy time series (top) and  $\psi_6$  time series (bottom) for a three dimensional system of 20 layers and  $8 \times 8$  pancakes per layer, close to the transition temperature. The jumps are associated with the passage from the liquid to the solid configurations. The correlation time is of the order of  $10^6$  iterations.

happens over a long timescale in case of a large system. In order to obtain good statistics for the system of 400 pancakes, one would need to have at least a hundred times the number of iterations it takes for the system to switch between phases; that is  $10^8$  iterations. The smaller system is more tractable as it is 10 times faster. Also the number of steps needed far from the transition is much smaller. A similar time series for the energy as well as for an order parameter are shown for the three-dimensional system in Figure 4.2, also at a melting transition. Because the vortices are extended objects, the number of Monte Carlo steps needed to obtain statistically independent configurations in this case are much bigger than in the two-dimensional case. In general our simulations were done on system of the size of the one in Figure 4.2 with  $10^6$  iterations. This is sufficient far from a transition but certainly not at a transition. In order to study a transition we were greatly helped by the fact the many simulations could be run in parallel at different temperatures across the transition and their results combined using the multihistogram method described in Section 4.3.

## 4.2 Simulation times scaling

A step of the Monte Carlo algorithm involves computing the whole energy of the system. Because in our model each pancakes interact with every other pancakes *in the same layer* then the computational time grows as  $\mathcal{O}(n^2m)$  where  $n$  is the number of pancakes per layers and  $m$  is the number of layers.

## 4.3 Multihistogram method

A single run of the Metropolis algorithm at an inverse temperature  $\beta$  gives valuable information about the density of states over the region of energy explored at this temperature. Indeed the Boltzmann probability distribution over configuration  $x$  is given by

$$p_\beta(x) = \frac{e^{-\beta H(x)}}{Z_\beta}$$

so that the probability for the system to have a given energy  $E$  is

$$\begin{aligned} p_\beta(E) &= \int dx \delta(H(x) - E) \frac{e^{-\beta H(x)}}{Z_\beta} \\ &= \int dx \delta(H(x) - E) \frac{e^{-\beta E}}{Z_\beta} \\ &= \Omega(E) \frac{e^{-\beta E}}{Z_\beta} \end{aligned}$$

where  $\Omega(E) = \int dx \delta(H(x) - E)$  is the density of states. Therefore if the energy histogram  $n_\beta(E)$ , an estimation of  $p_\beta(E)$ , is recorded in the simulation, one can obtain  $\Omega(E)$  through

$$\Omega(E) \propto n_\beta(E) e^{\beta E}.$$

$\Omega$  is determined up to the constant unknown factor  $Z_\beta$ .

In principle this knowledge is sufficient to deduce the energy distribution at any other temperature  $\beta'$  through

$$p'_{\beta'}(E) \propto \Omega(E) e^{-\beta' E}.$$

Nevertheless this will work only for energies for which the initial histogram value  $n_\beta(E)$  was reliably built out of a significant number of events. This is due to the fact that the purpose of the Metropolis algorithm is to explore only a minimal region of configuration space appropriate to a given temperature. Indeed a simple random exploration of the whole configuration space would give  $\Omega(E)$  everywhere but it would require an astronomical number of iterations.

This can be generalized to distribution over any other observable, say  $M$ , by using the histogram over couples  $(E, M)$ ;  $n_\beta(E, M)$ . Indeed one gets

$$\Omega(E, M) \propto n_\beta(E, M) e^{\beta E}$$

and can infer

$$p'_\beta(M) \propto \int de \Omega(e, M) e^{-\beta' e}.$$

Sometimes we need to study the precise temperature dependence of susceptibilities. For instance identifying the maximum value of a susceptibility will give indication on the order of the phase transition or the exact transition temperature. Nevertheless the dynamics of a Metropolis simulation becomes very slow and inefficient precisely at that point. Therefore it can be crucial to extract full information from long runs around the transition. The information that we really want to extract is the density of state  $\Omega(E, M)$  over all values of  $E$  and  $M$  pertinent at the transition. This function allows to deduce the precise temperature dependence of averages or susceptibilities of  $E$  or  $M$  around and at the critical temperature.

We start with a sequence of histograms  $n_i$  obtained from the simulation at inverse temperatures  $\beta_i$  using a number of  $w_i$  iterations. In principle each of these distributions predicts a certain approximation to  $\Omega$ . What is the correct way to combine this information into a single accurate determination of  $\Omega$ ? A simple average does not work because for some points some histograms give more precise information. Similarly any weighted average is not correct either. I will show that the correct distribution  $\Omega$  has to be a solution of the self consistency equation [63]

$$\Omega(E, M) = \frac{\sum_i n_i(E, M)}{\sum_j \frac{w_j \exp(-\beta_j E)}{\int de \exp(-\beta_j e) \int dm \Omega(e, m)}} \quad (4.1)$$

This formula is derived in Annexe A. This equation can be solved by simply iterating it. It converges rather slowly (in some cases we needed over 1000 iterations) though this is not really a problem because each iteration is fast to compute. Nevertheless one has to be careful that, if directly implemented in the above form, floating point variables cannot always hold the resulting values. One has to iterate the equation on the logarithm of  $\Omega$  rather than  $\Omega$  directly. In order to efficiently compute the logarithm of a sum of exponential, we would compute the maximum value of the exponent in the sum and factor this term out of the sum and out of the logarithm. This prevents the sum from becoming enormous before the logarithm is taken.

## 4.4 Observables

Ideally one should compute observables every  $N_O$  Monte Carlo steps where  $N_O$  is chosen big enough so that two successive configurations are statistically independent. In practice most observables are fast to compute so that  $N_O$  can be underestimated without significant loss in performance. We typically used values of  $N_O$  between 10 and 100, except for the computation of the magnetic field which is especially time consuming and could be computed only a few hundredth of time, or less, through a whole run (see Section 5.5.2).

### 4.4.1 Bragg peaks

We computed the in-plane pancake density-density correlation function  $G(x)$  defined as

$$G(x - y) = \langle n(x)n(y) \rangle = \left\langle \sum_{ij} \delta(r_i - x)\delta(r_j - y) \right\rangle$$

where the sum runs over all pancakes and  $r_i$  is the in-plane position of pancake  $i$ . If the pancakes are ordered as an hexagonal lattice in each plane then the Fourier transform of  $G$  possess distinct peaks at the reciprocal lattice positions. The top value of the six peaks of smallest wave-vectors represent directly the intensity of the Fourier components whose periodicity is that of the hexagonal lattice. Because we use a simulation box of finite dimensions, the Fourier transform of  $G$  has a shortest lengthscale (is discrete). For instance if the box is wide enough in a certain direction to be spanned by 8 pancakes in

the hexagonal ordering, then the Bragg peaks will be found at a distance of 8 times this shortest reciprocal lengthscale away from the center of the Fourier transform of  $G$ .

Our simulation box is a rectangle of ratio  $\sqrt{3}$  (see Figure 5.19 for an example of hexagonal lattice fitted in the box). Our system is in principle symmetric under rotation or translation of the vortex lattice as a whole. Therefore the hexagonal ground state can exist with any orientation. Nevertheless the shape of our simulation box together with the periodic boundary conditions force a preferred orientation for the ground state. The triangular plaquettes formed by nearest-neighbours must be orientated so that the triangle points toward the long direction of the box. Therefore the Bragg peaks are always to be found at the same position on the Fourier transform of  $G$  (see Figure 6.8 for an exception.)

#### 4.4.2 Hexatic order parameter

The hexatic order parameter is defined on pancake  $i$  as

$$\psi_6(i) \doteq \frac{1}{6} \sum_{j \in NN(i)} e^{i6\theta_{ij}}$$

where  $\theta_{ij}$  is the angle formed by the bond between pancakes  $i$  and  $j$  and a fixed, absolute and arbitrary direction. The sum runs over the nearest neighbours of the pancake  $i$  in the same layer. A good way to define “nearest neighbourhood” in an arbitrary state would be to use the Delaunay triangulation technique [64]. For simplicity we rather chose to define it as all pancakes within distance of  $1.2 a_0$ . This observable is a complex number of maximum modulus one when all bonds are separated by  $2\pi/6$  radian. The phase codes for an abstract direction of the local structure. The macroscopic observable is the thermodynamical and spacial average of the above.

$$\psi_6^2 = \left\langle \left| \frac{1}{N} \sum_i \psi_6(i) \right|^2 \right\rangle$$

$N$  being the total number of pancakes and the number of terms in the sum.

### 4.4.3 Magnetic field calculation

The magnetic field has been calculated using Equation 3.12. A two-dimensional array was used to store the value of the terms

$$B_z(\mathbf{K}_\perp, z) = \frac{1}{n} \sum_{i=1}^N e^{i\mathbf{K}_\perp \mathbf{r}_i} \bar{v}^s(\mathbf{K}_\perp, z_i - z) e^{-\frac{1}{2}\xi^2 \mathbf{K}_\perp^2} - \delta_{\mathbf{K}_\perp, 1}$$

where the last term is a Kroenecker delta which role is to subtract 1 to  $B(0, z)$ . From Equation 3.12 the real field is then given by a Fourier transform:

$$\frac{B_z(\mathbf{r}, z)}{B_0} - 1 = \sum_{\mathbf{K}_\perp} e^{-i\mathbf{K}_\perp \mathbf{r}} B_z(\mathbf{K}_\perp, z). \quad (4.2)$$

One has to remember that  $\mathbf{K}_\perp$  are a discrete set of values; the reciprocal lattice vectors for the whole simulation box. Discreteness comes from the finite size of the box. The values of  $A(\mathbf{K}_\perp, z)$  above are stored for the smallest values of  $\mathbf{K}_\perp$  up to a cutoff so that the total number of values stored for a given  $z$  will correspond exactly to the number of points of the real field resulting from the Fourier transform. The subtraction of the average comes from the Kroenecker delta in the expression for  $A(\mathbf{K}_\perp, z)$ . This is needed because at high fields the field variations that we are interested in can become very small compared to the average  $B_0$  so that if the field was stored directly, the coding in terms of floating point variables would cause an important loss of accuracy in differences between two field values. By setting the average back to zero we take full advantage of the floating point coding.

The way to compute any type of Fourier transform is to use some version of the Fast Fourier Transform algorithm (FFT)<sup>1</sup>.

The FFT is just a very efficient implementation of the discrete Fourier transform (DFT) which transforms a discrete array  $A_j$  of  $N$  elements into  $\tilde{A}_k$  through

$$\tilde{A}_k = \sum_{j=0}^{N-1} A_j e^{-i2\pi k j / N} \quad \text{for } k = 0 \dots N-1$$

---

<sup>1</sup>Be warned that from our experience the version found in the *Numerical Recipes in C* online book (second edition) by Press *et al.* at “<http://www.library.cornell.edu/nr/bookcpdf.html>” did not seem to work properly. Fortunately many other implementations can be downloaded freely.

(where we now use  $\iota = \sqrt{-1}$  in order to not confuse it with indices). Therefore it transforms an array of length  $N$  into a new array of length  $N$ . This can be generalized to  $N$  dimensions by being applied recursively, which the FFT routine complies to.

When using this to implement Equation 4.2 one has to be a little careful. We chose to store values of  $A(\mathbf{K}_\perp, z)$  for small values of  $\mathbf{K}_\perp$ ; negative and positive. More specifically, for a given  $z$  we built an array

$$A_{ij} = A(2\pi(i - N/2)/L_x, 2\pi(j - N/2)/L_y, z)$$

where  $(L_x, L_y)$  are the dimensions of the simulation box in directions perpendicular to  $\hat{\mathbf{z}}$ . The indices  $i$  and  $j$  run from 0 to  $N - 1$ . This requires  $N$  to be even since the reciprocal vectors components must be integer multiples of  $2\pi/L_x$  or  $2\pi/L_y$  respectively. In terms of  $A_{ij}$ , Equation 4.2 becomes

$$\frac{B_z(\mathbf{r}, z)}{B_0} - 1 = \sum_{ij} e^{-\iota(2\pi(i-N/2)x/L_x + 2\pi(j-N/2)y/L_y)} A_{ij}.$$

This suggests to store  $B_z/B_0 - 1$  into an array of size  $N \times N$ ;  $B_{kl} = B(kL_x/N, lL_y/N, z)$  so that

$$B_{kl} = e^{\iota\pi(k+l)} \sum_{ij} e^{-\iota(2\pi ik + 2\pi jl)/N} A_{ij}.$$

This is indeed a two-dimensional DFT except for the correction term in front which inverts the sign of the real part of the terms for which  $k + l$  is odd.

## 4.5 Disorder Implementation

We implemented the disorder based on a discretized version of Equation 3.5. A discrete version of the random field  $\phi$  can be numerically generated by choosing an independent random number for each discrete point of the field.

In order to reproduce the Gaussian nature of the field, the individual random values of the potential have to be generated according to a Gaussian distribution. We do this using a simple Monte Carlo algorithm which consists in generating random numbers in a box  $[-X, X] \times [0, 1]$  until the point ends up under a normal Gaussian inside the box. Once

this happens the algorithm return the  $x$  value. It is easy to show that this yields  $x$  values according to a normal distribution in the limit  $X \rightarrow \infty$ . Instead we use  $X = 4$  which is a good approximation given the exponential decay of the Gaussian distribution.

We note that a faster and more accurate method was found at item 26 of HAKMEM at URL “<http://www.inwap.com/pdp10/hbaker/hakmem/hakmem.html>”. We quote:

A mathematically exact method of generating a Gaussian distribution from a uniform distribution: let  $x$  be uniform on  $[0, 1]$  and  $y$  uniform on  $[0, 2\pi]$ ,  $x$  and  $y$  independent. Calculate  $r = \sqrt{-\log x}$ . Then  $r \cos y$  and  $r \sin y$  are two independent Gaussian distributed random numbers.

According to Equation 3.5 the random field obtained was convoluted with the function  $f$  defined in expression 3.6. The convolution was performed using three Fast Fourier Transforms (see Section 4.4.3). Indeed a convolution is just a product in Fourier space. Therefore we take the Fourier transform of the two functions, multiply them, and apply the inverse Fourier transform to the result.

The discrete disorder potential so obtained is addressed through bilinear interpolation. Let  $(x_i, y_j)$  be the positions at which the disorder is stored in a given layer, and let  $V_{ij}$  be its value at this point. If the disorder is accessed at position  $(x, y)$ , such that  $x_i < x < x_{i+1}$  and  $y_j < y < y_{j+1}$  then the potential is taken to be the average over the four nearest potential points weighted by a distance to that point:

$$V(x, y) = \sum_{\delta i=0}^1 \sum_{\delta j=0}^1 V_{(i+\delta i)(j+\delta j)} \frac{|x - x_{i+\delta i}|}{x_{i+1} - x_i} \frac{|y - y_{j+\delta j}|}{y_{j+1} - y_j}$$

The discretization size is maintained smaller than the correlation length which is set equal to the coherence length  $\xi$ . This means that the resolution of the disorder landscapes grows as  $L/\xi$  where  $L$  is the linear size of the simulation box. In turns, because the number of vortices is typically left constant,  $L$  grows as  $a_0$ , the average spacing between vortices. Since each vortex carries a quantum of magnetic flux,  $Ba_0^2$  is constant. Therefore  $a_0$  goes as  $1/\sqrt{B}$  and the dimension of the disorder landscape goes as  $1/\sqrt{B}$ . At low fields the number of points to store becomes very large. Therefore we cannot store a different landscape for each layer. We chose to solve this problem by using *the same landscape randomly displaced*

between different layers. The periodic boundary conditions on the disorder field allows for any arbitrary displacement.

## 4.6 Tabulation of the interactions

Depending on the average magnetic field, the simulation box can be comparable or small compared to the range  $\lambda$  of the interaction potential 3.1. Because we use periodic boundary conditions in the directions parallel to the layers, this means that each pancake can interact with many periodic images of each other pancakes. Based on the experience of Ryu *et al.* [37], we decided to tabulate the interaction energy 3.1 as a function of the relative position of two pancakes. This allows us to sum over as many periodic images as needed. For each binned relative position, we proceed to the summation over images up to an exponentially increasing distance and stop when the associated gain in energy drops below a certain level. Typically we stopped the summation when an increase in distance of 50% would yield an energy difference below  $10^{-8}\epsilon_0$ .

Since the position of the pancakes are continuous variables, the interaction table is addressed through linear interpolation, defined in the previous section.



# Chapter 5

## Results I (clean)

We will consider the simulation of systems of increasing complexity. In this Chapter we do not include the disorder in the simulations. In Section 5.1 we study the system when the interaction between vortex lines is turned off, and in Section 5.2 we study the system when the interaction between layers is turned off. Then we proceed with the study of both interactions, still without disorder, and for a non-physical constant value of  $\lambda$  (which should physically depend on  $T$ , see Figure 3.2). This allows us to understand the main properties of the model as well as the limitations of the simulation, which we summarize in Section 5.4. This knowledge is applied to the study of the realistic system, but still without disorder, in Section 5.5. This yields results which can be compared to experiments provided that the temperature is high enough for the disorder to be neglected. We will proceed with the simulation of a system with disorder in the next Chapter.

### 5.1 Decoupled lines

The simplest limiting case is the one in which the pancake piles are not interacting. For small fluctuations a single vortex line behaves like a string of harmonic oscillators. Let  $\delta u_f^2(z) = \langle (u(z) - u(0))^2 \rangle$  the mean square fluctuation of the distance between two pancakes within the same pile separated by a distance  $z$ . One can show using the equipartition

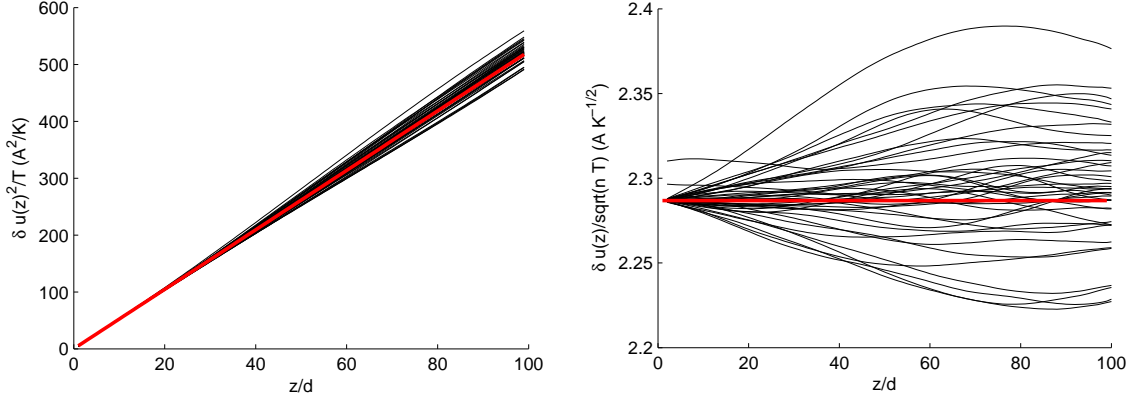


Figure 5.1: Comparison between Equation 5.1 (in red) and a simulation with non-interacting vortex lines in 100 layers with open boundaries and at 42 different temperatures between 1 and 900 Kelvin (in black). The graph on the left represents  $\delta u^2(nd)/T$  versus  $n$  and the one on the right represents  $\delta u^2(nd)/(nT)$  versus  $n$ .

theorem that in the case of an infinite number of layers,

$$\delta u_f^2(z) = \frac{8\pi^2\gamma^2\mu_0k_B T\lambda^2 z}{\Phi_0^2(1 + \ln \lambda/d)} \quad (5.1)$$

Figure 5.1 shows that this equation fits well a simulation with 100 layers and open boundaries, at least up to 900 Kelvin for  $\lambda = 1200\text{\AA}$ ,  $d = 11.4\text{\AA}$  and  $\gamma = 7.5$ , even at the shortest lengthscales.

## 5.2 Decoupled layers

When the interaction between layers is turned off the system is purely two-dimensional. Understanding this special case is a first step toward understanding the full three-dimensional system, but it is also interesting on its own right as we now proceed to discuss (see K. J. Strandburg in Ref. [65] for a review). In general, melting transitions do not have a complete analytical description. The Mermin-Wagner-Hohenberg theorem [66] states that a two-dimensional system with short range interactions cannot have true long-range order

with a continuous symmetry [67]. But it can have a quasi long-range order in which correlation functions decay more slowly with distance than expected in a true solid (i.e as  $r^{-\eta(T)}$  where  $r$  is the distance and  $\eta(T)$  a temperature-dependent exponent) [65]. In a small system with periodic boundary conditions such a phase appears as fully ordered in the sense that correlations functions do not have enough room to significantly decay. The Kosterlitz-Thouless-Halperin-Nelson-Young (KTHNY) theory predicts a two-step melting of such a two-dimensional isotropic (hexagonal) solid [65]. The first step is a Kosterlitz-Thouless (KT) transition caused by the appearance of dislocations which preserve bond angles but disturb positional order. The resulting intermediate phase, the so-called hexatic phase, is characterized by long-range bond-angle correlations. This order is then destroyed by a second KT transition. Depending on the particular system other scenarios are possible. One seems to need simulations of very large dimensions in order to observe characteristics of a KTHNY transition as in the hard-sphere simulation by Jaster *et al.* [68] or the Lennard-Jones simulation by Chen *et al.* [69].

It is here important to remind the reader that the interaction we use is *not* the physical effective electromagnetic interaction that we would find between two pancake vortices in a thin film. Indeed, for computational purpose we summed out the screening coming from the interaction between pancakes in different layers and in different “stacks” so that we do not have to perform this sum numerically (see Chapter 3). The summation assumed that the pancakes were aligned within a stack. The true interaction in a thin film would be logarithmic up to a much greater distance than  $\lambda_{\perp}$  and then would decay as one over the distance [10]. Also if we were to use the full magnetic interaction between layers with no Josephson interaction as computed by Clem [10] and if the effect of pancakes in different layers were to compensate each other (which is plausible at high field) then the interaction would be logarithmic to all scales.

Figure 5.2 shows the transition temperatures obtained with the simulation of decoupled layers. It is signaled consistently from the divergence of the root-mean-square relative pancake displacement between nearest neighbours in a layer ( $\delta u_{\perp}$ ) and the suppression of the Bragg peak intensity, as shown in Figure 5.3. The fluctuations of the Bragg peak intensity at the transition, seen in Figure 5.3, are caused by a slow simulation’s dynamics at the transition and the rather large range of temperature over which the system can

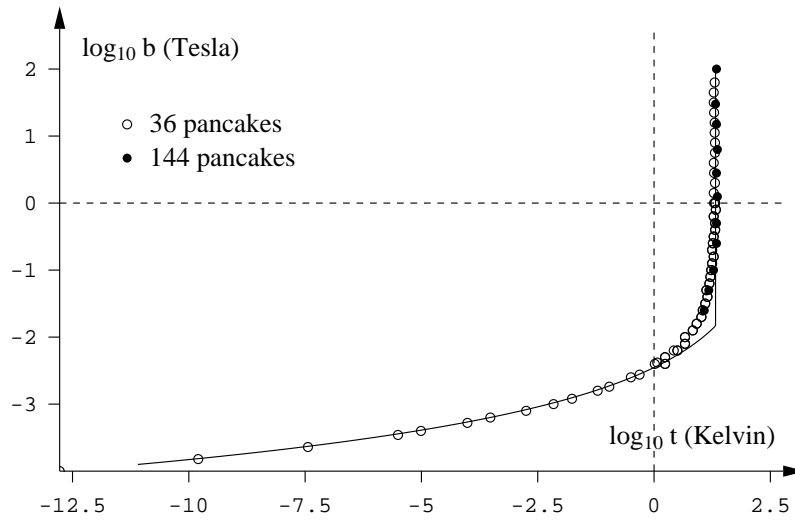


Figure 5.2: 2D transition temperature as a function of field as determined by the mean-square fluctuations on a 36 and 144 pancakes, single layer system with periodic boundary conditions. The solid line is a rough fit composed of a linear and an exponential part of the form  $t \simeq e^{-c/\sqrt{b}}$  for some constant  $c$  (this is the functional form of the interaction potential for a distance proportional to  $a_0 \sim 1/\sqrt{b}$ , when  $a_0 \ll \lambda$ ). It will be used as a model of this 2D melting. The edge in the solid line is due to the fact that this fit does not account for the smooth crossover between the two limiting regimes.

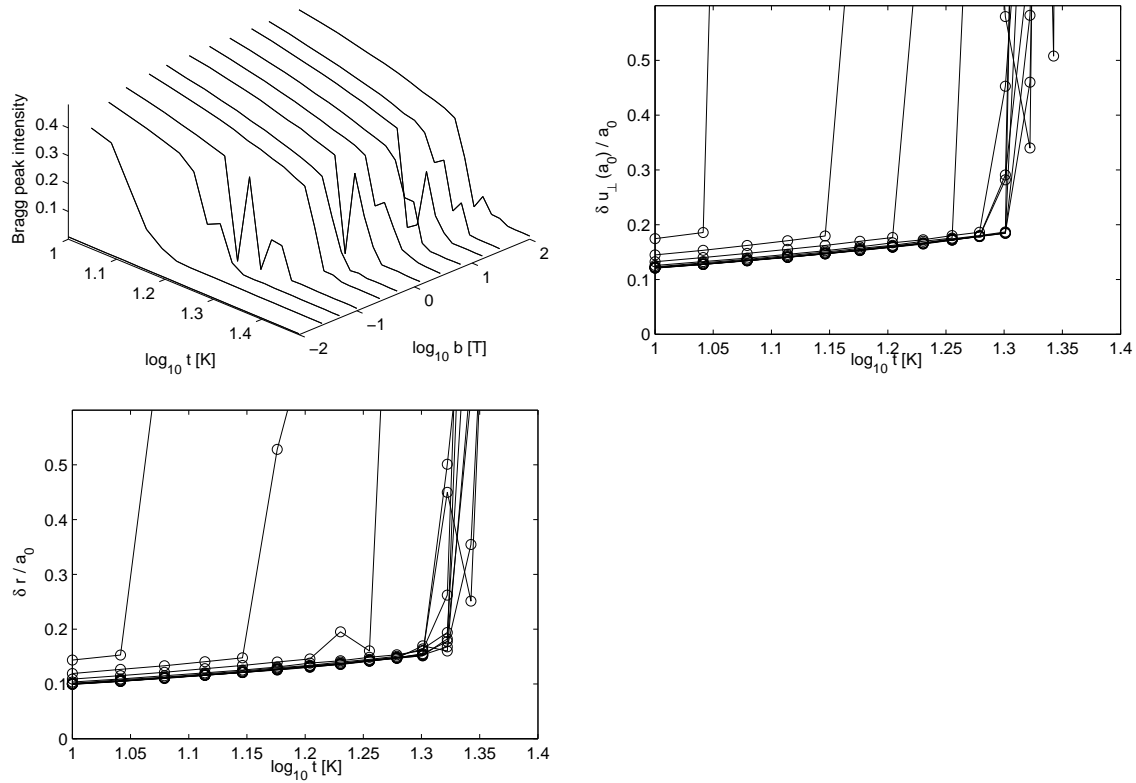


Figure 5.3: Bragg peak intensity (up-left), root mean square relative displacements between nearest neighbours in a layer (up-right) and root mean square fluctuations of the pancakes about their average position  $\delta r$  (bottom), as function of field and temperature for a single-layer system of 144 pancakes. Those data served to produce the 144 pancakes data points on Figure 5.2.  $\psi_6$  was not calculated for this dataset. From the bottom figure we see that the Lindemann constant (the value of  $\delta r / a_0$  at which the system melts) should be around 0.15.

slowly switch from the liquid to the solid state and back; the *coexistence region*, as seen in the histograms on Figure 5.6. The fact that we *see* it oscillating comes from the unusual approach that we use which consists in running independent simulations at each temperatures across the transition temperature instead of obtaining the same data with a sweep in temperature of a single simulation. The later method would result in hysteresis, because the system which is badly equilibrated tends to stay in the state in which it was at the previous temperature. In our case bad equilibration translates into those oscillations instead.

The melting temperature depends on the size of the lattice but not in a way which would be significant on this logarithmic scale (see figures (5.4) and (5.5) for a more precise picture of the dependence, up to 400 pancakes).

This curve has been calculated for  $\lambda = 1200\text{\AA}$  so that the crossover field value  $b_0 \sim \Phi_0/\lambda_0^2 \simeq 0.14$  T separates the logarithmic from the exponential interaction region. In the logarithmic region (high fields), the transition temperature is independent of the field. The transition temperature of 20 K is consistent with estimations using the Kosterlitz-Thouless melting theory for a fully logarithmic interaction as in Ref. [3]. At low field in the exponential region the transition temperature falls off exponentially as the field is lowered.

It is easy to understand why the transition temperature is independent of the field in the regime where the interaction is logarithmic; the average field enters the problem only by setting a lengthscale which has the same effect as a factor in the logarithm's argument (in the Hamiltonian term 3.1 and referring to the approximation 1.20). This factor can be pulled out of the logarithm and appears only as a constant energy term which has no physical effect.

The order of the transition can be studied by analyzing how the susceptibility of an order parameter or the heat capacity, depends on the d-dimensional volume of the system [70]. If the phase transition is first order in the thermodynamic limit then (once the system reaches a sufficient size) the maximum value of the heat capacity at the transition should grow linearly with the size of the system. This is directly related to the fact that there must be a finite energy jump per unit volume associated with the transition in the thermodynamic limit (the latent heat). The same linear behaviour should be observed for

the susceptibility of an order parameter. Another signature of a first-order transition is the scaling of the free energy barriers between the two phases. For a finite size system the probability distribution in energy near the transition will show two distinct bumps, each corresponding to a population of states belonging to a different phase. The ratio of probability between the minimum at the midpoint between the peaks and the maximum of the peaks (at the temperature where both peaks are of equal size) gives the value of the free energy barrier between the two phases. In the first-order transition picture this difference of free energy should be directly related to the free-energy cost associated with the creation of interfaces between the two phases. If  $L$  is the linear dimension of a  $d$  dimensional system, the size of the interfaces grow as  $L^{d-1}$ . Therefore the free energy barrier  $\Delta f$  should grow as  $L^{d-1}$  (Lee and Kosterlitz [71]).

Figure 5.4 shows the result of this analysis above the field  $b_0$  for which  $a_0 \sim \lambda$  and Figure 5.5 shows the low field behaviour. In both cases the scaling of the heat capacity is fully consistent with a first-order transition. On the other hand the behaviour of the free energy barrier is surprisingly oscillatory. Multiple runs have confirmed that this behaviour is not random or due to poor equilibration, as shown by the moderate size of the error bars. The cause of those oscillations is not understood and should be investigated. They might be linked to the constraint imposed by the shape of the unit cell on the elastic excitations. Indeed we use a rectangle unit cell which destroys many natural symmetries of the lattice. An hexagonal unit cell for instance would be more appropriate. Alternatively we cannot rule out the possibility that this effects comes from a hidden intermediate hexatic phase if the KTHNY theory is applicable. In any case the linear scaling of the heat capacity alone is a strong signature of a first-order phase transition [71].

Figure 5.6 show the evolution of the energy histograms across the transition below and above the field  $b_0$  for which  $a_0 \sim \lambda$ . One can see that there is a finite range of temperatures at which the system can have either the energy of the melted phase or the energy of the solid phase. In the simulation this translates as a very slow dynamics. The system stays in one of the phases over many iterations and suddenly “tunnels” to the other state, with a typical switching time of a million of iteration for the biggest system (Figure 4.1).

In order to go further we would like to measure the correlation function of the hexatic order parameter. Because  $\psi_6$  is defined only on top of the pancakes there is no obvious

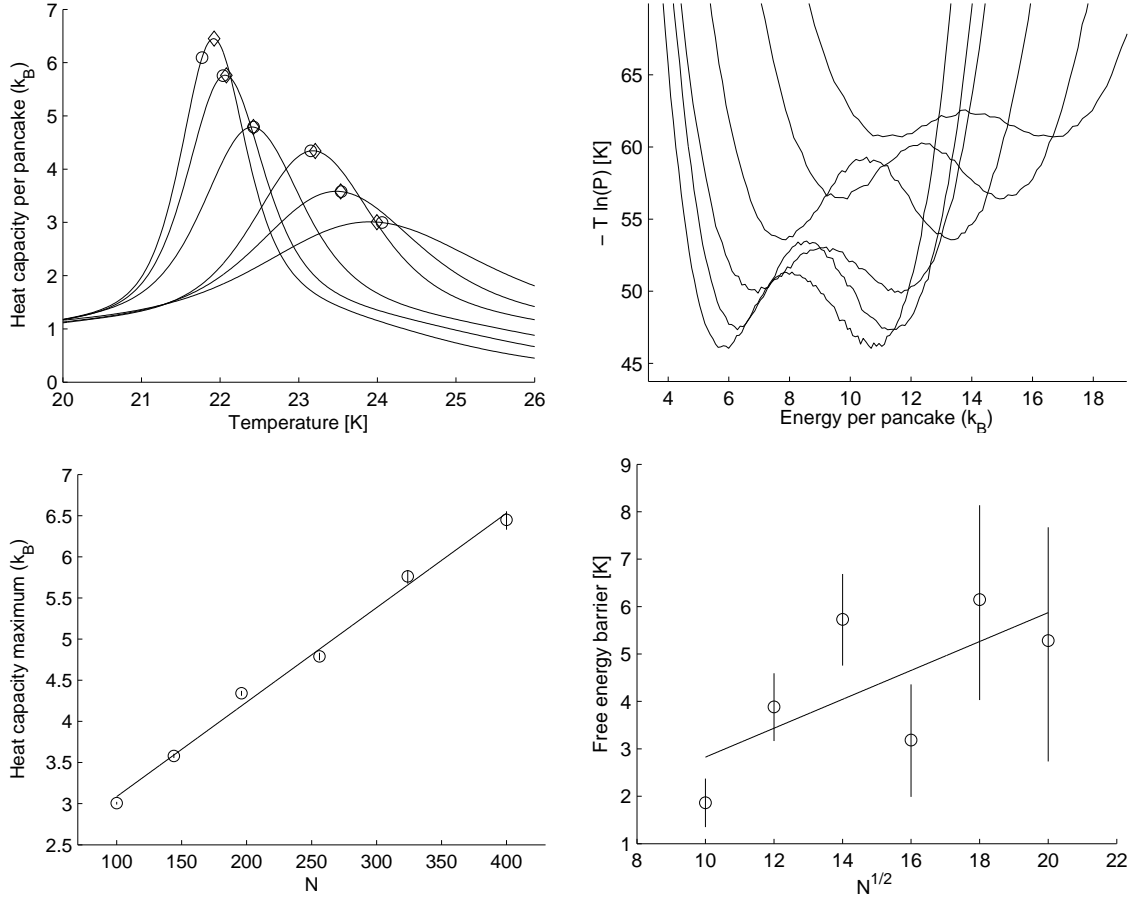


Figure 5.4: 2D transition scaling in the logarithmic regime at  $b = 1$  T (or  $B = 0.68$  T for YBCO parameters, see Section 5.2.1). The upper-left graph represents the heat-capacity per pancake as function of temperature for various system sizes (increasing from the rightmost curve to the leftmost). The circles indicate the temperature at which the simulations have been run. The lower-left graph shows the maximum heat-capacity as function of system size. The upper-right graph shows a quantity proportional to the free energy as function of energy at a temperature  $T_0$  and for various system sizes ( $P(E)$  is the probability distribution in energy). For each system size  $T_0$  is chosen as the temperature at which the two local minima of the free energy are equal. These temperatures are indicated by the diamonds on the upper heat-capacity graph, showing that they are also the temperatures at which the heat-capacity is maximum. The bottom-right graph shows the scaling of the difference between the local maxima and the local minima in the free energy as function of system size. This quantity is interpreted as an evaluation of the free-energy barrier between the two phases. Those results have been obtained by combining, for each system size, the results of 31 independent simulations with  $10^5$  equilibration iterations and  $2 \cdot 10^6$  averaging iterations, for a total of  $6.2 \cdot 10^7$  Monte Carlo iterations.

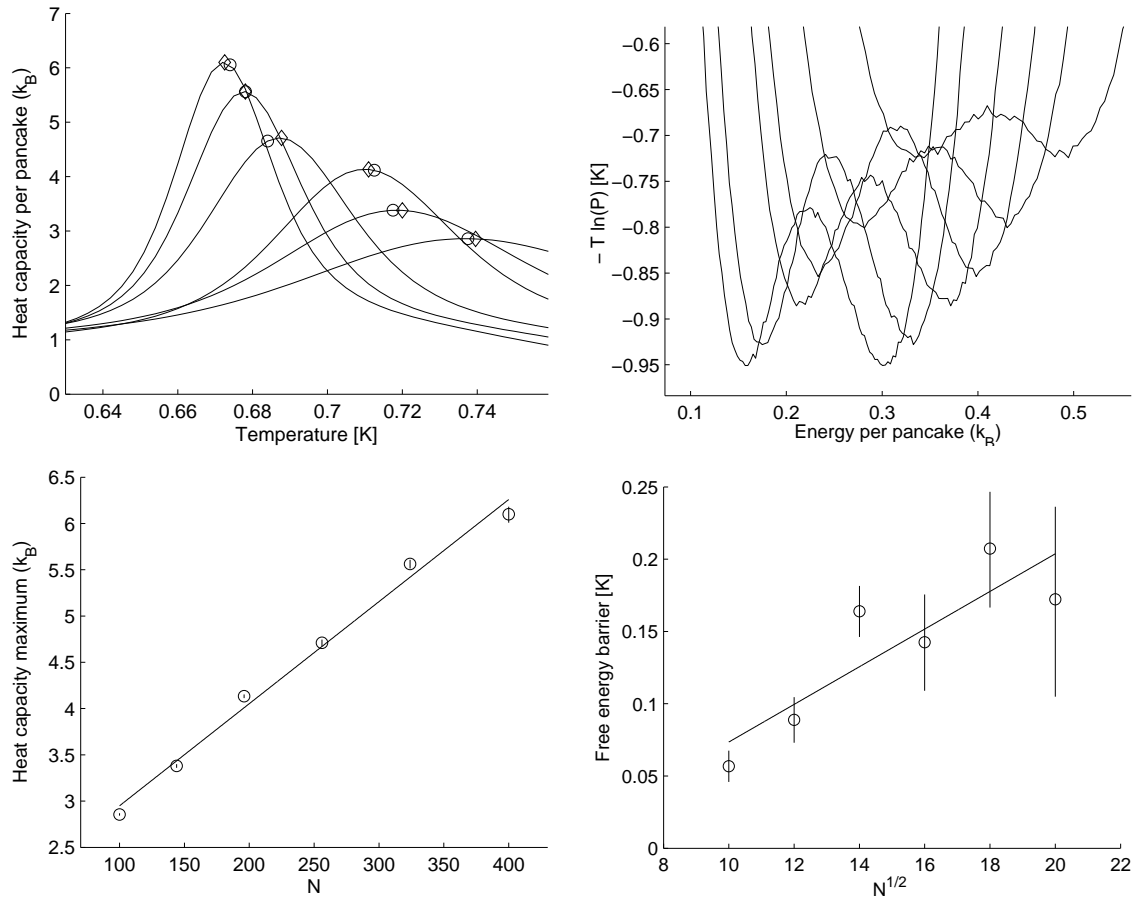


Figure 5.5: 2D transition scaling in the exponential regime at  $b \simeq 3.2$  mT (or  $B \simeq 2.2$  mT for YBCO parameters, see Section 5.2.1). See also comments for the scaling at  $b = 1$  T (Figure 5.4).

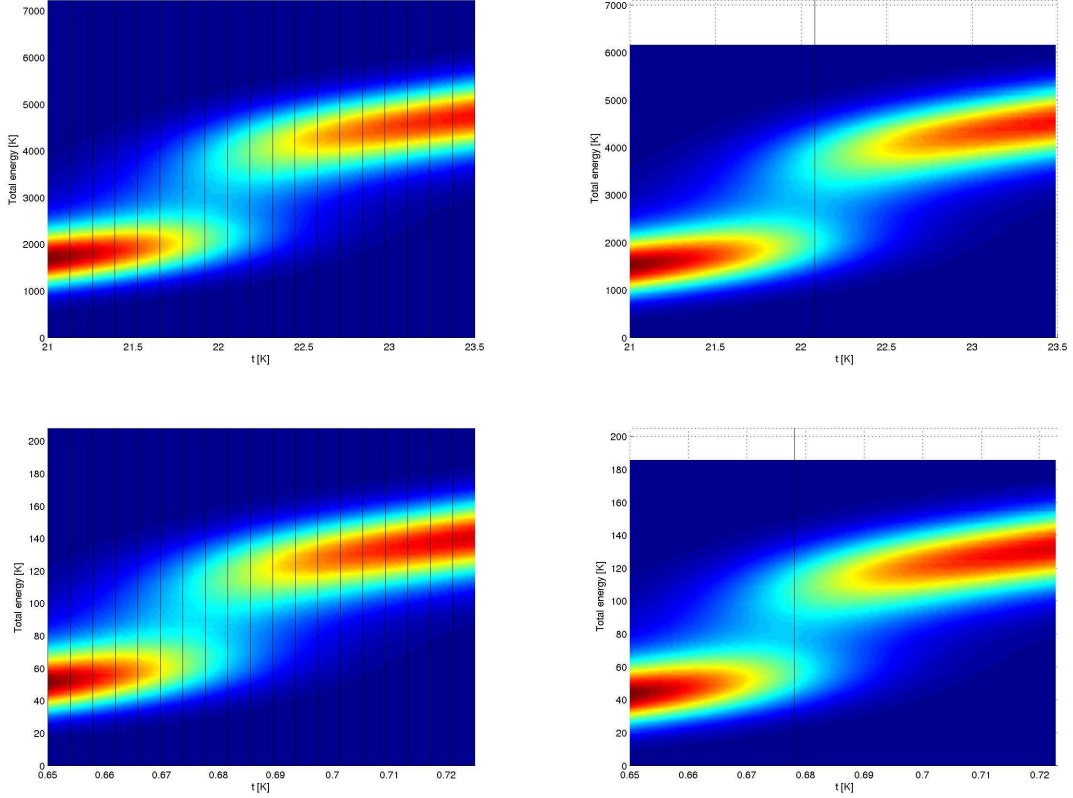


Figure 5.6: Energy histograms around the two-dimensional melting transition at two different fields with a system of 324 pancakes, interpolated from a discrete number of simulations using the multihistogram method. The graphs on the top were done at a field largely in the logarithmic interaction region ( $b = 1$  T or  $B = 0.68$  T for YBCO parameters) and the bottom graphs were computed in the exponential interaction regime ( $b \simeq 3$  mT or  $B = 2.2$  mT for YBCO parameters). The vertical black lines indicate the actual temperature at which the simulation was run; all other temperatures are interpolations using the multihistogram method (see Appendix A). Those diagrams show no trace of a third intermediate phase as predicted by the KTHNY theory.

meaning to a field  $\psi_6(r)$  other than

$$n(r)\psi_6(r) \doteq \frac{1}{N} \sum_i \delta(r - r_i)\psi_6(i)$$

where  $n(r)$  is the number density of vortices at position  $r$ . Assuming that there is no correlation between  $n(r)n(0)$  and  $\psi_6(r) \cdot \psi_6(0)$ , the correlation function

$$C(r) \doteq \langle \psi_6(r) \cdot \psi_6(0) \rangle - \langle \psi_6(r) \rangle \cdot \langle \psi_6(0) \rangle$$

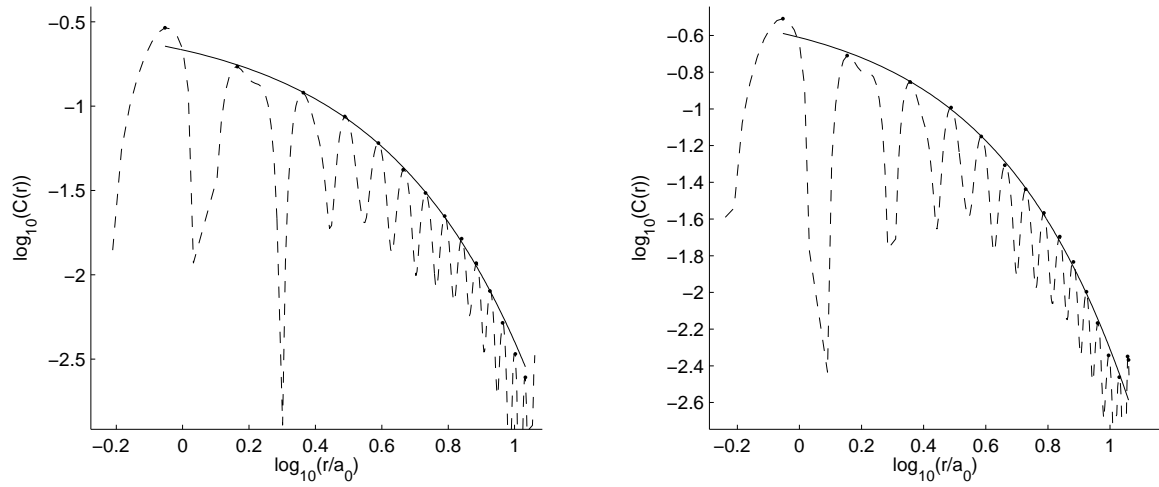
can be computed as

$$C(r) \simeq \frac{\langle n(r)n(0) \psi_6(r) \cdot \psi_6(0) \rangle}{\langle n(r)n(0) \rangle} - \langle \psi_6(r) \rangle \cdot \langle \psi_6(0) \rangle$$

where the product  $x \cdot y$  is defined as the real part of  $x\bar{y}$  ( $\bar{y}$  is the complex conjugate of  $y$ ), which is just the dot product of the complex numbers seen as two-dimensional real vectors. Nevertheless data show that the assumption of the absence of correlation between  $n(r)n(0)$  and  $\psi_6(r) \cdot \psi_6(0)$  is wrong, even at local correlation maxima, because  $C(r)$  as above defined becomes negative at large distances in the liquid phase instead of tending to zero. Therefore we had to add an unknown constant in the expression for  $C(r)$ :

$$C(r) \simeq \frac{\langle n(r)n(0) \psi_6(r) \cdot \psi_6(0) \rangle}{\langle n(r)n(0) \rangle} + C_0 \quad (5.2)$$

The intermediate phase of the KTHNY theory should be characterized by a power law, rather than exponential, decay of the correlation function. Figure 5.7 shows the behaviour with distance of the  $\psi_6$  correlation function in the liquid phase at a temperature just sufficient to avoid the temperature region over which the system can be found in both the liquid or the solid state, which can be seen in Figure 5.6 as the region over which the histograms contains two bumps. The analysis has not been done within this coexistence regime because the existence of the ordered phase would hinder interpretations. The exponential decay of the correlations shows that the disordered phase identified has no orientational order and is therefore not an hexatic phase.



$b = 1 \text{ T}, t = 23.5 \text{ K}$

$b \simeq 3 \text{ mT}, t = 0.72 \text{ K}$

Figure 5.7: Behaviour with distance of the  $\psi_6$  correlation function  $C(r)$  defined by 5.2, in the liquid phase at a temperature just sufficient to avoid the phase coexistence. The smooth line is a fit of the bumps maxima to an exponential decay. The constant  $C_0$  was included as fitting parameter. The good quality of the fit indicates that there is no bond-angle order in this phase. The system contained 400 pancakes.

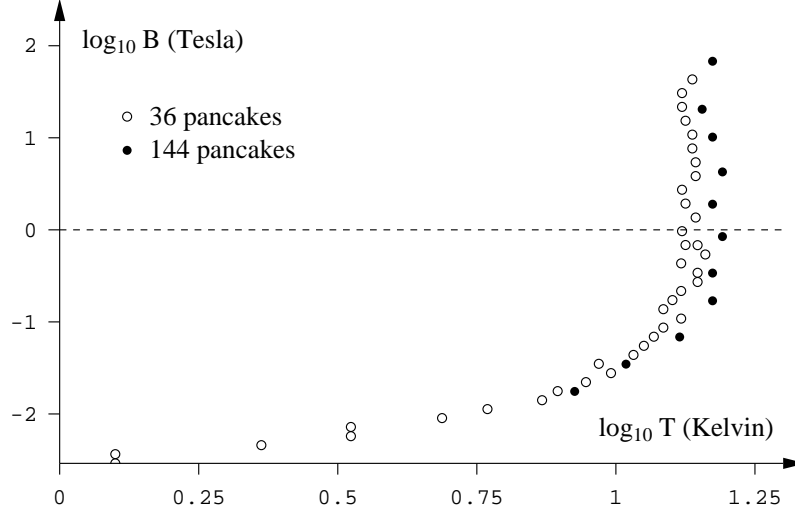


Figure 5.8: Part of the data in Figure 5.2 transformed as to account for YBCO parameters with a  $\lambda$  dependent of temperature, as in Figure 3.2.

### 5.2.1 Conversion to other parameters

We want to show that the above results for the two-dimensional system can be adapted to any other values of the parameters. Indeed we explored both  $b$  and  $t$  which covers all the physics contained in the system. Indeed the Hamiltonian 3.1 is characterized only by two dimensionless parameters which can be chosen to be  $a_0/\lambda$  together with

$$d\beta\epsilon_0 = \frac{d\beta\Phi_0^2}{2\pi\mu_0\lambda^2}.$$

Therefore the phase diagram 5.2 can be converted in terms of  $d\beta\epsilon_0$  and  $a_0/\lambda$  instead of  $b$  and  $t$ . A new  $b$  and  $t$  can be extracted from the graph for different values of  $\lambda$  or  $d$  simply by applying the reverse equations, in a way very similar to what we did in Section 3.4.4. This amounts to solving the equations

$$\begin{aligned} \frac{a_0}{\lambda} &= \frac{a'_0}{\lambda'} \\ \frac{d\beta\Phi_0^2}{2\pi\mu_0\lambda^2} &= \frac{d'\beta'\Phi_0^2}{2\pi\mu_0(\lambda')^2} \end{aligned}$$

to convert the unprimed set of parameters to the primed one.

An example for YBCO<sup>1</sup> is shown in Figure 5.8. We see that the effect is a slight shift toward lower temperatures. The high field melting temperatures becomes 13.7 Kelvins instead of 20 Kelvin.

Also observables with the unit of energy can be expressed in terms  $d\epsilon_0$  and observables with unit of length can be expressed in terms of  $a_0$  so that the resulting numerical values are independent of a particular choice of  $\lambda$  or  $d$  which serve only to define those units.

This will be used particularly in Section 5.4 where we will make use of the knowledge of the two-dimensional phase diagram in order to predict the behaviour of the three-dimensional simulation.

### 5.3 Melting with constant $\lambda$

We now want to turn on the interaction between layers. The simulation can handle only a finite number of layers  $N$ . The maximum value which could be reasonably handled with the computer power at our disposition was between  $N = 20$  and  $N = 100$  depending on the problem. Unlike the number of pancakes per layer, the number of layers can totally change the qualitative behaviour of the simulation. We will see that, depending on the field, temperature and other parameters, there is a lower bound on the number of layers needed in order to obtain a behaviour qualitatively consistent with that of an infinite number of layer. This bound can become quiet large and even diverge for parameters of interests. This will require the use of an approximation method based on the analysis of Section 3.4.1, which allows to obtain the correct observable using only a fraction of the physical number of layers. Unfortunately this approximation method is subject to other limitations that restrict its usage only to certain domain of the parameter space, putting some regions out of reach of the simulation as it stands. A detailed analysis will be presented in the next section. In this section we present preliminary results which will motivate the following analysis.

---

<sup>1</sup>The change has been to use a temperature-dependent  $\lambda$  (as in Figure 3.2) together with  $\lambda(0) = 1400\text{\AA}$  rather than  $1200\text{\AA}$ , so that it can compare to the results from Aegerter *et al.* for the 3D system [21]

### 5.3.1 Three types of transitional behaviours

We chose at first to perform simulations with  $\lambda$  constant at all temperatures instead of including a more physical  $T$ -dependence which would require it to diverge at the superconducting transition (see Sections 1.1.2 and 3.1). We made this choice in order to understand the various regimes that the simulation can encounter without the additional complexity introduced by an effective Hamiltonian which varies with temperature as is the case if we include the temperature dependence of  $\lambda$ .

We note that, even though we do not consider here the dependence of  $\lambda$  on  $T$ , some of the results that we will obtain will apply for the system with a realistic  $\lambda(T)$ , as explained in Section 3.4.4.

Figure 5.9 shows observables over a wide region of the  $b$ - $t$  plane obtained for a simulation with  $N = 8$  layers for parameters adapted to YBCO at  $T = 0$ ;  $\lambda = 1200\text{\AA}$ ,  $\xi = 20\text{\AA}$ ,  $d = 11.4\text{\AA}$  and  $\gamma = 7.5$ . The Bragg peaks disappears at high temperature, indicating a loss of the long-range crystalline order like for the two-dimensional system. Here on the other hand we see that the system gets disordered by either increasing or lowering the field. The graphs showing the line wandering  $\delta u(L)/a_0$  ( $L = Nd$  is the thickness of the simulation box) indicates that the transition at high field is of a different nature than the low field one, given that it happens together with a distinct kink in the line wandering. This jump in  $\delta u(L)/a_0$  indicates that the melted phase is characterized by a greater freedom of the vortex lines which are then allowed to wander across several sites (typically separated by the average distance  $a_0$ ), and therefore entangle with each other. Another way to view it is as a loss of correlation between two ends of a vortex line.

Furthermore at even higher field we also see a kink in  $\delta u(d)$ , the root-mean-square fluctuations between neighbouring pancakes in the same pile, indicating yet another behaviour. The transition now frees two *neighbouring* pancakes in a pile. This behaviour may not be only the same as the one above with a shorter correlation length, but a quantitatively different process as the discrete nature of the piles become, here, relevant.

On the other hand the reentrant transition at low field is *not* associated with any feature in  $\delta(L)$ , which instead stays smaller than  $a_0$ .

This shows that the lowest transition leads to an *unentangled liquid* were the vortex lines move freely with respect to each other but stay straight in average [62]. The transition

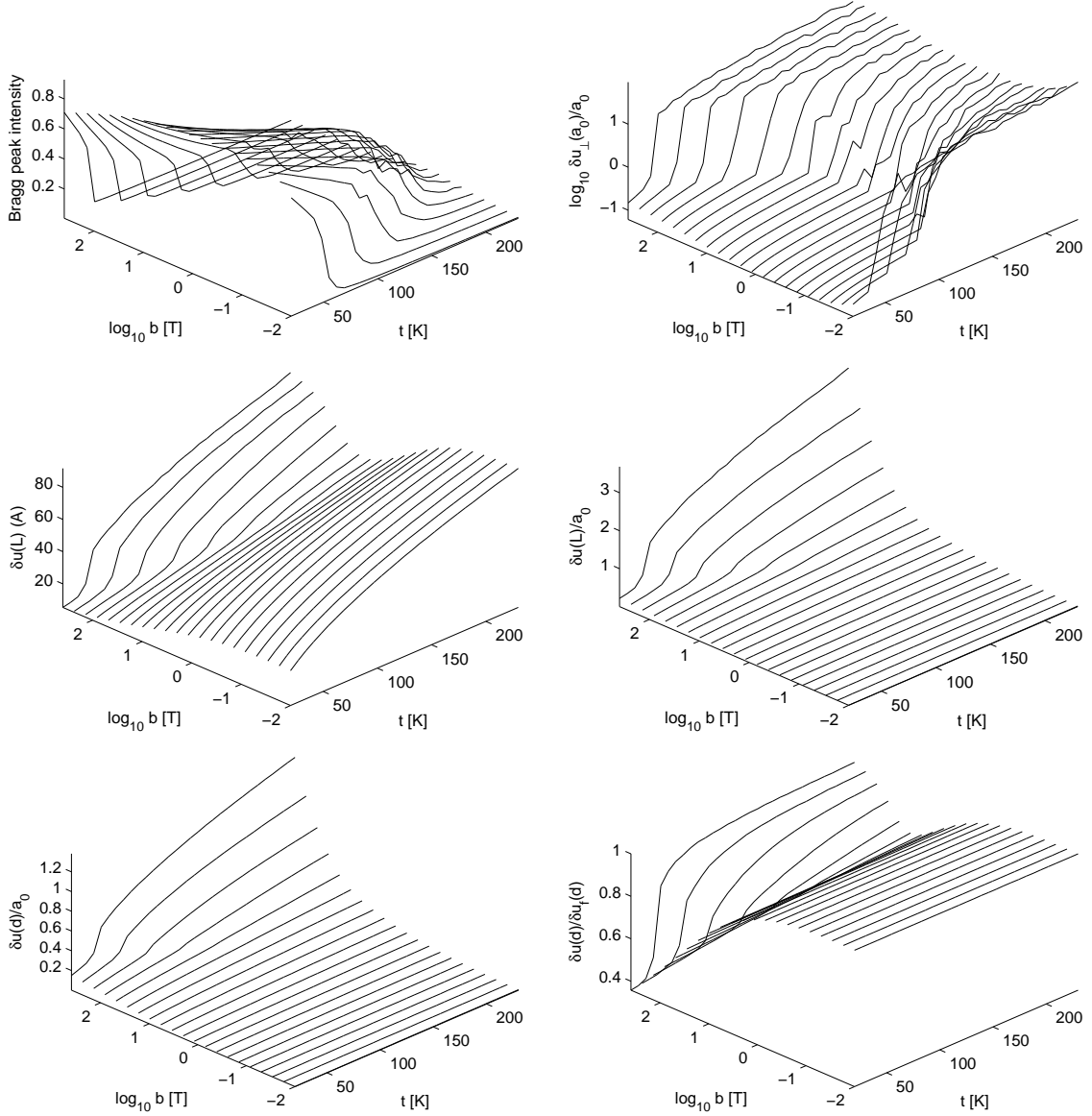


Figure 5.9: Various observables as function of  $b$  and  $t$  for a system of 8 layers and 64 pancakes per layers.  $\delta u_{\perp}(a_0)$  stands for the RMS in-plane relative nearest-neighbour displacement (Equation 3.8).  $\delta u(d)$  is the RMS displacement between pancakes in the same stack but in successive layers and  $\delta u(L)$  is the RMS displacement between pancakes in the same stack but in opposite layers through the sample, or the *line wandering* through the sample (Equation 3.16, with  $\delta u(nd) = \delta u_n$ ).  $\delta u_f(z)$  is the same physical quantity as  $\delta u(z)$  but specifically for non-interacting vortex lines (Section 5.1). Notice the kink in the line wandering associated with the melting at high field. Also the kink in  $\delta u(d)$  at high field indicates a melting with decoupling of the layers.

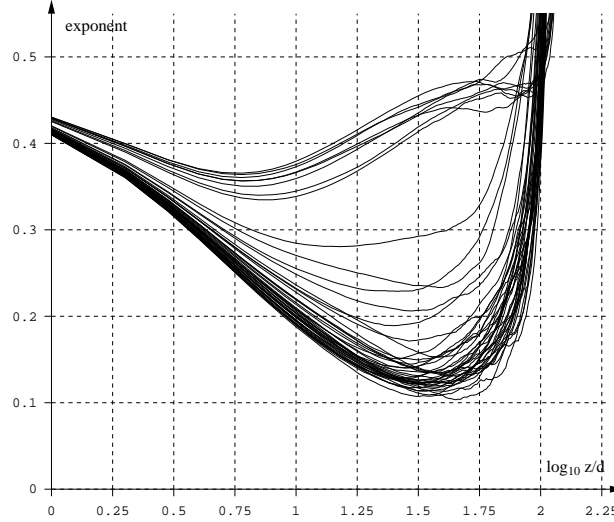


Figure 5.10: Dependence of the relative pancakes root mean square fluctuations exponent in a pile as function of distance  $\delta u(z)$  for various temperatures across the transition at  $b = 1$  Tesla with 100 layers. More precisely the vertical axis is  $\alpha \doteq \frac{\partial \ln \delta u(z)}{\partial \ln z} = \frac{z}{\delta u(z)} \frac{\partial}{\partial z} \delta u(z)$ . It is equal to  $\frac{1}{2}$  for a free vortex line. The divergence for large  $z$  is likely due to the open boundary effect. The upper group of lines are from simulations at higher temperatures and the lower group corresponds to lower temperatures, across the “entangling” melting transition.

toward high fields leads to an *entangled liquid* or *three-dimensional liquid* in which the in-plane order is lost because of the large wandering of the lines around each other [62]. This is supported by Figure 5.10 showing how the lines break free over a certain lengthscale after the entangling transition. Those two type of liquid are expected for our model in the continuous regime, for it is equivalent to the 2D Boson model (see Section 3.4.3). The transition at the highest field at which one observes a kink in  $\delta u(d)$ , on the other hand, is related to the discrete nature of our model. The value of  $z$  at which  $\delta u(z)$  has a kink at the transition indicates the correlation length of the pancake positions in a pile. Indeed the kink comes from the fact that the line starts wandering freely over that lengthscale in order to account for the in-plane position fluctuations. When the kink reaches  $z = d$ , the interlayer spacing, then two successive pancakes in a pile are fully decoupled for they can travel far

enough to break the hexagonal lattice <sup>2</sup>. The decoupling transition is further confirmed in a simulation with 100 layers as shown in Figure 5.11. We note that a simulation including a Monte Carlo move in which the way the pancakes are connected is changed (a reconnection move) would improve the analysis of this transition as it would allow  $\delta u(d)$  to really diverge.

Figure 5.12 shows that when the number of layers is increased, the transition at a given field changes from a non-entangling transition to an entangling one. As long as the transition is non-entangling, the transition temperature is proportional to the number of layers. On the other hand the transition temperature is no more sensitive to the number of layers within the entangling transition, as further confirmed by Figure 5.13 showing the phase diagram for different number of layers  $N$ . (Consider only the points for which  $n = 1$ , the meaning of  $n > 1$  will be explained in the next section).

Therefore the non-entangling transition is a finite size effect. In order to obtain a melting hopefully in qualitative agreement with a system of infinite size, we need to reach a number of layer sufficient in order to observe the entangling transition. The number of layers needed can be estimated by noting that if the inter-layer interaction was infinite (if the lines were totally stiff), then the system would be nothing more than the two-dimensional system studied in the previous section but with the interaction multiplied by the number of layers  $N$ . Therefore a system of  $N$  layers at temperature  $t$  and field  $b$  will certainly melt in a non-entangling fashion if  $t > N t_m^{2D}(b)$  where  $t_m^{2D}(b)$  is the transition temperature when  $N = 1$  at field  $b$  (Figure 5.2). This means that if we want to avoid this finite size effect we want to make sure that  $N$  is such that

$$N \gg \frac{t}{t_m^{2D}(b)} \quad (5.3)$$

The pertinence of this relation can be seen in Figure 5.13 in which the little dots represents  $(N t_m^{2D}(b), b)$  for  $N = 8$  and  $N = 100$ . Those points are seen to match closely the low-field 3D transition points for the corresponding system of  $N$  layers. In the high field region where the 3D transition temperatures gets smaller than what is predicted from 5.3, the melting

---

<sup>2</sup> At that point the vortex lines can be considered to have lost their existence since, were the simulation to allow pancakes to switch to the closest pile, the pancakes would wander independently inside a layer. The fact that this simulation does not allow reconnection is not a true limitation as all the possible pancake configurations *and* connection do exist if one does not keep track of the immaterial identity of the pancakes. A reconnection move would therefore only accelerate the dynamics.

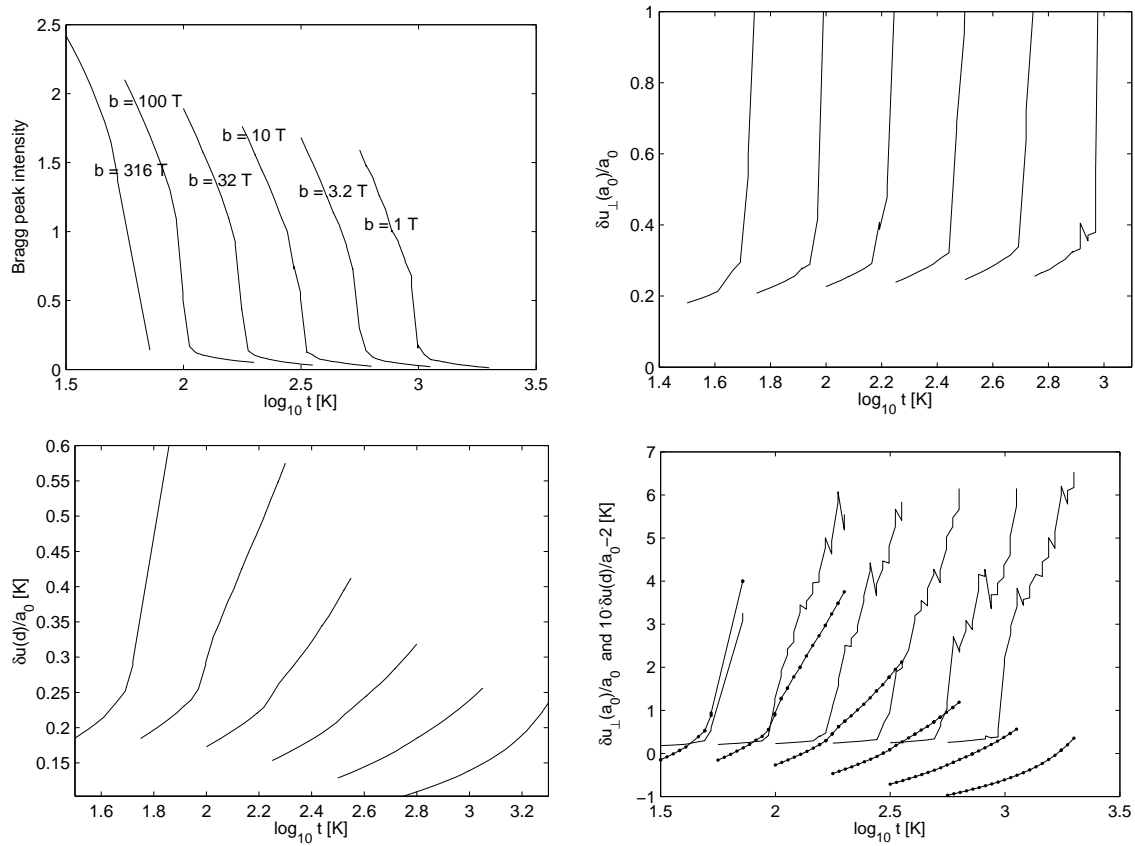


Figure 5.11: Series of observables versus temperature at several (high) fields. See the caption of Figure 5.9 for a definition of the symbols. The bottom-left graph represents the root mean square fluctuations between two neighbouring pancakes in a pile ( $\delta u(d)$ ) in a pile. At 30 Tesla we see a distinct kink which is barely noticeable at the lower fields (10 Tesla). This value of the field is consistent with continuum elastic theory which predicts the decoupling to happen at  $b \simeq 27$  Tesla (Equation 6.5 in Ref. [31]). The bottom-right graph compares  $\delta u(d)$  (scaled and shifted, with dots) to the fluctuations between neighbours inside plane (solid lines), it indicates that the decoupling of the layers accompanies the melting at high fields (though it may also happen in the liquid phase at lower fields). Also compare this decoupling field (between 32 and 10 Tesla) to the intersection between the green dashed line and the dotted line in the top graph of Figure 5.21.

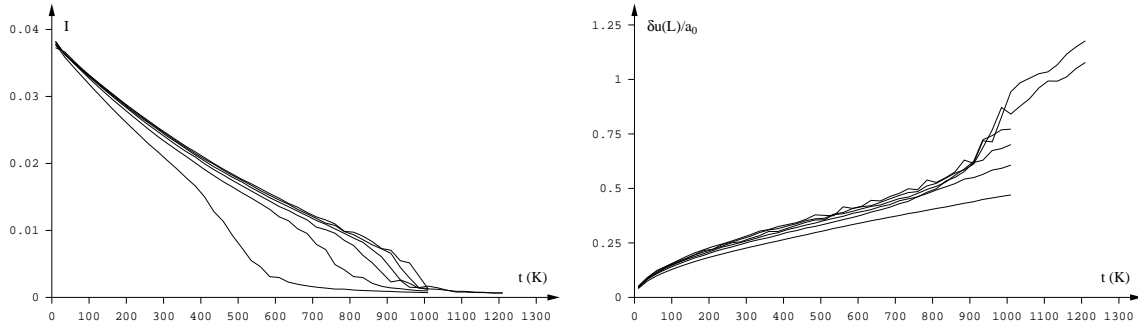


Figure 5.12: Dependence of the Bragg peak intensity and line wandering on the number of layers at  $b = 1$  Tesla, with 64 pancakes per layer.

points all gather on the solid line representing scaling 3.34. Furthermore, comparing to figures 5.9 and 5.14 show that this region of the melting which follows the law 3.34 is the entangling melting characterized by a kink in the line wandering  $\delta u(L)$ . Now let us explain what the  $n > 1$  means on Figure 5.14.

### 5.3.2 Layer decimation

Because the non-entangling melting transition temperature  $t_m^{2D}(b)$  (Figure 5.2) decays exponentially as a function of field at low fields, the number of layers needed to reach the three-dimensional entangling transition also grows exponentially according to formula 5.3. But we have seen in Section 3.4.1 that if the lines do not fluctuate too much (relation 3.17), one can substitute  $n$  layers with only a single one assuming the correct renormalization of the simulation's parameters. In practice we perform the transformation 3.28 in the simulation by modifying only  $\gamma$  and the unit of energy  $\epsilon_0$ :

$$\begin{aligned}\epsilon_0 &\rightarrow n\epsilon_0 \\ \gamma &\rightarrow n\gamma\end{aligned}$$

Figure 5.15 shows a test of this procedure for  $N = 80$  and  $n = 4$  at a field  $b = 1$  Tesla for the parameters used all along this section (YBCO with constant zero-temperature  $\lambda$ ).

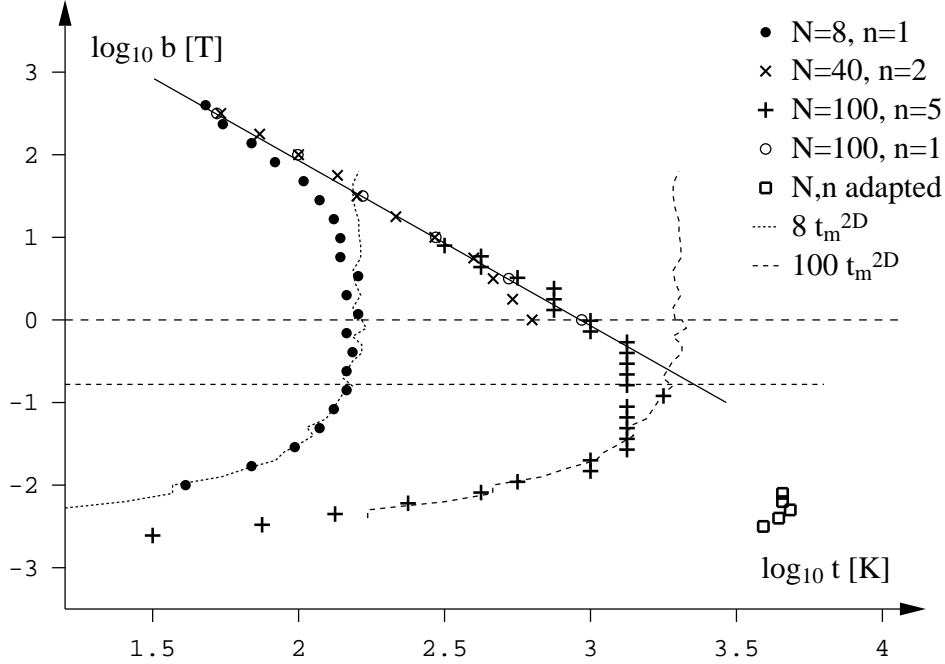


Figure 5.13: Transition temperature as function of field for various system size for YBCO  $T = 0$  parameters.  $N$  is the physical total number of layer of the system. The simulation uses only  $N/n$  layers with parameters appropriately rescaled (Section 5.3.2). The horizontal solid line shows the field value at which  $a_0 = \lambda$ . The inclined solid line is a fit of Equation 3.34. The two dashed lines represented the 2D melting transition temperatures respectively multiplied by 8 and 100. It shows where the 3D systems crossover from a 3D melting to a 2D melting and therefore deviates from the scaling relation 3.34. Those transition temperatures correspond to the point where the nearest-neighbour in-plane relative fluctuations  $\delta u_{\perp}(a_0)$  reach 45% of  $a_0$ , except for the points labelled “ $N=40, n=2$ ” where the threshold is fixed at 60%, and for the squares which correspond to the points where  $\psi_6$  falls to 0.1 (because of the bad quality of  $\delta u_{\perp}(a_0)$  for those data). The rather high values of the threshold for  $\delta u_{\perp}(a_0)$  have been chosen in order to avoid fluctuations due to the coexistence temperature region where the system jumps from the solid to the liquid phase with low probability. The squares are not positioned on the solid line because they are far in the exponential interaction regime for which the scaling 3.34 is no more valid (see Section 5.3.4 for details about those points).

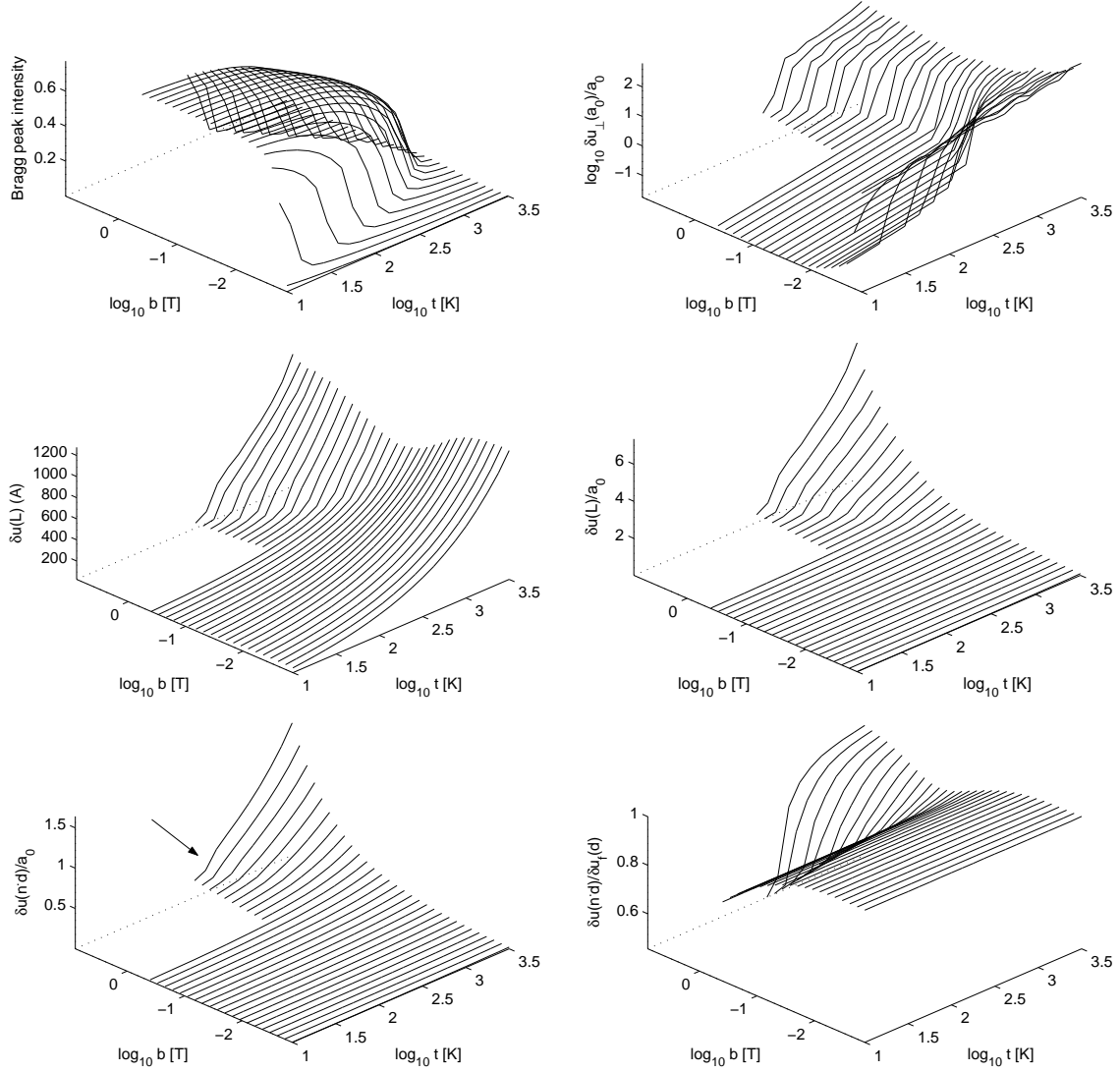


Figure 5.14: Various observables as function of  $b$  and  $t$  for a system of 36 pancakes per layers and 20 layers renormalized as 100 real layers. Notice the kink in the line wandering associated with the melting at high field. Also the kink in  $\delta u(nd)$  (arrow) at the highest field values is likely a manifestation of the discreteness of the system at the lengthscale  $z = nd$ , which is here artificial (because we neglect  $n - 1$  layers inbetween). It therefore hints at the inappropriateness of the approximation at those fields (Section 5.4).

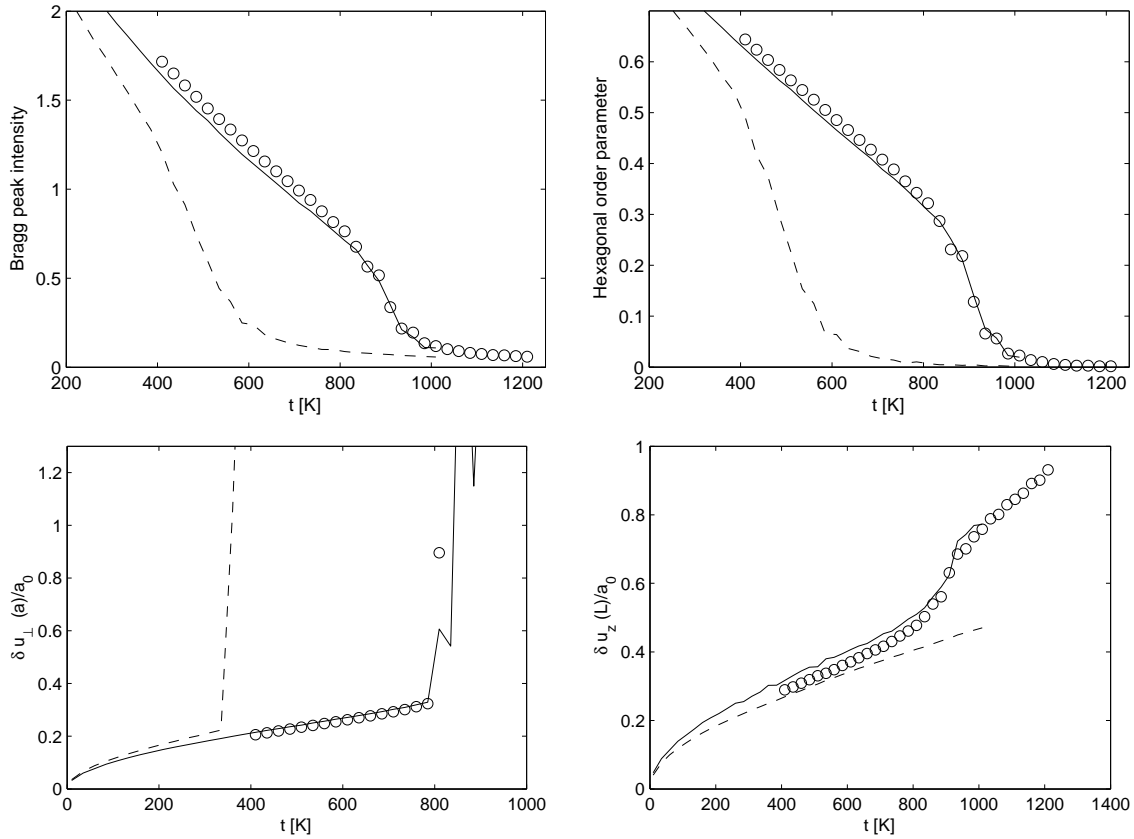


Figure 5.15: Comparison between a simulation done with 80 layers (solid line) and a simulation done with 20 layers with parameters renormalized with  $n = 4$ . Both simulations used 36 pancakes per layer and were done at  $b = 1$  (T). The bottom-left graph represents the relative root mean square displacement between two neighbouring pancakes in the same layer. The bottom-right graph represents the relative root mean square displacement between two pancakes at both extremity of the same pile (line wandering). The dashed line is from a simulation with 20 layers and no renormalization of the parameters.

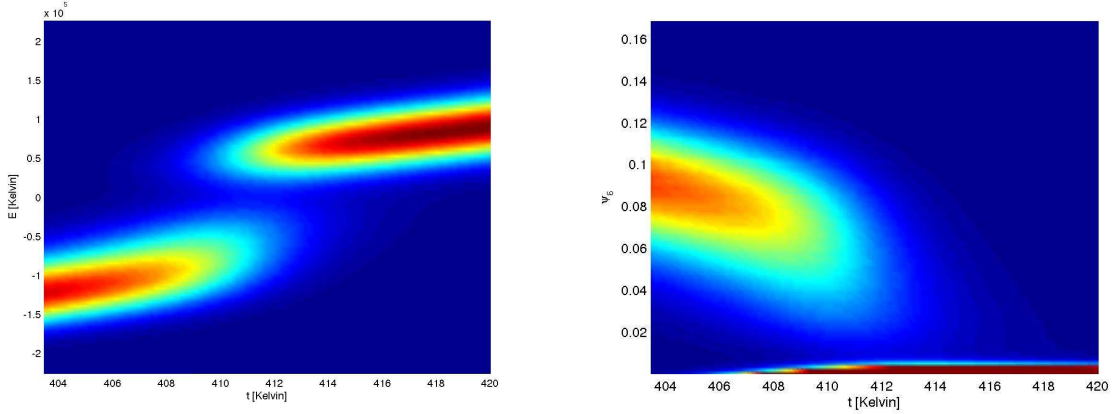


Figure 5.16: Energy (left) and  $|\psi_6|^2$  (right) histograms as function of temperatures around the transition for a system of 20 layers, 5 virtual layer ( $n = 5$ ) and 100 pancakes per layer at  $b = 5$  T (YBCO:  $B \sim 0.2$  T). The simulations have been run at 15 equally spaced temperatures in the shown range. Those graph have been calculated from the joint density of state as function of the energy and  $|\psi_6|^2$  observable extracted from those simulations using the multihistogram method. The fluctuations  $\delta u(nd)$  on Figure 5.18 shows that this physics is that of the decoupling transition rather than an entangling transition in the continuous regime (see text).

Figure 5.14) shows observables in the  $b$ - $t$  plane for a simulation of 100 physical layers with only 20 layers ( $N = 100, n = 5$ ). The transition points extracted from this simulation are the points labelled “ $N = 100, n = 5$ ” in figure (5.13. We can see that they closely match the points obtained with the simulation of 100 layers, as well as the non-entangling melting breakdown appropriate for 100 layers (dashed curve).

### 5.3.3 Order of the transition

Figure 5.16 shows the histograms of the energy and  $|\psi_6|^2$  order parameters as function of the temperature at  $b = 5$  (T) (YBCO:  $B \simeq 0.2$  T). This shows that the transition observed is very sharp and very likely first-order as further confirmed by the scaling behaviour of the specific heat and the  $\psi_6$  susceptibility shown in Figure 5.17. Nevertheless, even though at  $b = 5$  (T) the system is in the continuous regime (no associated kink in  $\delta u(d)$ ), those

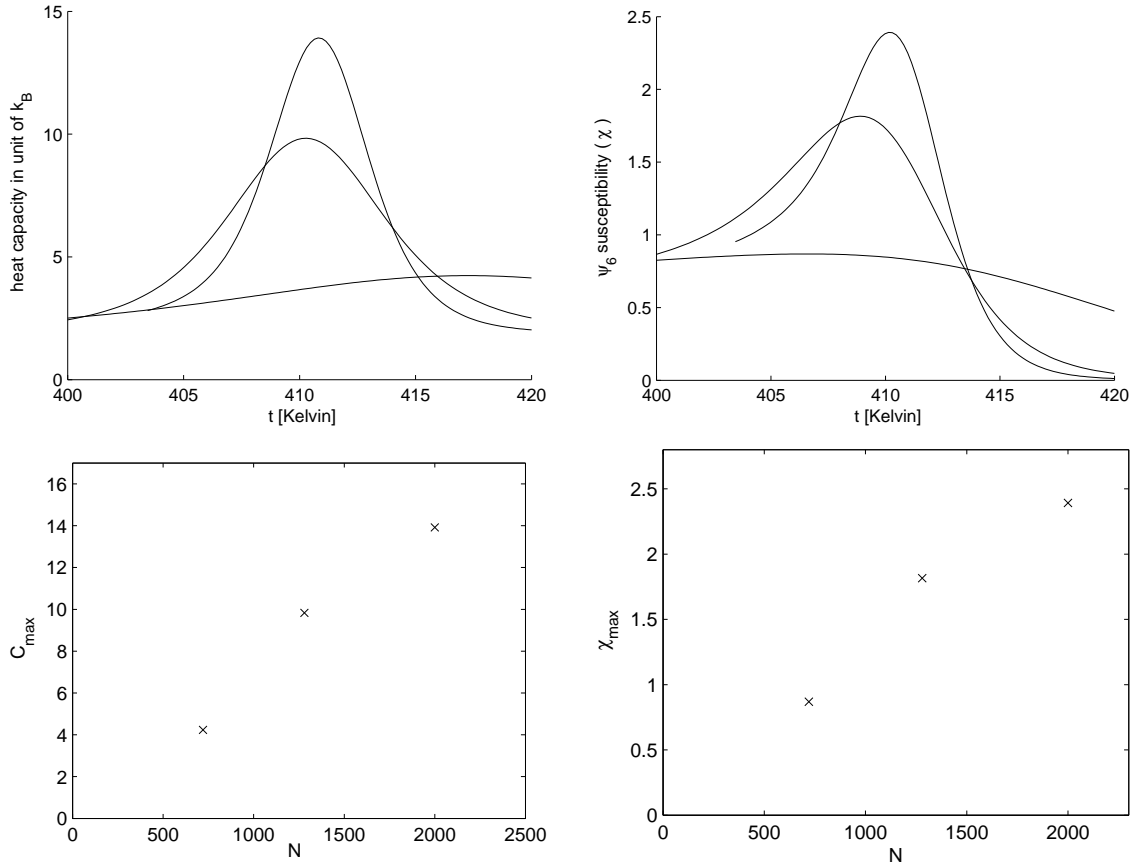


Figure 5.17: Heat capacity (left) and  $|\psi_6|^2$  susceptibility (right) for different system sizes at  $b = 5$  T (YBCO:  $B \sim 0.2$  T). The bottom graphs show the scaling of the respective peaks maxima. All three simulations have been done with a system of 20 layers, simulating a system of 100 layers ( $n = 5$  virtual layers). The number of pancakes per layer was respectively 36, 64 and 100.  $N$  is the total number of pancakes. The fluctuations  $\delta u(nd)$  on Figure 5.18 shows that this physics is that of the decoupling transition rather than an entangling transition in the continuous regime (see text).

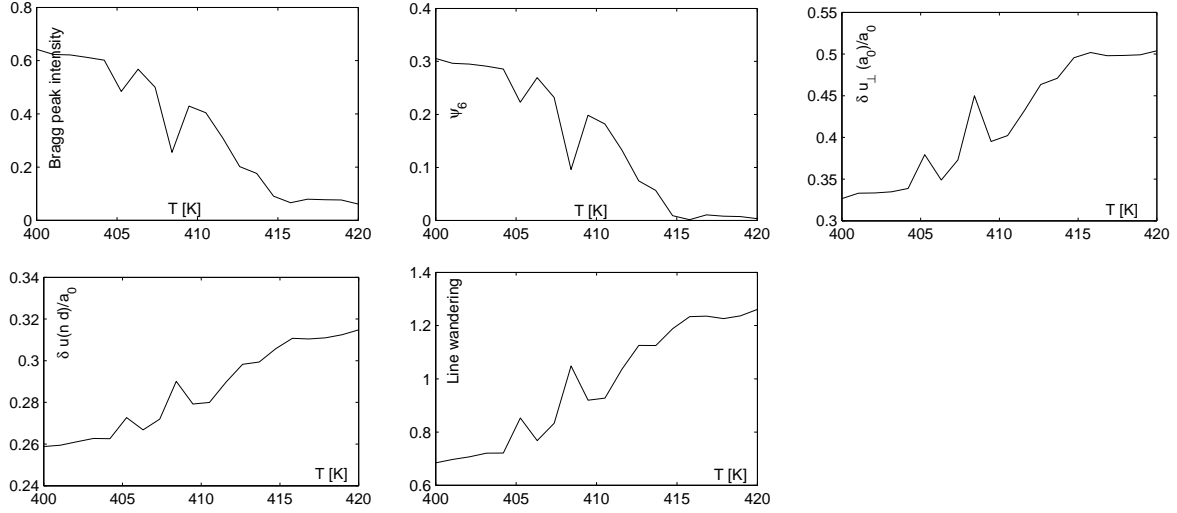


Figure 5.18: Various observables corresponding to the transition shown in figures (5.16) and (5.17), for the system with 64 pancakes per layer. The simulation was done on 20 layers renormalized as 100. The oscillations come from the poor dynamics at the transition, which was corrected by the multihistogram method in Figure 5.16 and (5.17) (but not in those pictures because we saved only the timeseries of energy and  $\psi_6$ ). The bottom-left graph represents the interlayer root-mean-square fluctuations between pancakes separated by a single simulated layer (representing 5 physical layers). The fluctuations in this particular graph indicate that  $n$  may have been set at a too high value, for this indicates that the position-position correlation length along a vortex becomes shorter than the distance over which we neglect fluctuations. This makes the transition studied here of the decoupling kind rather than of the entangling kind (see text).

simulation where done with a rather high number of virtual layers;  $n = 5$  (as understood a posteriori). The jump in  $\delta u(nd)$  at the transition (Figure 5.18) indicates that the transition is effectively of the same form as a high field transition where a jump in  $\delta u(d)$  is observed (compare to Figure 5.11). This shows that the artificial discreteness of the system caused by the relatively high number of virtual layers becomes important, hence invalidating this system as a good approximation of the full system. In short,  $n$  was set too high, causing the observed transition to be of the “decoupling type”. Therefore what we can conclude from those data is that the decoupling-melting transition is first order. In order to directly confirm the first-order nature of the entangling transition new simulations should be run with a smaller number of virtual layers.

### 5.3.4 Re-entrant melting

Analytical calculations based on the Lindemann criterion applied to a continuous elastic medium [40] predict a reentrant melting at low field in the infinite system. The reentrant melting temperature that we observed in Figure 5.13 for instance increase linearly with the number of layer and therefore may not qualitatively correspond to a property of a system with an infinite number of layers. Instead we would like to investigate the possibility of a reentrant melting with the total number of layers kept large enough (Equation 5.3) in order to avoid this temperature-dependant non-entangling melting.

There has been no simulation of this phenomenon, neither with the XY model nor the model of elastic flux lines. Reentrance has been observed in the 2d boson model [72][73] which is nearly identical to this one at low field, but the approximation used in this context are difficult to translate to the picture that we are using, and we do not know whether or not this reentrance is an artefact of the approximation used<sup>3</sup>.

---

<sup>3</sup>The problem of finding the thermodynamical average of an observable for the infinite system (along  $z$ ) translates in the boson language to finding the average of a corresponding quantum observable in the ground state of the 2d model. What has been done in Refs. [72] [73] is to find an approximate ground state wave-function by minimizing the energy in a particular ensemble of state, which is believed to capture the physics of the problem. In what follows we will see that we ran into trouble when trying to access the reentrant regime with our simulation because of the high number of layers that we would need to take into account. In the boson model this translates into a high time resolution, which is coded in the high-momentum components of the ground state wave-function. Therefore a cutoff in momentum space

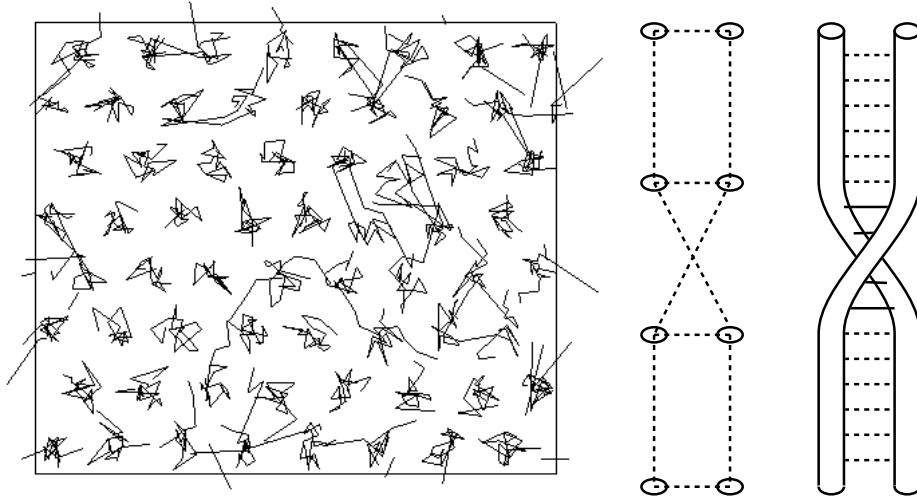


Figure 5.19: Left: simulation snapshot prior to the dubious reentrant melting. The lattice is globally ordered but at many places, lines swap positions on the lengthscale of one or a few layers. Such a state would cost more intralayer energy were the intermediate pancake to be reintroduced, as show on the right figure. Its existence shows the low-field breakdown of the layer decimation approximation. Right: two piles get swapped within a single simulated layer. This costs only little interlayer energy and no intra-layer energy at all. But if all the intermediate pancakes were to be added (rightmost figure), they would have to come very close at a high cost of intra-layer energy (solid horizontal lines).

We encountered the problem that the condition 3.17 does not allow for the number of virtual layers  $n$  to be big enough to compensate for the rapid growth of the total number of layers due to the exponential decay of  $t_m^{2D}$  (through Equation 5.3). Therefore the number of layers to simulate still grows too fast when the field decreases. If the condition 3.17 is not satisfied then we observe a reentrant melting of a different type, which seems associated with the proliferation of a defect in which two parallel vortex lines get swapped within one single simulated layer (Figure 5.19).

Such a state would be energetically disfavoured if the neglected (virtual) intermediate layers were to be added (see Figure 5.19).

---

might have the same effect as an excessive value of  $n$  in our approximation.

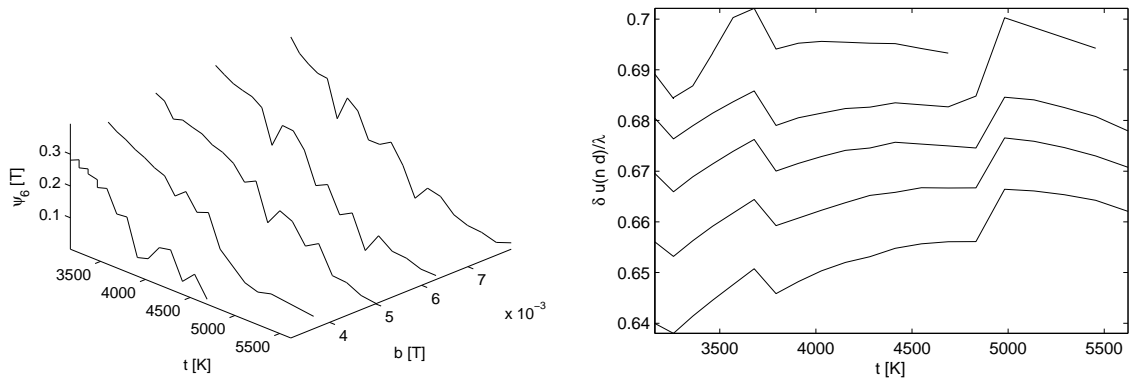


Figure 5.20: Data corresponding to the squares in Figure 5.13. Those data are of bad quality because of the large system sizes involved (up to 450 layers). Nevertheless we clearly see a drop of the  $\psi_6$  order parameter down to nearly 0 (remember that the maximum is 1). The graph on the right shows the root mean square fluctuations between neighbouring pancakes in a pile  $\delta u(nd)$  relative to  $\lambda$ . The strongest fluctuations correspond to the data at the lowest field. The unphysical discontinuities are due to the increase in the number of virtual layers  $n$  as the field decreases and temperature increases. The curves look alike because  $n$  was set to the same values as function of temperature for all fields. This shows that the fluctuations are not much smaller than  $\lambda$  and therefore that condition 3.17 is not secured for the lowest fields.

The squares on Figure 5.13) have been obtained from long simulations with the condition 3.17 just barely satisfied (figure (5.20)). It would seem to indicate that the melting temperature starts decreasing when at around  $b \sim 3$  mT and  $t \sim 4500$  K, which corresponds to  $B \sim 0.74 \mu\text{T}$  and  $T \sim 0.9986T_c$  for YBCO. Nevertheless, for the lowest fields the fluctuations  $\delta u(d)$  which should be much smaller than  $\lambda$  are in fact around 70% of  $\lambda$ . Therefore we have no conclusive evidence for the existence of a reentrant melting but we have evidence that it does not happen at least relatively far in the logarithmic regime (with a field 1.5 orders of magnitude smaller than the field at which  $a_0 \simeq \lambda$ ). This observation can be extended to models with different parameters and notably a T-dependant  $\lambda$  only if they are within the regime where the continuous vortex line approximation holds (see Section 3.4.2). But for any parameters the model will be in the continuous regime at sufficiently low field and temperature, in which this observation is always of relevance. Indeed the continuous regime is characterized by expression 3.29 which can always be satisfied either by decreasing  $\delta u_1$  through the temperature, or increasing  $a_0$  by decreasing the field  $B \sim 1/a_0^2$ .

## 5.4 On the number of layers

Before proceeding to simulations with a temperature-dependant penetration depth  $\lambda$ , we want to establish an algorithm for deciding what are safe values for the number of layers  $N$  and for the proportion of layers that we can neglect  $n$ . In order to optimize simulation time we want  $N$  as small as possible and  $n$  as big as possible. Choosing  $N$  is rather easy; we already made the observation that if  $N$  (Equation 5.3) is too small then the system will melt in a non-entangling fashion. We assume that this is the only relevant phenomenon for choosing  $N$ . From experience it is safe to choose  $N$  at least three times above the limit expressed in 5.3. This can be checked by observing how far from  $Nt_m^{2D}$  the melting curve starts deviating from the correct 3D melting line in Figure 5.13. For instance for the 8 layers system we see that the deviation from the solid line occurs less than half a decade away from  $8t_m^{2D}$  and  $10^{0.5} \simeq 3$ .

In choosing  $n$  we want to make sure that

1. the relation 3.17:  $\delta u_n \ll \min(\lambda, a_0)$  is safely satisfied,

2. the system does not enter into the inter-layer linear interaction regime built in the Hamiltonian (Equation 3.3).

We do not a priori know the quantity  $\delta u(nd)$  (also named  $\delta u_n$  in Equation 3.17). But we know an upper bound; the free line fluctuation  $\delta u_f(nd)$  defined in Equation 5.1. Also the results shown in the bottom-right graph of Figure 5.9) or (5.14 indicate that  $\delta u(nd)$  does not differ from  $\delta u_f(nd)$  by more than a factor two near a transition, so that this upper bound is not unreasonably inefficient. Therefore point one above consists in making sure that  $n$  is chosen so that  $\delta u_f(nd) = \delta u_f(d)\sqrt{n}$  is small enough compared to both  $\lambda$  and  $a_0$ . The second point is satisfied by mainting  $\delta u_f(d)$  small enough compared  $2\gamma d$ .

The actual algorithm used goes as follow, for a given field  $B$  and temperature  $T$ , and security margins  $s_1$ ,  $s_2$ ,  $s_3$  and  $s_4$ .

1. Choose the number of layers of the simulation box

$$N = s_1 \frac{T}{T_m^{2D}(B, T)} \quad (5.4)$$

where  $T_m^{2D}(B, T)$  is the temperature at which a system with the same Hamiltonian but the interlayer interactions turned off would melt. It is computed from the interpolating curve  $t_m^{2D}(b)$  on Figure 5.2. Section 5.2.1 explains how  $t_m^{2D}(b)$  can be used to obtained  $T_m^{2D}(B, T)$ .

2. Check that  $\delta u_f(d) < 2\gamma d/s_2$ . If this is not the case then choose  $n = 1$  and stop the algorithm here. The layer decimation would be wrong as it applies only to harmonic interactions. (The inter-layer interaction (Equation 3.3) was assumed to be harmonic in the derivation of Section 3.4.1).

3. Check that

$$\delta u_f(d) < a_0/s_3. \quad (5.5)$$

If this is not the case then choose  $n = 1$  and stop the algorithm here. This means that we entered the decoupling regime and we have to account for every layers.

4. If  $\lambda > a_0$  then we are in the logarithmic regime. Choose

$$n = \frac{a_0^2}{s_3^2 \delta u_f^2(d)}$$

but not less than  $n = 1$ .

5. If  $\lambda < a_0$  then we are in the exponential regime. Choose

$$n = \frac{\lambda^2}{s_4^2 \delta u_f^2(d)}$$

but not less than  $n = 1$ .

6. In any case, we don't want the resulting actual number of simulated layers  $N/n$  to be ridiculously small. If it is smaller than a given value  $nl_{\min}$  then we choose  $n = \max(1, N/nl_{\min})$ .

We typically used  $s_1 = 3$ ,  $s_2 = 1.2$ ,  $s_3 = s_4 = 4$  which seemed to be sufficient in most cases.

Figure 5.21 shows the different quantities used for a target  $N/n = 100$  layers and for parameters adapted to YBCO and BSCCO.  $N/n$  is the actual number of layers simulated and therefore defines what is numerically feasible. The white region can be handled with  $N/n = 100$  by adjusting  $n$ . The light gray region requires  $N/n > 100$  and the dark gray region requires  $n = 1$ .

## 5.5 Melting of the full clean system

Figure 5.22) shows a comparison between the simulation's melting temperature (extracted from data shown in Figure 5.24) and various experimental results for the melting temperature of the flux lattice in a YBCO crystal. The visible part of the phase diagram is mostly in the logarithmic regime; as shown by the fact that all the simulation points fall on the solid line which follows the simple quadratic law expressed in Equation 3.34, transformed according to the experimental T-dependance of  $\lambda$  as allowed in the logarithmic regime (see Section 3.4.4. The shift with respect to experiments at high field may be linked to disorder effect given that the glass transition has been observed at  $B \simeq 10$  Tesla [29][47].

Figure 5.23 shows how sensitive the simulation's results are on  $\lambda(T)$ . We see that the two-fluid model for  $\lambda(T)$  [5], often used to parameterize the BCS model, is able to make our

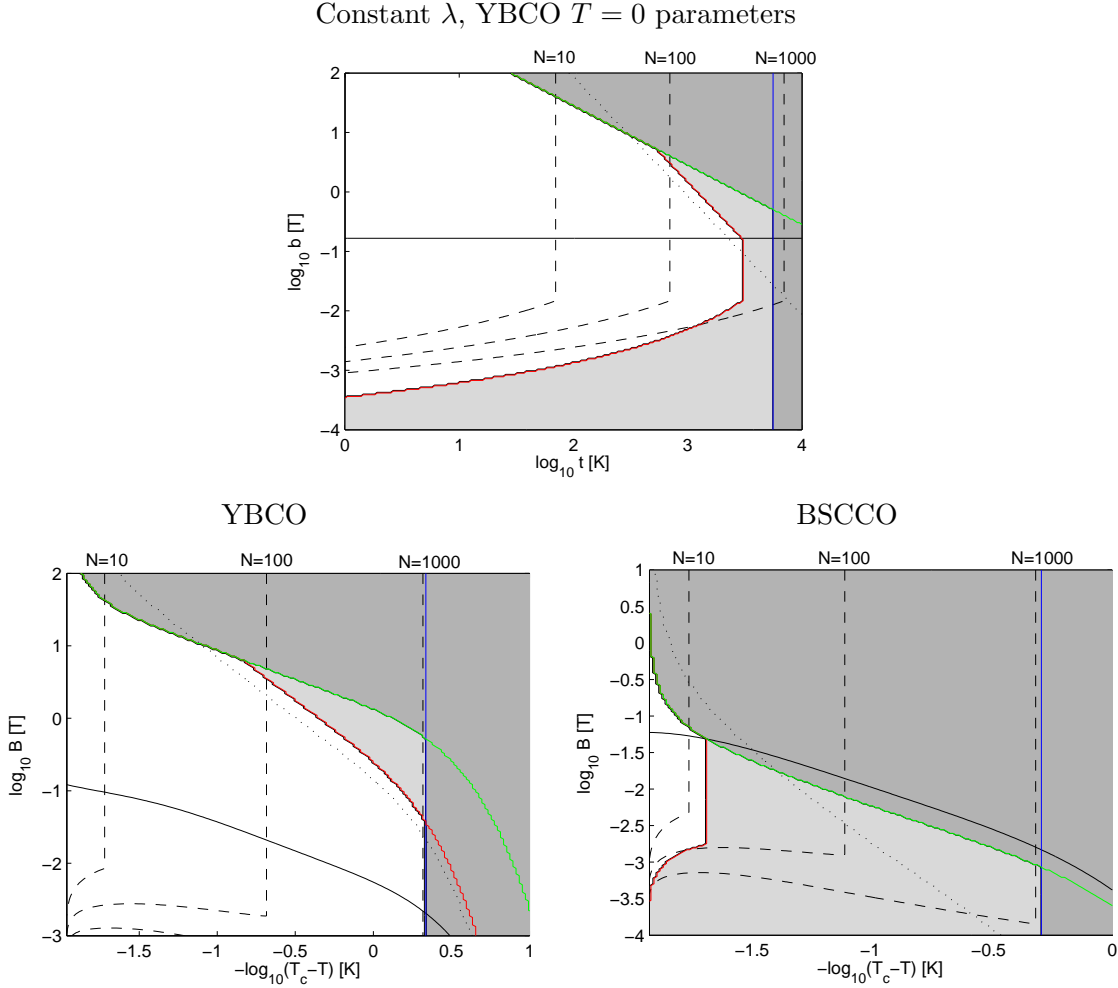


Figure 5.21: Simulation validity regimes for constant  $\lambda$  (top) with  $\gamma = 7.5$ ,  $\lambda(0) = 1200\text{\AA}$ , YBCO (bottom-left) ( $\gamma = 7.5$ ,  $\lambda(0) = 1400\text{\AA}$  and  $\lambda(T)$  according to Figure 3.2) and BSCCO (bottom-right) ( $\gamma = 140$ ,  $\lambda(0) = 2000\text{\AA}$  [34] and  $\lambda(T)$  according to Figure 3.2). The solid black line shows the points at which  $a_0 = \lambda$ . The black dotted line is the melting transition for the continuous line Hamiltonian in the logarithmic regime (Equation 3.34). It should be correct below the green line and above the solid black line. The dashed lines indicate the total number of layer  $N$  required by Equation 5.4 with margin  $s_1 = 4$ . On the right hand side of the red line, condition 3.17 requires  $N/n > 100$  (with margin  $s_3 = 3$  and  $s_4 = 4$ , see text), making simulations numerically difficult. The blue line indicates where the intra-layer interaction becomes linear so that one is forced to use  $n = 1$ . The green line corresponds to equality in Equation 5.5, it marks the limit to the decoupling regime at high field.

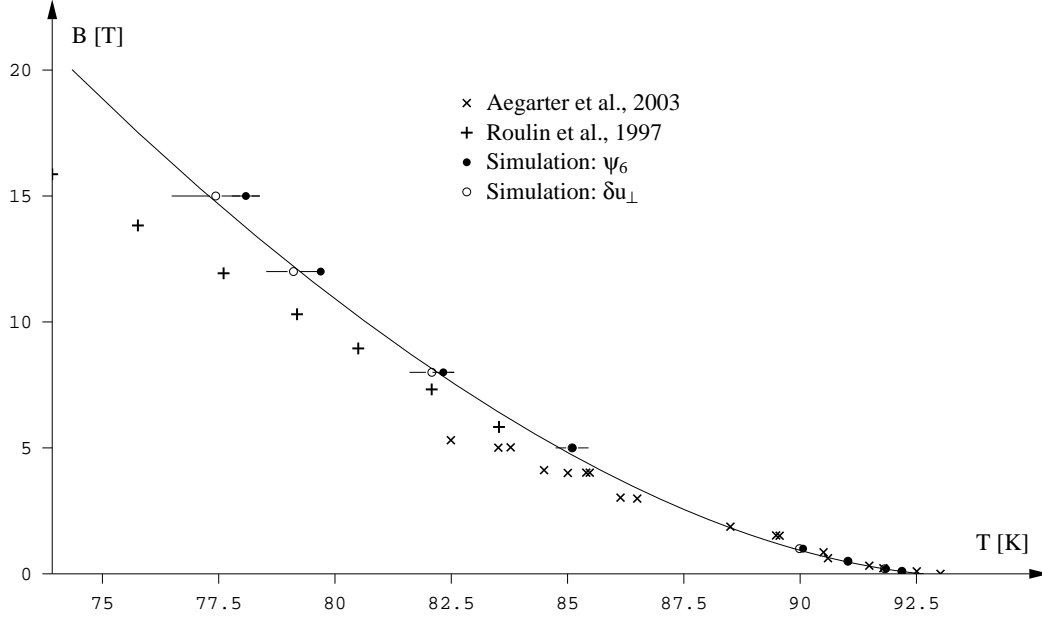


Figure 5.22: The melting temperature as function of external field for  $\text{YBa}_2\text{Cu}_3\text{O}_{6+\delta}$ . The solid line is the scaling 3.34 fitted to the constant  $\lambda$  transition (Figure 5.13) and transformed according to equations (3.32) and (3.33) with the experimental  $\lambda(T)/\lambda(0)$  shown in Figure 3.2, for various values of  $\lambda(0)$ . The simulations (white and black circles) were performed with the same temperature-dependent penetration depth  $\lambda(T)$  with 64 pancakes per layers and number of layers adapted according to the analysis in Section 5.4, with margins  $s_1 = 3$ ,  $s_2 = 1.2$ ,  $s_3 = s_4 = 4$ . The white circles with their uncertainty bars show the region over which  $\delta u_\perp$  raises from  $0.35a_0$  to  $0.5a_0$ . The filled black circles show the region over which  $\psi_6$  falls from 0.2 to 0.1. The straight crosses were obtained from Ref. [74] for the  $\delta = 0.96$  sample which were measured from the position of a heat capacity peak. The oblique crosses are from Ref. [21] from three different methods:  $\mu\text{SR}$ , SANS (neutron diffraction) and VSM (magnetization measurements). The parameters used were  $\lambda = 1400 \text{ \AA}$ ,  $\gamma = 7.5$  and  $T_c = 93 \text{ K}$ . The experimental points from heat capacity measurements [74] have been uniformly translated to accommodate for a different zero-field transition temperature  $T_c$  (91 K instead of 93 K), as this is how Roulin presented his results. A uniform scaling instead would shift the points by a maximum of 0.4 Kelvin which corresponds to the width of one of the crosses on this graph.

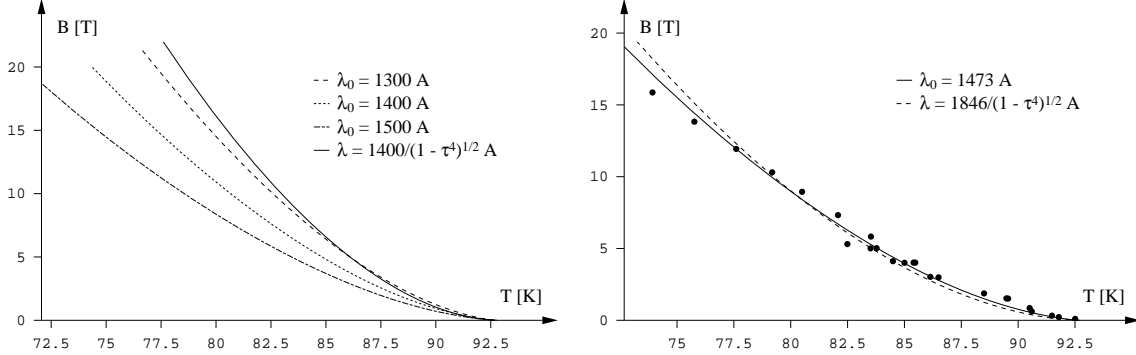


Figure 5.23: The left graph shows the dependence of the melting temperature on  $\lambda(T = 0)$  for YBCO. Also shown is a curve for  $\lambda(T)$  computed according to the “two-fluids” model [5];  $\lambda(t) = \lambda(0)/\sqrt{1 - \tau^4}$  where  $\tau \doteq T/T_c$ . The other curves make use of the Experimental data from Hardy *et al.* (see Figure 3.2). The right graph shows a fit of  $\lambda(0)$  to the experimental transition temperatures (same as on Figure 5.22) for both models of  $\lambda(T)/\lambda(0)$ . All the curves are made using the logarithmic regime assumption of Section 3.4.5 and fitted to the simulation data at constant  $\lambda$ .

simulation fit the experimental data but for a value of  $\lambda(0) = 1850 \text{ \AA}$  significantly higher than most estimations ( $1200 - 1400 \text{ \AA}$ ).

Figure 5.24 shows the evolution of various observables across the transition. We see that the Lindemann number; the value of the root-mean-square position fluctuations of the pancakes just before the melting, is around 40% which is higher than usually assumed (15%-30%). This is likely due to the fact that vortex lines are extended objects, which allows the structure to be stable despite large local fluctuations.

Due to the large anisotropy parameter  $\gamma$  of BSCCO the physics of the flux line lattice is quite different from YBCO, as can be seen on Figures 5.21 and 5.25. The first-order transition observed by Zeldov *et al.* [34] is correctly fitted by the physics of non-interacting lines in our model but can in no way be fitted by the continuous line scaling law 3.34. This indicates that the experimentally observed transition is independent of the in-plane interaction 3.1 and therefore unlikely related to a melting of the vortex lattice, which confirms the analysis of Zeldov *et al.* [34] who conclude that what they observe is most likely a decoupling transition between a vortex liquid and a pancake liquid.

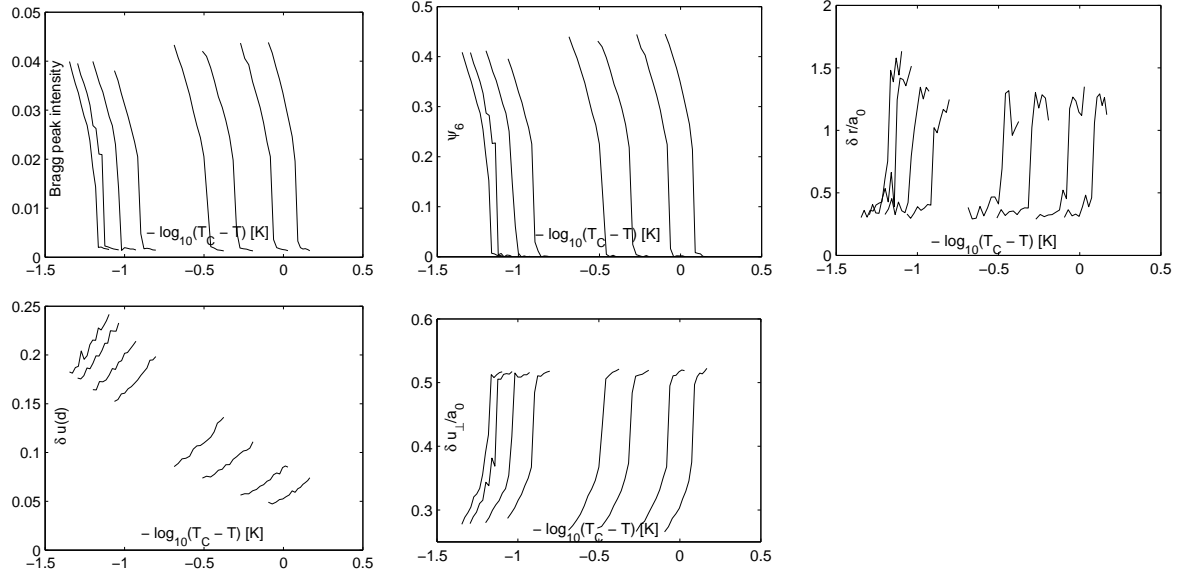


Figure 5.24: Various observables as function of temperature for various fields. This is the simulation data used to produce Figure 5.22. The top-right graph represents the root mean square pancakes displacements relative to the average pancake spacing  $a_0$ . It indicates that the Lindemann ratio, the maximum value of  $\delta r/a_0$  before it diverges, is around 40% which is much higher than the two-dimensional value of 15% (Figure 5.3). This suggests that due to their extended nature the vortices can locally fluctuate a lot without breaking the global order. The four lowermost curve on the  $\delta u(d)$  diagram were obtained with various values of  $n$  (the number of layer neglected according to the scheme described in sections 3.4.1 and 5.3.2). For those points the values of  $\delta u(d)$  reported are defined through  $\delta u(nd) = \sqrt{n} \delta u(d)$ .

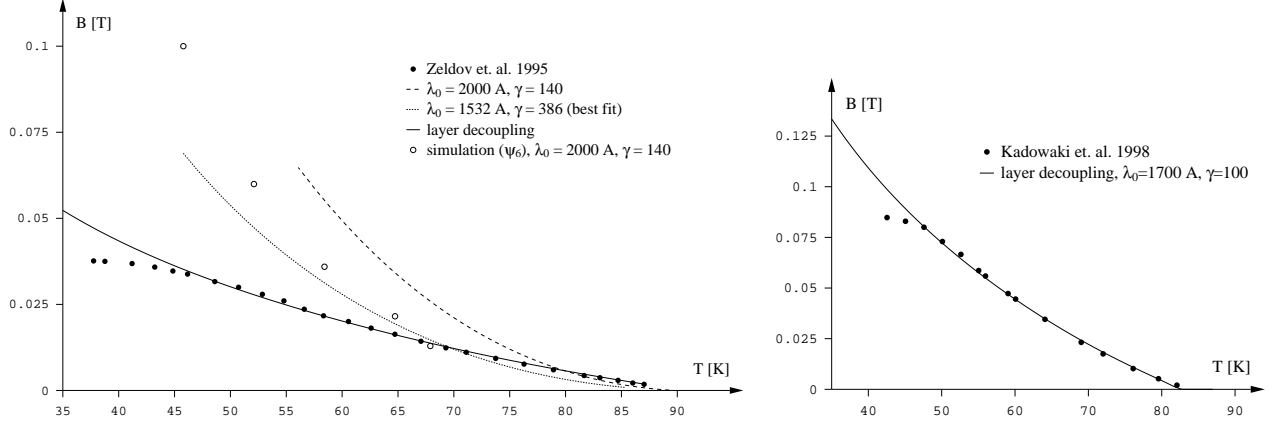


Figure 5.25: Phase diagram for  $\text{Bi}_2\text{Sr}_2\text{CaCu}_2\text{O}_{8+y}$  (BSCCO). Left: The filled circles are from experimental measurements of the magnetization jump by Zeldov *et al.* [34]. The solid line represents the points at which the RMS fluctuations between neighbouring pancakes in a non-interacting line reaches a fraction  $f$  (here fitted to  $f = 1/4.2$ ) of the average in-plane distance between vortices:  $\delta u_f(d) = fa_0$ , using  $\gamma = 140$  and  $d = 15\text{\AA}$  [34]. We note that the solid line is almost exactly the green line on Figure 5.21. The dashed lines are the continuous line  $\lambda$  melting curve following 3.34 and transformed according to the specified parameters and  $\lambda(T)/\lambda(0)$  as in Figure 3.2 for BSCCO. The line labeled “best fit” is the closest the curve can get to the experimental points by tuning  $\gamma$  and  $\lambda(0)$ . The empty circles are from simulations. They correspond to  $\psi_6$  dropping below 0.1, plus or minus one temperature step. The constant shift away from the solid line may be due to an insufficient number of layers. Right: same analysis for data from Kadowaki *et al.* [35]. The specific values of  $\lambda(0)$  and  $\gamma$  for the solid line have been found to fit the curve.

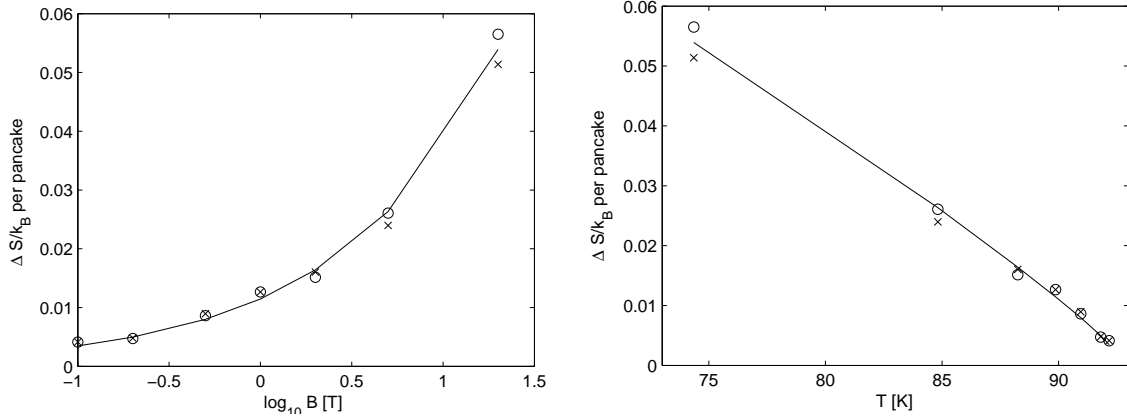


Figure 5.26: Entropy jump in YBCO as function of the average magnetic field (top-left) and transition temperature (top-right) and energy jump (latent heat) (bottom-left), obtained from the simulation. The circles are obtained by integrating  $C_V/T$  under the heat capacity peak. The crosses are extracted from the jump in energy (see Figures 5.27 and 5.28). The solid lines are a fit to Equation 5.10.

For BSCCO, the simulation's melting roughly follows the prediction from the scaling law and therefore cannot describe the experiments. Therefore the physics involved in this transition is different from the melting transition subject of this work. We cannot rule out that our model may undergo a decoupling transition in the liquid phase, though we never observed it. But this would at least requires that the transition happens within the liquid phase of our model, which it does not with reasonable parameters for BSCCO ( $\lambda_0 \simeq 1500 - 200$  and  $\gamma \simeq 50 - 250$ ). Instead it is very likely that the assumptions used to derive the interaction 3.1 (namely that the interactions between pancakes in different layers can be eliminated by assuming a standard contribution to the same-layer interaction) is not valid anymore for the strongly anisotropic BSCCO. This assumption may therefore artificially increase the rigidity of the system, causing it to be a solid where it should in fact be a liquid, and hiding the physics responsible for the experimentally observed transition.

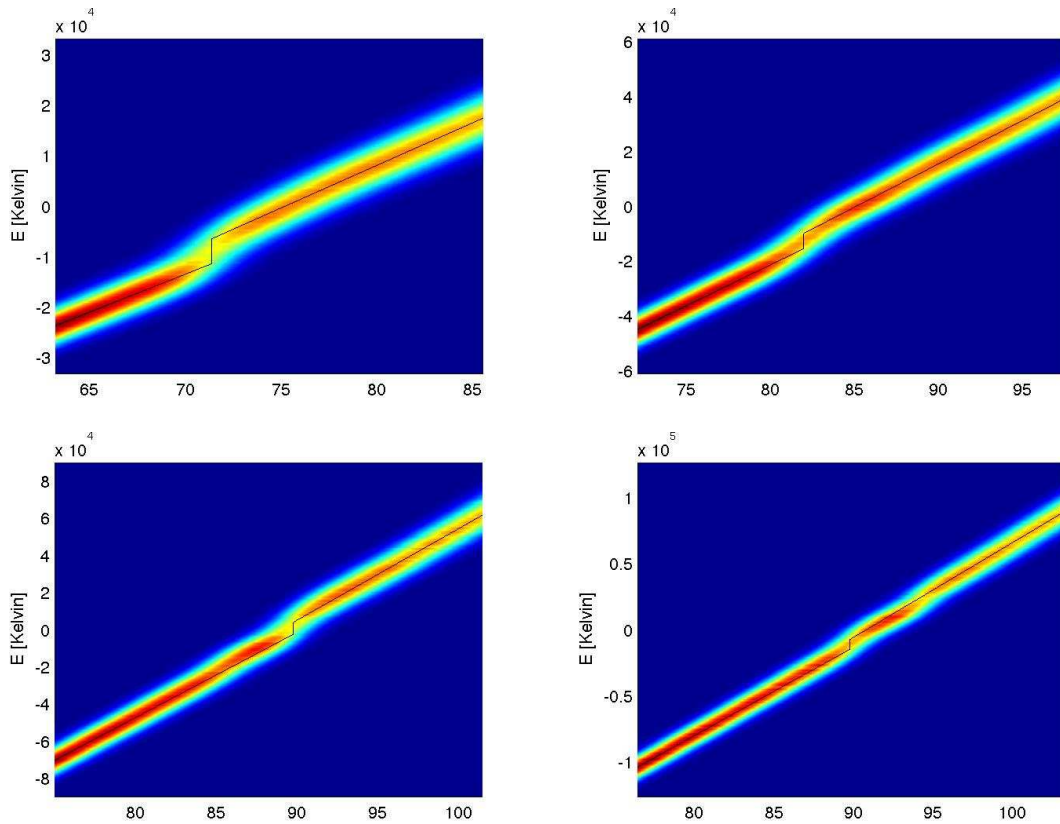


Figure 5.27: Energy histograms respectively for  $B = 20, 5, 2$  and  $1$  Tesla (continued on Figure 5.28). The black line shows how the energy jump was calculated for the results shown in Figure 5.26.

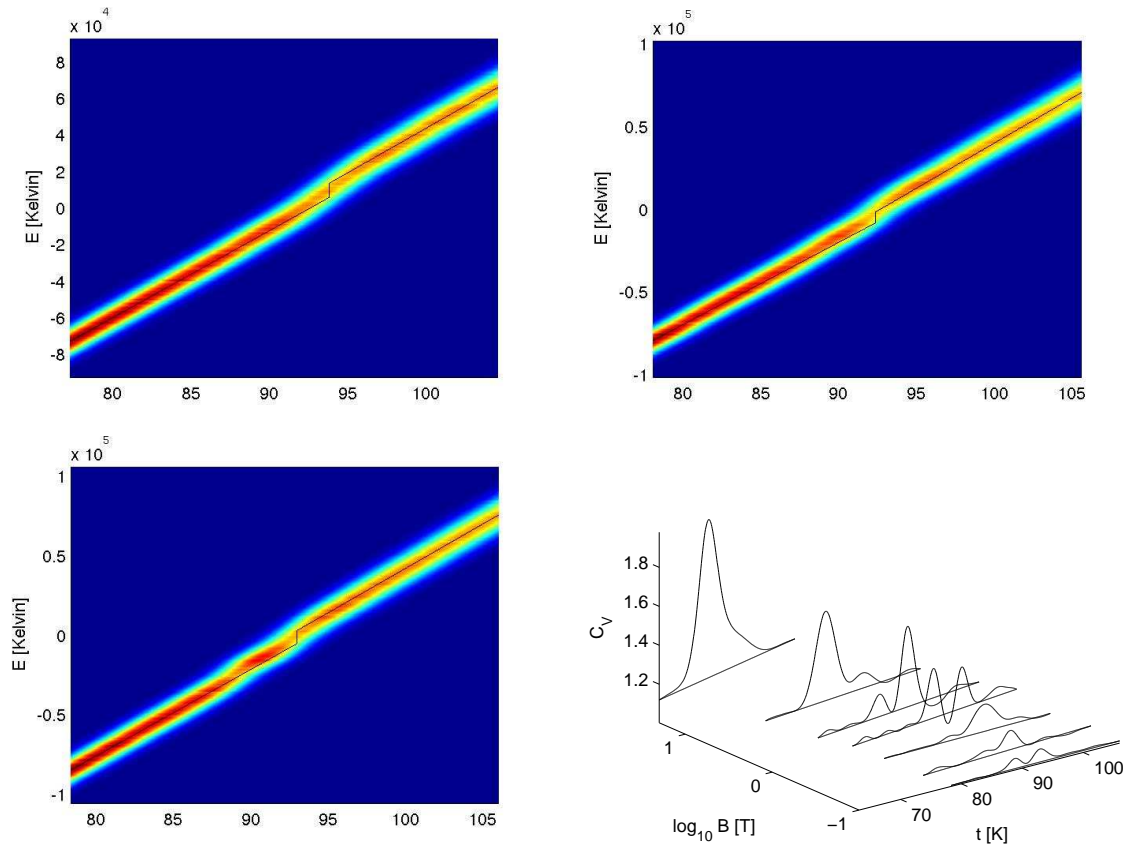


Figure 5.28: Energy histograms for fields  $B = 0.5$ ,  $0.2$  and  $0.1$  Tesla (See Figure 5.27). The bottom-left graph represents the heat capacity peak for each field as function of pseudo-temperature  $t$  (equal to the real temperature only at the transition, see text). The three lowest field series were obtained with respectively  $n = 2$ ,  $3$  and  $4$  virtual layers (Section 3.4.1). The heat capacity was computed accounting for the virtual layers according to Equation 3.22.

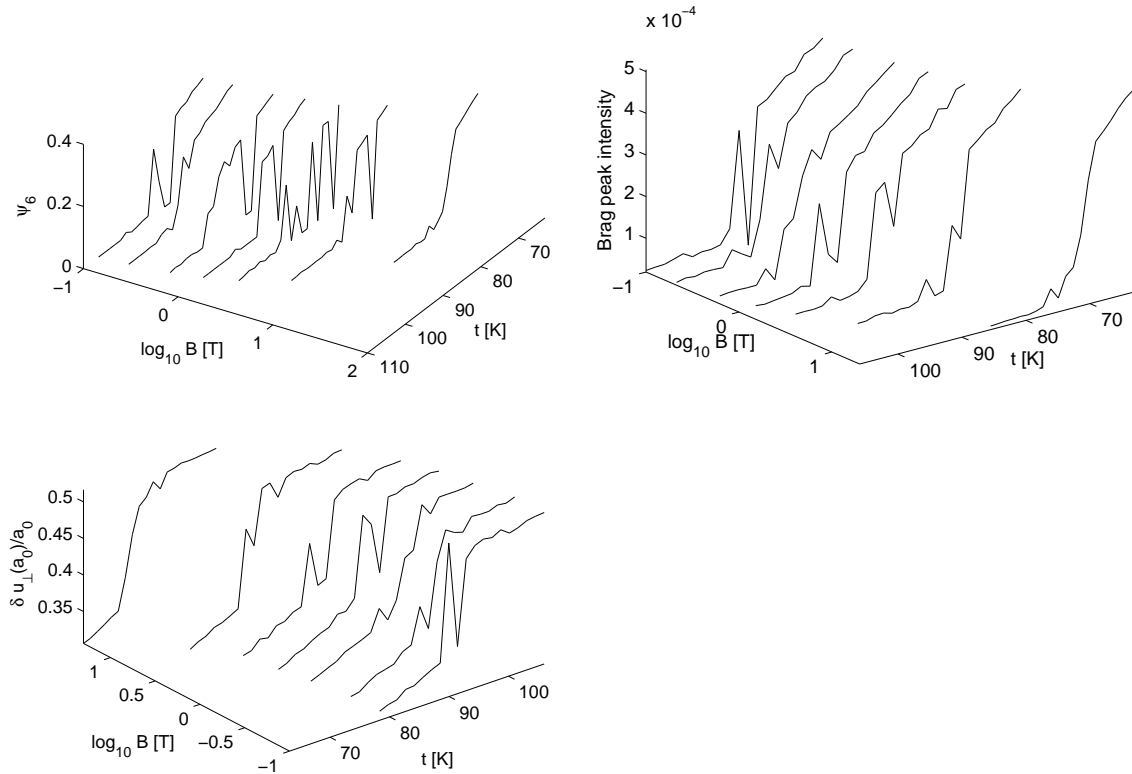


Figure 5.29: Observables corresponding to the data used to produce  $\Delta S$  (Figure 5.26). Note that the bottom graph is rotated of 180 degrees around the vertical axis compared to the two other figures, for graphical clarity. Each line (temperature series) was obtained with different value of  $\lambda$ , constant for all point of the series, and set to the value of  $\lambda$  at the melting temperature for that field according to Hardy's data (Figure 3.2).

### 5.5.1 Entropy jump

We used the simulation to compute the entropy jump at the melting transition for YBCO (Figure 5.26). The jump was measured by two different methods (Figures 5.27 and 5.28). The first one consists in directly measuring the energy jump  $\Delta E$  at the transition. Given that the free energy must be constant across the transition we have

$$\Delta F = \Delta E - T_m \Delta S = 0$$

then  $\Delta S = \Delta E/T_m$ . The second method uses the heat capacity

$$C = \frac{\partial E}{\partial T}.$$

At equilibrium we always have  $dF = dE - TdS = 0$ , therefore

$$\frac{\partial S}{\partial T} = \frac{1}{T} \frac{\partial E}{\partial T} = \frac{C}{T}.$$

If one identifies a heat-capacity peak on a generally smooth background and suspect that the peak results from a first-order transition, then integrating  $C/T$  *under* the peak—with the background subtracted—yields the associated change of entropy.

We chose to make the simulation with a value of  $\lambda$  constant over a temperature series, in order to keep a constant Hamiltonian. This allows us to directly use the histogram method, and to avoid the thermodynamical subtleties involved with a temperature-dependent “Hamiltonian”.

The connection to the real system is still maintained by setting  $\lambda$  for each time series to its value at the melting transition:  $\lambda(T_m)$ , where  $T_m$  is given by the solid curve on Figure 5.22.

Figures 5.27 and 5.28 show the resulting energy histograms. Figure 5.29 shows various observables for the data used to obtain the entropy jump. And Figure 5.26 shows the values obtained for  $\Delta S$  as function of field and temperature.

Let us try to explain the behaviour of  $\Delta S$  as function of the average magnetic field  $B$ . When the field decreases, the average spacing  $a_0$  between vortex lines increases and the interaction energy 3.3 between neighbouring pancakes in a pile becomes larger for a given displacement *relative* to  $a_0$ . This means that the vortex lines become more rigid.

But the melting happens when the vortex lines can fluctuate enough to become entangled with each other (that is over a distance  $a_0$  at least). Because of the increasing rigidity of the lines, those fluctuations happen on an increasing lengthscale  $\zeta$ , corresponding to the position correlation length along  $z$ . The entropy freed at the melting is related to the motion of vortex segments correlated over the distance  $\zeta$ . Therefore the jump in entropy *per pancake* must decrease as

$$\Delta S \sim \frac{1}{\zeta}. \quad (5.6)$$

The correlation length  $\zeta$  can be evaluated through

$$\frac{\zeta}{d} \sim \frac{T_m}{T_m^{2D}} \quad (5.7)$$

where  $T_m^{2D}$ , the 2D melting temperature that we encountered before, is the energy that would be needed to melt the system if the interlayer interaction was to be turned off. Indeed, melting the system requires the relative displacement of line segment of length  $\zeta$ , or piles of  $\zeta/d$  pancakes, which interact together according to  $\zeta/d$  times the term 3.1 which govern 2D melting. This analysis is also justified by the observation in Section 5.3 that a system of finite size  $\zeta$  melts precisely at  $T_m = \frac{\zeta}{d} T_m^{2D}$ . Here we assume that this relation holds when the number of layer is sufficient for the system to melt into an entangled liquid.

In Section 5.2.1 we have seen that in terms of  $\lambda$ ,  $T_m^{2D}$  scales as

$$T_m^{2D} \sim \frac{1}{\lambda^2}. \quad (5.8)$$

Furthermore the data represented here is all in the “logarithmic” interaction regime (Section 3.4.5). In this regime there is only one pertinent parameter; namely

$$\eta \frac{a_0}{\lambda} \sim \frac{\beta a_0}{\lambda^2 \gamma} \sqrt{1 + \ln \frac{\lambda}{d}}.$$

from which we have deduced that (keeping only the parameters that can vary)

$$T_m \sim \frac{\sqrt{1 + \ln \frac{\lambda}{d}}}{\sqrt{B} \lambda^2}. \quad (5.9)$$

Therefore, substituting 5.8 and 5.9 into 5.7 gives  $\zeta$  which then makes  $\Delta S$  scale as (using 5.6)

$$\Delta S \sim \frac{\sqrt{B}}{\sqrt{1 + \ln \frac{\lambda}{d}}}. \quad (5.10)$$

The solid line in Figure 5.26 is a fit to the scaling behaviour 5.10.

As the field further increases the entropy jump will increase until it saturates at the value for the two-dimensional melting, which is found to be  $\Delta S \simeq 0.28k_B$  (computed from both graphs on Figure 5.6).

Schilling *et al.* [33] measured the entropy jump in YBCO both by using the magnetization jump and by integrating the heat capacity peak. They found it to be constant between  $0.3k_B$  and  $0.6k_B$ , up to  $B = 8$  (T). Roulin *et al.* [74] found  $\Delta S$  to be between 0.2 and  $0.4 k_B$  with similar measurements, although on a crystal with twin boundary defects. More recently Bouquet *et al.* [47] measured  $\Delta S$  to be between 0.5 and  $1 k_B$  per pancake and falling to zero at the critical point at  $B = 10$  Tesla.

All those values of  $\Delta S$  are greater than ours by a factor of 10. Furthermore the decrease of  $\Delta S$  toward  $T_c$  in our simulation is not observed in experiments. On the other hand those values are comparable to our two-dimensional (or high field limit)  $\Delta S \simeq 0.28k_B$  per pancake. This may imply that fluctuations that have been neglected in this model play an important part in the observed transition. For instance the XY model accounts for the superconducting order parameter's phase fluctuations rather than just fluctuations of the vortex positions. Such a simulation of a three-dimensional system yielded an estimate for  $\Delta S$  of  $0.3k_B$  at  $B = 10$  Tesla [75], which is within the range of experiments and ten times bigger than what we observe with our model.

### 5.5.2 Field distribution (clean system)

We computed the thermally averaged magnetic fields for average fields between 0.1 and 5 Tesla and for various temperatures for our YBCO model.  $\lambda(T)$  was taken from [22] (Figure 3.2) and  $\xi(T)$  was set so as to keep  $\kappa = \lambda/\xi$  constant. The layer decimation procedure was *not* used (we fixed  $n = 1$ ) because the calculation of the field with virtual layers would

require assumptions that we do not want to make here<sup>4</sup>.

For each field value, a few simulations were made around the melting temperature  $T_m$  and eight more between  $T = T_m$  and  $T = 4$  Kelvin. The boundary conditions were left open in the  $z$  direction and the field was computed only on the central layer (see discussion on page 46). The resolution of the computed magnetic field was automatically adapted in order to be ten times smaller than the smallest lengthscale prediction  $\xi_{\text{eff}} = \xi^2 + \delta r^2$  (Equation 3.15). The root-mean-square position fluctuations  $\delta r$  was predicted through the formula  $\delta = 0.3\sqrt{T/T_c}$  which assume that the Lindemann number is 0.3 and that the fluctuations depends on the temperature as for a harmonic potential. This rough prediction guarantees that the resolution is sufficient to precisely resolve the high field cutoff under any condition. Furthermore the total number of Monte Carlo steps at which the field was computed in order to make the temperature averaging was adapted taking into account the above resolution so that the total time spent computing the field is a reasonable constant. This makes sense because we expect that for small fluctuations  $\delta r$ , for which the resolution is the highest, thermal averaging also requires a smaller sample. As a result the total number of averaging steps went from 20 for the lowest field and lowest temperatures to 320 at high temperature/field, for 5 to 44 hours of computation.

Figure 5.33 and 5.34 shows the magnetic field distribution obtained at each field for the eight points well in the solid phase. Figure 5.35 shows the evolution of the field distribution across the melting transition at  $B = 0.5$  Teslas.

Figure 5.30 shows observables for those simulations. In particular we computed the field's second moment

$$\langle B^2 \rangle \doteq \int n(B) B^2 dB$$

---

<sup>4</sup>We want the final field distribution to account for all variations of the field. If we used a coarse-grained version of the field it would neglect the intermediate field fluctuations due to the nearly-free wandering of the flux line on the neglected layers. The reason why we allowed ourselves to ignore those layers when studying the melting transition was that those fluctuations are small compared to  $a_0$  which is the pertinent lengthscale for this phenomenon. But here we are interested in the magnetic field distribution for which a pertinent lengthscale is the coherence length  $\xi$  which defines the size of the vortex cores and the high field cutoff value. At low fields the renormalization was most appropriate when studying the melting because the pancakes' fluctuations would get small compared to  $a_0$ . But in the same region those fluctuations in fact increase compared to  $\xi$  and therefore may have an important influence on the field distribution.

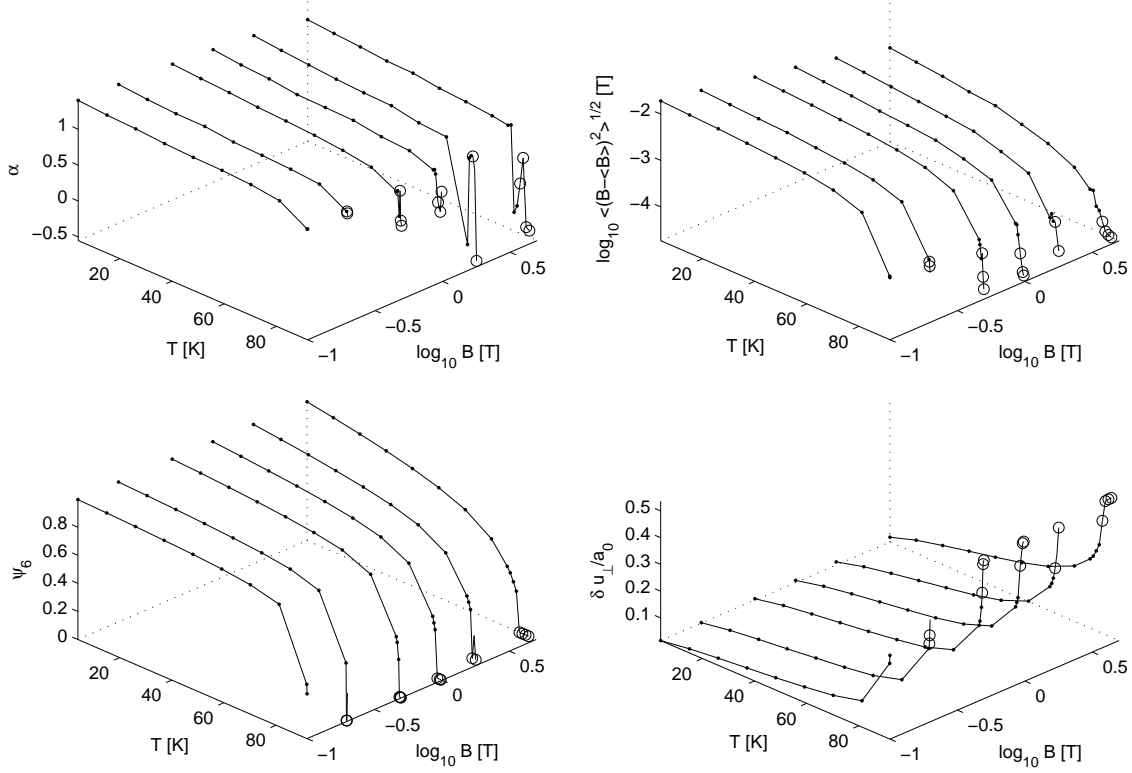


Figure 5.30: Observables associated with the simulations used to obtain the magnetic field distribution for the clean system (Section 5.5.2). The points designed by empty circles are fully in the melted phase, as shown by the suppression of the order parameter  $\psi_6$ . Only the eight lowest-temperature simulations for each field have been used for fitting of the field distribution. The field distributions obtained close to the transitions are of low quality because of the slow dynamics caused by the rapid increase of the number of layers and the proximity of the transition. The fluctuations of  $\alpha$  near melting are due to the fact that this parameter becomes undefined in the liquid phase (see text).

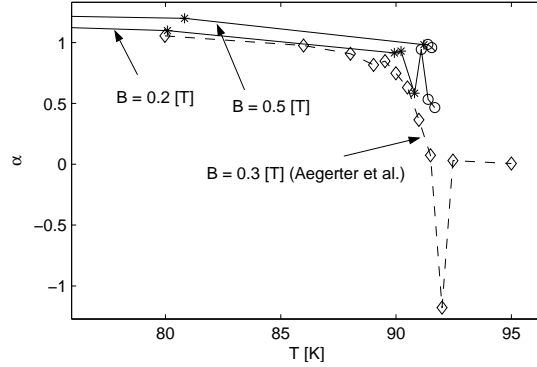


Figure 5.31: comparison between  $\alpha$  obtained in our simulation at  $B = 0.2$  (T) and  $B = 0.5$  (T) (solid lines), and the  $\mu$ SR measurements in Ref. [21] for YBCO, at  $B = 0.3$  Tesla. The stars are points obtained in the solid state and the circles are points obtained in the liquid phase. In our simulations the points obtained in the liquid phase are theoretically undefined and subject to fluctuations which depend on averaging issues (see text). On the other hand the experimental  $\alpha$  is generally lower and drops to a negative value at the transition. This is likely due to effects neglected in our simulation, like the macroscopic variations of the magnetic field near the edge of the sample [21], [14].

where we write  $B$  for  $B_z$ , the  $z$  component of  $\mathbf{B}$ . We neglect the other components (see discussion on page 43). We also show the skewness parameter as defined in expression 2.1. Because the liquid is characterized by perfect translation symmetry, the field distribution in the melted phase must average to a delta-function. Therefore both  $\langle B^2 \rangle$  and  $\langle B^3 \rangle$  must tend to zero and  $\alpha$  is undefined. This explains the strong fluctuations of  $\alpha$  for the few points computed in the melted phase (open circles in Figure 5.30). The sign of the skewness parameters  $\alpha$  has been used by Aegerter *et al.* [21] to experimentally decide, on the basis of the  $\mu$ SR lineshape, whether the flux lattice had melted. In our theoretical framework, nonetheless, this parameter is of little interest to characterize the melting. In a real experiments there are other factors beside the flux lattice contributing to the width of the  $\mu$ SR lineshape. When the field fluctuations related to the vortex lattice disappear, those other factors become important in shaping the observed distribution. In particular, the negative, or at least small skewness in the liquid phase can come from the crystal's edge

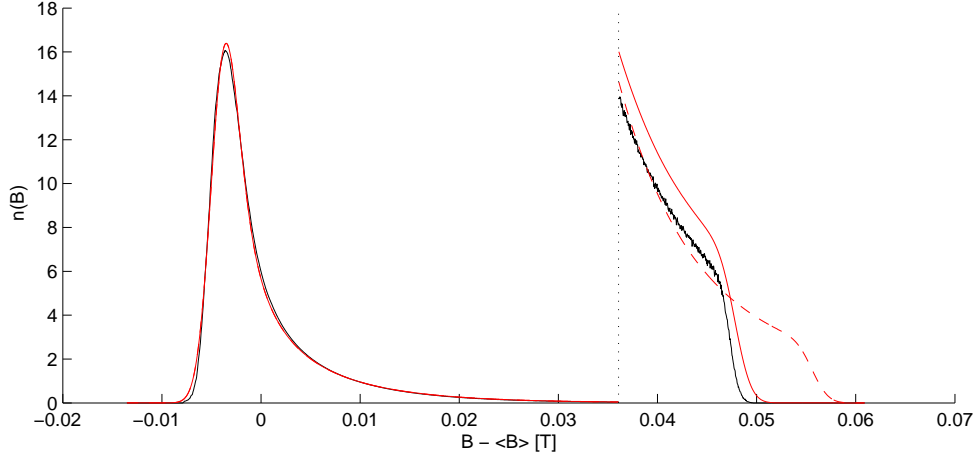


Figure 5.32: The black line is an example of field obtained from the simulation at  $B = 0.1$  (T) at  $T = 4$  (K) for the system with disorder. The high field tail is magnified. The vertical line delimits the magnified region. The red dashed line is a fixed point of the fitting procedure which consists in minimizing the distance between the two curves. The solid red line is a fixed point of the fitting procedure using the distance between the *magnified* curves. In fact the unmagnified distance to the simulation's curve is smaller also for the solid red line, showing that the dashed line is only a *local* minimum of the distance function. The parameters are  $\xi_{\text{eff}} = 14.49$  ( $\text{\AA}$ ),  $\lambda_{\text{eff}} = 1374$  ( $\text{\AA}$ ) and  $\sigma = 1.263\gamma_{\mu}$  ( $mT$ ) for the dashed red line and  $\xi_{\text{eff}} = 22.75$  ( $\text{\AA}$ ),  $\lambda_{\text{eff}} = 1373$  ( $\text{\AA}$ ) and  $\sigma = 1.264\gamma_{\mu}$  ( $mT$ ) for the solid red line.

effect [21] (Figure 5.31) as studied by Indenbom *et al.* [14] (see also Schneider *et al.* [51] for effect on the field distribution). Another factor can be the short scale field variations due to nuclear magnetic moments [13].

### On the fitting procedure

We fitted the simulation's field distribution with the model obtained from Equation 3.13, parameterized by  $\xi_{\text{eff}}$  and  $\lambda_{\text{eff}}$ , and convoluted with a Gaussian of weight  $\sigma/\gamma_{\mu}$  according to Equation 1.25. The fitting procedure consists in finding the global minimum of a *distance* between the parametrized curve and the distribution obtained with the simulation. The particular distance function  $\Delta$  to minimize depends on statistical assumptions. Here we

chose to minimize the Cartesian distance between the two distributions (say  $n_1(B)$  and  $n_2(B)$ ):

$$\Delta(\xi_{\text{eff}}, \lambda_{\text{eff}}, \sigma) \propto \int dB (n_1(B) - n_2(B))^2$$

This distance is left invariant by a Fourier transform. Therefore the distance between the two corresponding  $\mu\text{SR}$  lineshapes is essentially the same function.

We minimized  $\Delta$  using Matlab 6.5 *fminsearch* function which requires a starting point to be specified for the three parameters.

We noted that, at low fields, the method would converge to values which depend on the choice of initial values. Figure 5.32 shows two such fixed points of the fitting procedure. This is due to the fact that, at low field, the shape of the main peak depends very little on  $\xi_{\text{eff}}$ . The main dependance on  $\xi_{\text{eff}}$  is in the position of the peak, which can in turn be compensated by a slight change in  $\lambda_{\text{eff}}$ . In order for both parameters to be determined we need to take into account the details of what happens in the high field tail. Therefore we had to use another distance function  $\Delta$  where the tail is artificially weightened as on Figure 5.32. Specifically we chose to apply the magnification on the upper tier of the field region over which the distribution is non-zero and weightened the distance over this region by a factor equal to the ratio between the two parts' integrals (Figure 5.32).

## Fitting results

The fits in the solid phase are shown on figures 5.33 and 5.34. Figure 5.36 shows the results for the fitting parameters. The fitting procedure is described below.

Over the whole range probed, in the solid state,  $\lambda_{\text{eff}}$  is within 1% of  $\lambda$ . On the other hand the fitted coherence length  $\xi_{\text{eff}}$  reaches up to twice the value of  $\xi$ . Instead it matches very well the approximation computed from the RMS displacements  $\delta r$  assuming Gaussian fluctuations (Equation 3.15). For instance  $\xi_{\text{eff}}$  increases with decreasing  $B$  because the large spacing between vortices allows for larger fluctuations.

There are only two points at the highest field and highest temperatures where  $\lambda_{\text{eff}}$  diverges from the input value  $\lambda(T)$ . We see that this effect is accompanied by a notable deviation of  $\xi_{\text{eff}}$  from its value predicted from the pancakes RMS fluctuations. In fact this result is somewhat dubious given that a fit with  $\lambda_{\text{eff}}$  imposed equal to  $\lambda(T)$  gives a

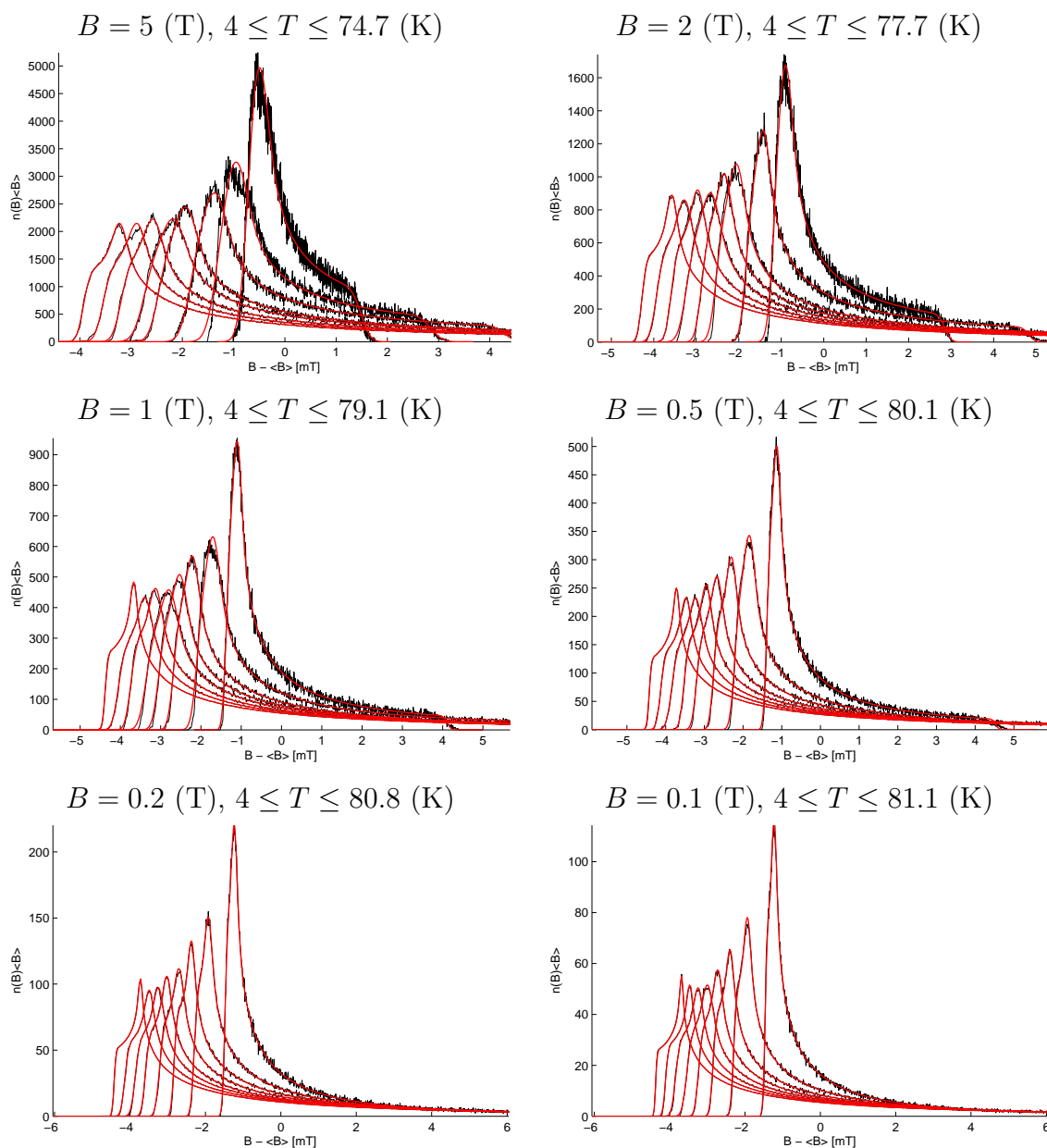


Figure 5.33: Field distribution obtained from the simulation (in black) and fits (in red). In each graph, the leftmost curve was obtained with the lowest temperature in the series, 4 Kelvin. The highest temperature was approximately 8 (K) smaller than the melting transition at each field. The lowest temperature was 4 Kelvin in each case. Those graphs include only simulations in the solid state. The upper field cutoff is not always visible on those graph; see Figure 5.34 for a zoom.

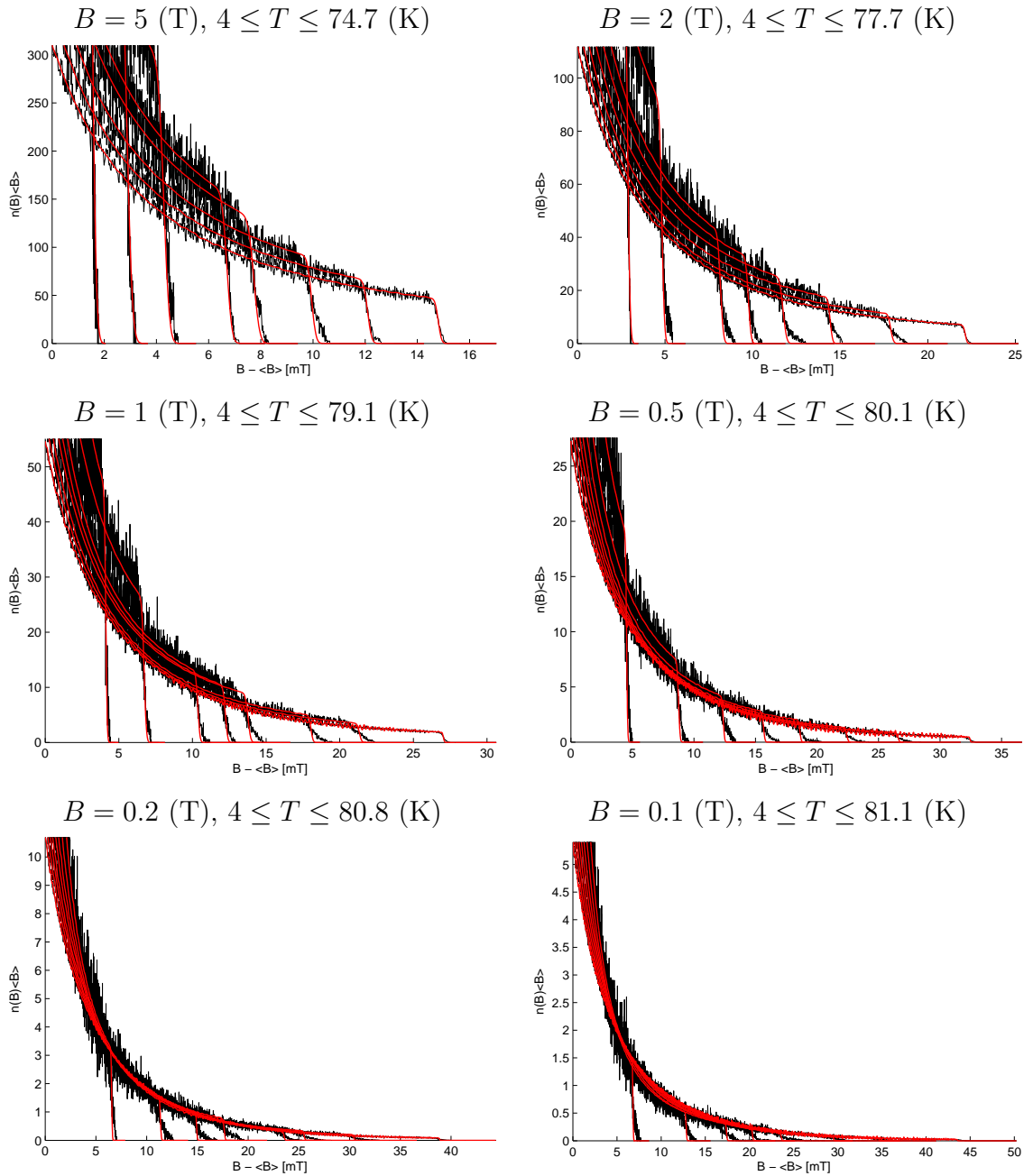


Figure 5.34: Zoom on the high field tail of the field distributions (on Figure 5.33) obtained from the simulation (in black) and fits (in red), respectively for  $B = 5, 2, 1, 0.5, 0.2, 0.1$  Tesla for the clean system. In each graph, the longest tail is that at the lowest temperature (4 Kelvin).

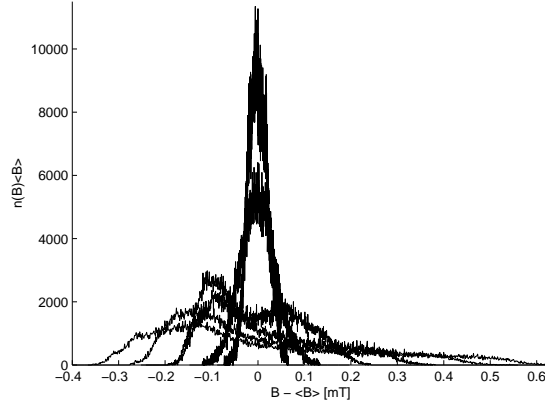


Figure 5.35: Magnetic field distribution across the melting transition at  $B = 0.5$  Teslas, for temperatures between 89.925 K and 91.682 K. The distributions are of bad quality because of the slow dynamics at the transition, and also because the low number of samples used in the averaging of the field becomes insufficient when the fluctuations are large.

result very close to the best fit compared to the fluctuations in the field distribution values (right graph on Figure 5.37). We do not know whether this effect is a real property of the fit, whether the fitting of such geometry is badly conditioned, or whether this is an error due the bad averaging of this field distribution as indicated by the visible noise. More simulations at high field would be needed to confirm this behaviour.

Let us try to make sense of those results. We have seen in Section 3.3.3 that under the “first-order” assumption that the individual pancakes fluctuates in an uncorrelated manner, and according to a Gaussian distribution, then there is *no way* to distinguish  $\xi$  from the RMS fluctuations  $\delta r$  if all that is given to use is the field distribution (or  $\mu$ SR lineshape). But it also means that this type of fluctuation is completely absorbed into  $\xi_{\text{eff}}$  so that, in this approximation, we should have  $\lambda_{\text{eff}} = \lambda$  and  $\sigma = 0$ . In fact our results show that this approximation is generally quite good for YBCO. The deviations from the approximation are seen in the non-zero value of  $\sigma$  as well as in the small deviations of  $\lambda_{\text{eff}}$  from  $\lambda$ .

The fact that for most of our values for  $\lambda_{\text{eff}}$  are within 1% of  $\lambda$  is in agreement with the fact the Sonier [8] obtained the correct  $\lambda$  at medium-high temperatures by fitting the

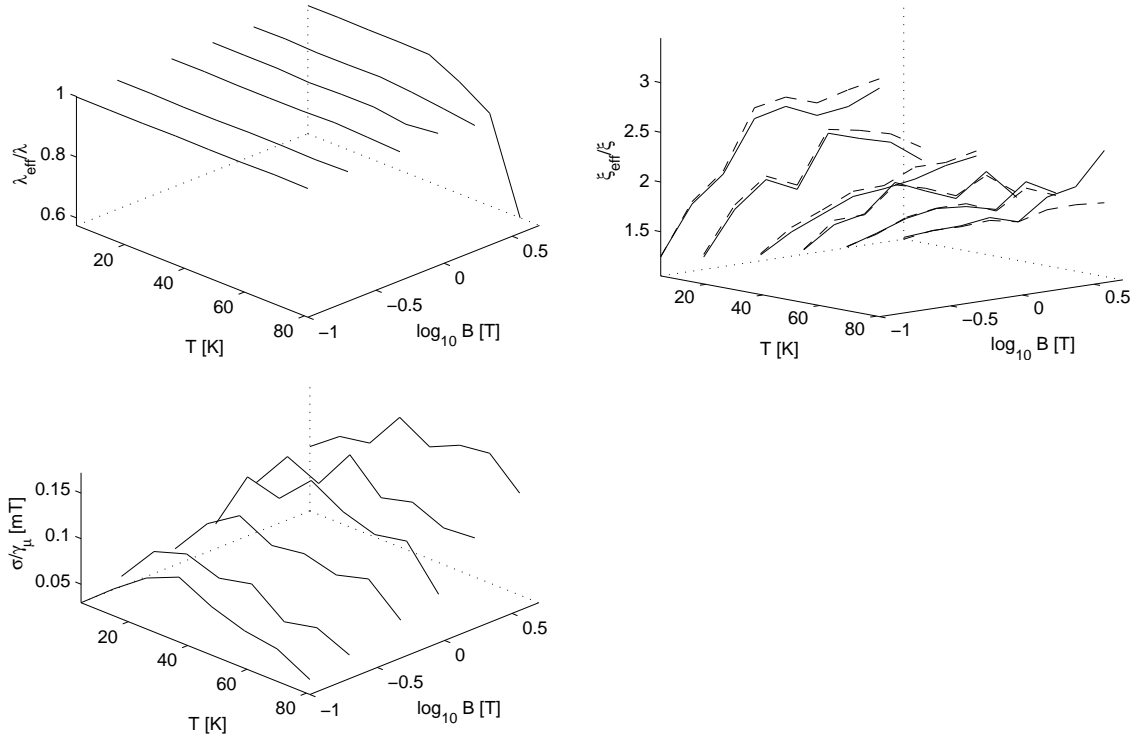


Figure 5.36: Result of fitting the simulation’s thermally averaged magnetic field by the distribution obtained with the simple model 3.13 and convoluted with a Gaussian of weight  $\sigma/\gamma_\mu$  (Equation 1.25), over a wide range of fields and temperatures, all in the solid phase, for our YBCO model. In the upper-left graph, the dashed line was computed from the RMS displacements  $\delta r$  obtained from the simulation, using Equation 3.15. The bottom-left graph is  $\sigma/\gamma_\mu$  relative to width of the field distribution.

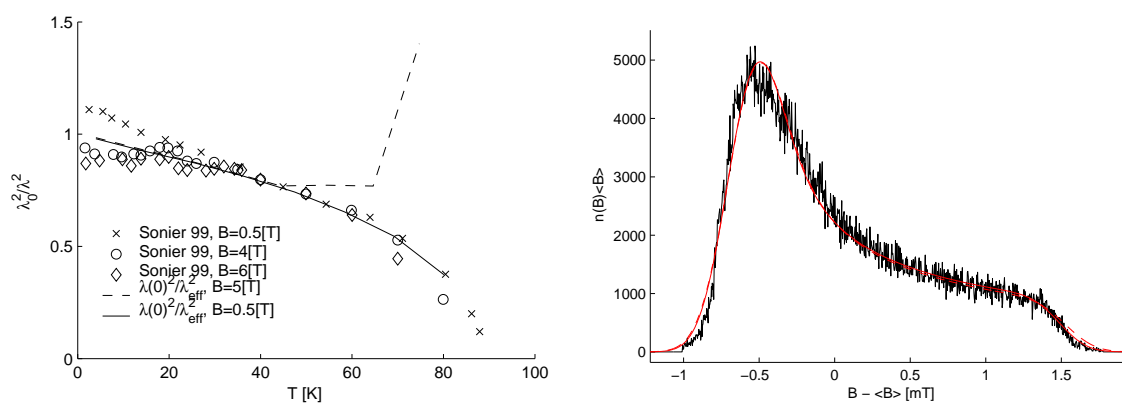


Figure 5.37: Left: Comparison between Sonier’s  $\mu$ SR measurement of the  $T$ -dependence of  $\lambda$  using  $\mu$ SR [8] and our prediction of what the method used should yield assuming the  $T$ -dependence of Figure 3.2 and taking into account the thermal fluctuations. Here we assumed  $\lambda_0 = 1200\text{\AA}$  for Sonier’s data. The strong deviation of the fitted  $\lambda_{\text{eff}}$  that we observe at high temperatures for  $B = 5$  (T) ( $T = 65.9$  and  $74.7$  (K)) is absent of Sonier’s data. Right: the fit giving rise to the strongly deviating point on the left graph (solid red line) as well as a fit with the correct  $\lambda$  constrained (dashed red line) (this is at  $B = 5$  (T) and  $T = 74.7$  (K)).

$\mu$ SR lineshape (Figure 5.37). Nevertheless this is not true of our two highest temperature points at  $B = 5$  (T) for which  $\lambda_{\text{eff}}$  strongly diverges. The second graph on Figure 5.37 shows that a distribution with  $\lambda_{\text{eff}} = \lambda$  gives a results very close to the best fit compared to the fluctuation in the simulation data. This indicates that the reason for the observed deviation may be a lack of iteration in the calculation of the magnetic field distribution in the simulation. Indeed this point is the closer to the transition than the other points and may suffer from a slower dynamics.



# Chapter 6

## Results II (dirty)

We implemented the disorder based on the presentation of Section 4.5. We focused on the system's low temperature behaviour because this is the relevant regime for the experimental observations of the vortex core expansion at low magnetic fields [18]. In order to reach an approximation of the ground state we performed naive simulated annealing in which we start from a system at *high enough* temperature (see below) and equilibrate it at successive steps of lower temperature until the target temperature is reached.

The initial temperature is high enough if the vortices are not pinned and can wander freely from one local minima of the disorder to another one. One way to be sure that this happens is to start in a phase where the system is melted. Then a value of the root-mean-square position displacements greater than the average vortex spacing as well as the disorder correlation length would indicate that the initial temperature was in fact high enough. Nevertheless if the pinning temperature is lower than the melting temperature one would take advantage of starting in the solid phase. Indeed a too rapid sweep over the transition may artificially freeze defects in the vortex lattice.

### 6.1 Decoupled layers

Like for the case with no disorder we chose to first try to have a handle on the simpler two-dimensional system of decoupled layers. In this case we chose to anneal the system starting from an initial temperature four times higher than the disorder landscape's root-mean-

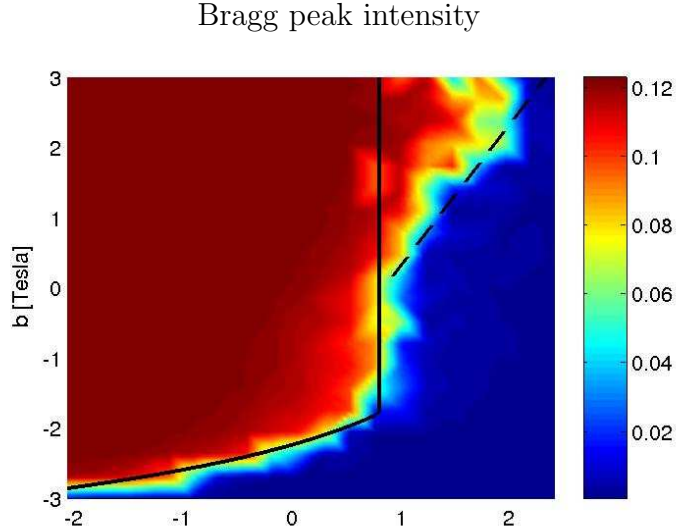


Figure 6.1: Bragg peak intensity as function of field and disorder strength for the two-dimensional system. The solid black line is obtained from the fit  $t(b)$  on the two-dimensional melting Figure 5.2 with the conversion  $\delta V(b) = t(b)/4$ . Because the temperature at which we started the annealing was  $t = 4\delta V$ , this means that on the left hand side of this curve the system started in an ordered state and on the right hand side it started from a disordered state.

square fluctuations  $\delta V$ . The temperature was decreased by equally-spaced steps down to  $\delta V/8$ , independently of the clean system's melting temperature. In addition averages were taken at a much lower temperature  $T = 10^{-13}(K)$ , which was potentially the lowest value of  $\delta V/8$  in our dataset. This essentially meant that we measured observables in a single final state of the system. What motivates the jump from  $T = \delta V/8$  to  $T \simeq 0$  is the assumption that the system has already reached the vicinity of the ground state at  $T = \delta V/8$ . This procedure was performed for 6 independent disorder realizations at each value of temperature and field.

The upper left graphs in Figure 6.1 shows the Bragg peak intensity at various combination of disorder strength and field. On the right hand side of the solid line the clean system would be melted were it to be at temperature  $T = 4\delta V$ , which is the temperature at which we started annealing the system. Figure 6.2 shows that at the chosen initial temperature

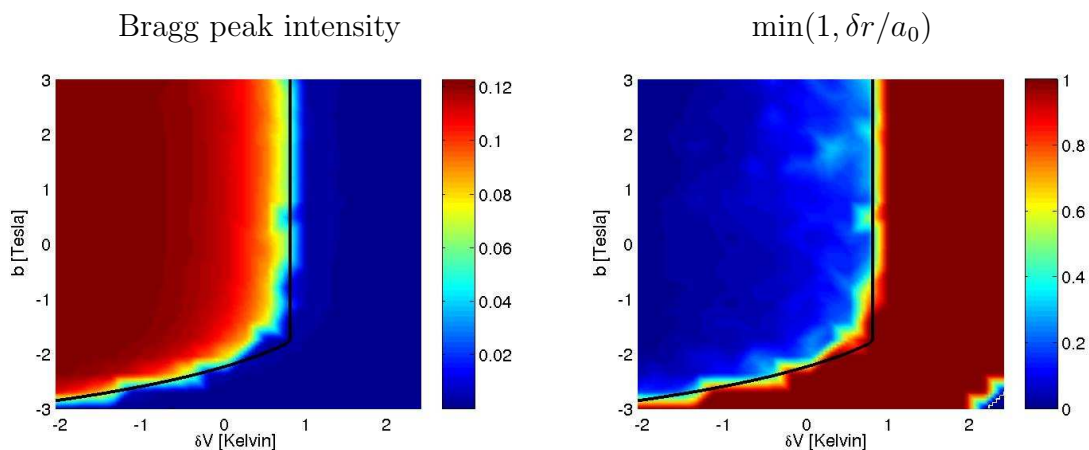


Figure 6.2: Bragg peak intensity and positions RMS fluctuations at the initial temperature  $T = 4\delta V$  before annealing. The small blue region on the bottom-right corner of the  $\delta r$  graph is an artifact (see Footnote on page 131).

the system has the same properties as the clean system at the same temperature and is likely not pinned, indicating that our initial temperature was high enough.

The ground state (Figure 6.1) at fields below 10 Teslas gets disordered at a disorder strength  $\delta V$  proportional to the clean system's melting temperature at that field, as shown by the solid line. Because of the proximity of the initial-temperature melting line, one could be led to think that the system was in fact already frozen in the initial state. But the root-mean-square fluctuations on Figure 6.2 show that under conditions where the ground state is disordered the initial state was *not* pinned. Indeed, for those points  $\delta r$  is always larger than the lattice spacing and the disorder correlation length, indicating that the pancakes were traveling freely<sup>1</sup>. Therefore the disordered ground states are *not* frozen instance of the initial state. Neither are the ordered ground states. Indeed, under the black line, one can see (Figure 6.1) that, for all fields, the annealing drove the system from a

<sup>1</sup>Except for one or two points on the lowest-right corner which are artefacts due to the extreme weakness of the lattice at such fields. In fact the temperature there was six orders of magnitude higher than the melting temperature, probably causing the pancakes to drift so far that their positions could not be stored adequately in floating point registers. This problem has been fixed in other simulations by maintaining the vortices inside the simulation box.

disordered to an order state, showing that the pinning happened at a temperature lower than the initial one.

At fields higher than 10 Teslas the linear relation between the clean-melting temperature and the “critical” disorder strength (at which our zero-temperature state loses hexagonal order) is no longer followed. The system becomes more robust to disorder as the field increases. In the logarithmic interaction regime ( $B > 0.1$  Teslas), we know that the interaction Hamiltonian 3.1 is effectively independent from  $B$  (because  $B$  matters only as  $a_0/\lambda \sim 1/\sqrt{B}$  and  $a_0/\lambda$  enter only the approximately logarithmic interaction potential which therefore factors out as an additive constant). Therefore the only parameter which varies with the field is the ratio between the inter-vortex spacing and the disorder correlation length (which is set equal to the coherence length  $\xi$ ):  $a_0/\xi$ . This number is always greater than one because both distances become comparable only at  $H_{c2} \simeq 600$  (T). But as the field increases  $a_0$  becomes closer to  $\xi$ .

What happens may be explained in the following way. At low fields, when  $a_0 \gg \xi$ , the probability to find a low value of the disorder potential is large even on a surface small compared to  $a_0^2$ . Therefore almost any configuration of the lattice can minimize the disorder potential. This is why the lattice gets pinned in the state it happens to have when annealed past the pinning temperature. At higher fields  $\xi$  is bigger relatively to the lattice’s typical length  $a_0$  and good minima of the disorder are more difficult to find. For instance, minimizing the disorder potential may require two pancakes to share the same local minima, which would go beyond the interaction energy the lattice is willing to pay. Therefore moderate displacements which would still break the lattice order are not favourable anymore in terms of gained pinning energy. Instead the lattice wins by minimizing the interaction energy and keeping the hexagonal order.

Let us be more precise. Clearly the freed pinning energy  $U_p$  must grow with the RMS displacements from the hexagonal lattice  $\delta r_0$ . For instance let us assume a power-law  $U_p \propto \delta r_0^\nu$ , with  $\nu > 0$ . Furthermore we can expect the freed pinning energy per pancake to be of the order of the disorder’s RMS fluctuations  $\delta V$  when  $\delta r_0$  is of the order of the correlation length  $\xi$ . Therefore

$$\frac{U_p}{\delta V} \simeq \frac{\delta r_0^\nu}{\xi^\nu}.$$

Also we know from the study of the clean system that in order to break the lattice we need

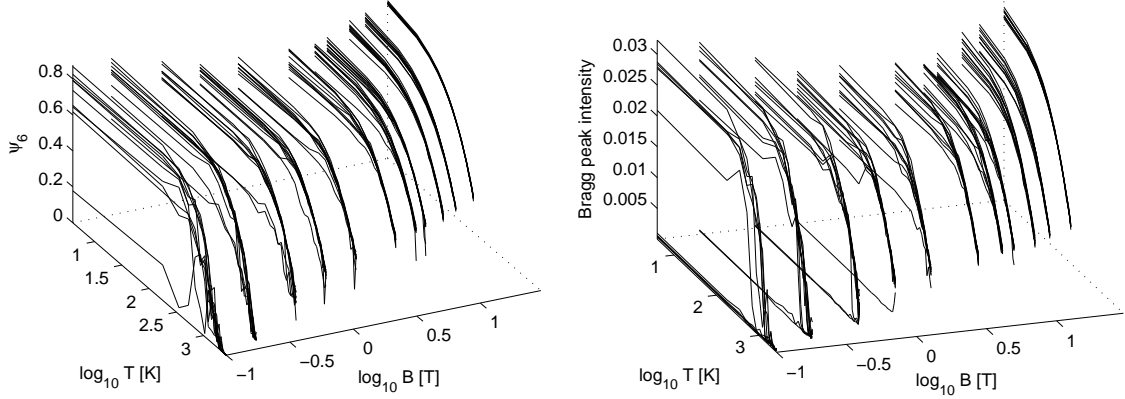


Figure 6.3: History of  $\psi_6$  and the Bragg peak intensity through annealing. Each lines corresponds to a different disorder realization. We see that some simulation have a zero  $\psi_6$  at low temperatures but a non-zero Bragg peak intensity. This is due to the fact that we monitor only the Bragg peaks commensurate with the simulation box. The too-rapid annealing seems to force certain states in an incommensurate quasi-hexagonal order as illustrated on Figure 6.8.

an energy of  $T_m^{2D}$  Kelvin per pancake (the clean melting temperature), which corresponds to fluctuations of the order of

$$\delta r_0 \simeq c_L a_0$$

where the Lindemann number is  $c_L \simeq 0.15$  (Figure 5.3). The system will become disordered at the value of  $\delta V$  for which both energies are equal:  $T_m^{2D} = U_p$ , which yields

$$\delta V = T_m^{2D} \frac{\xi^\nu}{(c_L a_0)^\nu}.$$

Therefore  $\delta V$  increases with the field  $B \sim 1/a_0^2$ . The dashed line on Figure 6.1 represents the above equation with  $\nu = 1$ .

## 6.2 The full dirty system

We performed simulations with the full three-dimensional systems and with a disorder parameters  $\delta_\alpha = 1/100$ , close to the one discussed in Section 3.2.1 for YBCO. This corresponds to RMS fluctuations of the disorder  $\delta V \simeq 60K$ . The system was equilibrated by

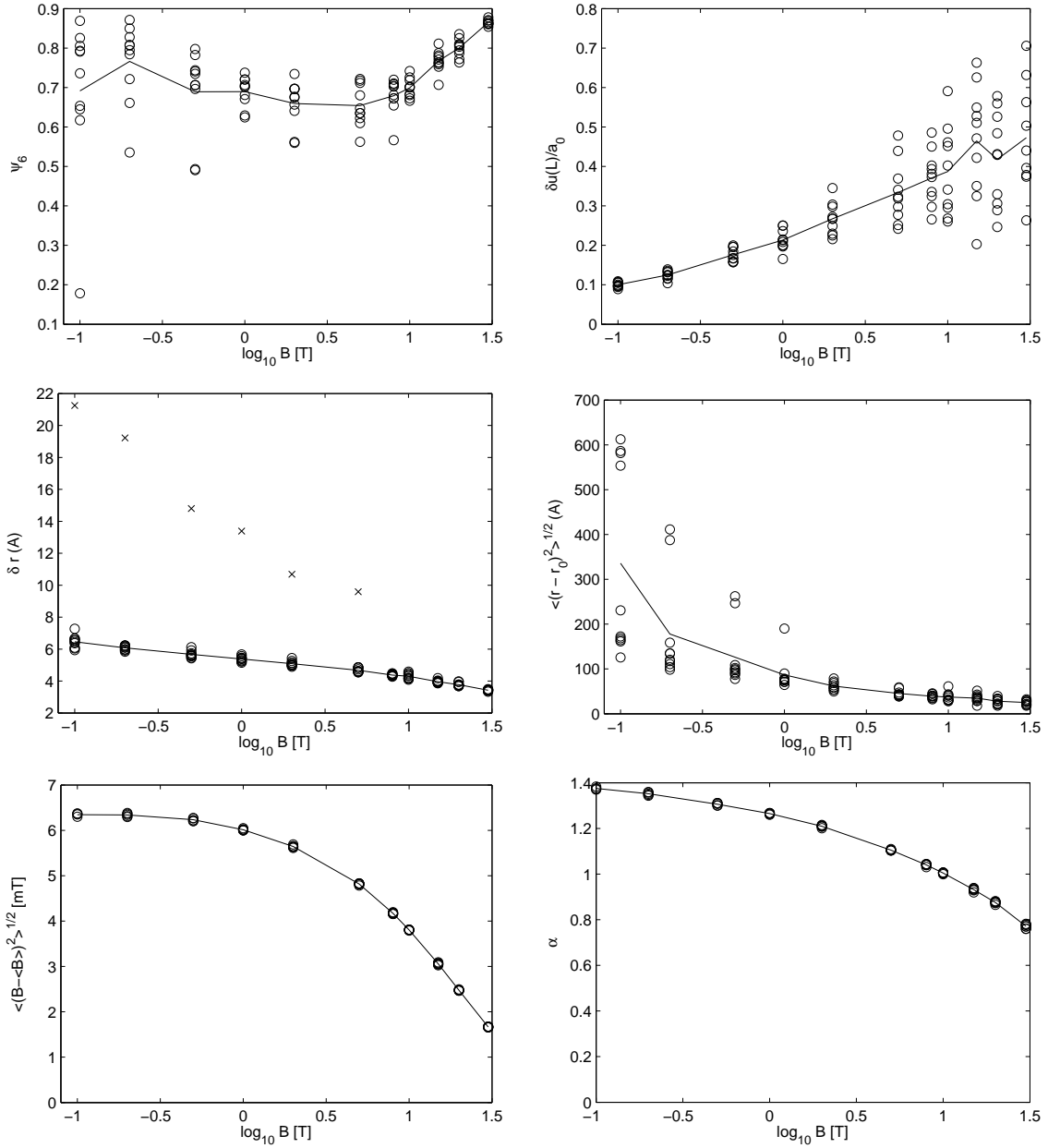


Figure 6.4: Observables for a simulation at  $T = 4$  (K) for YBCO with disorder  $\delta_\alpha = 1/100$  (Section 3.2.1), equilibrated by annealing from the clean melting temperature. The simulation cell contained 100 layers with periodic boundary conditions along  $z$ , and 64 pancakes per layer. The open circles are thermal averages for single disorder realizations. The solid lines are average over all 10 disorder realizations. The cross are the corresponding values for the clean system, from the results of Section 5.5. The middle-right graph represents the RMS fluctuations of the displacement of each pancakes away from its position  $r_0$  in an ideal hexagonal lattice. For the two bottom graphs, which refer to the field distribution, the solid line is not the average of the corresponding values for each disorder realization but instead the same property computed for the average distribution.

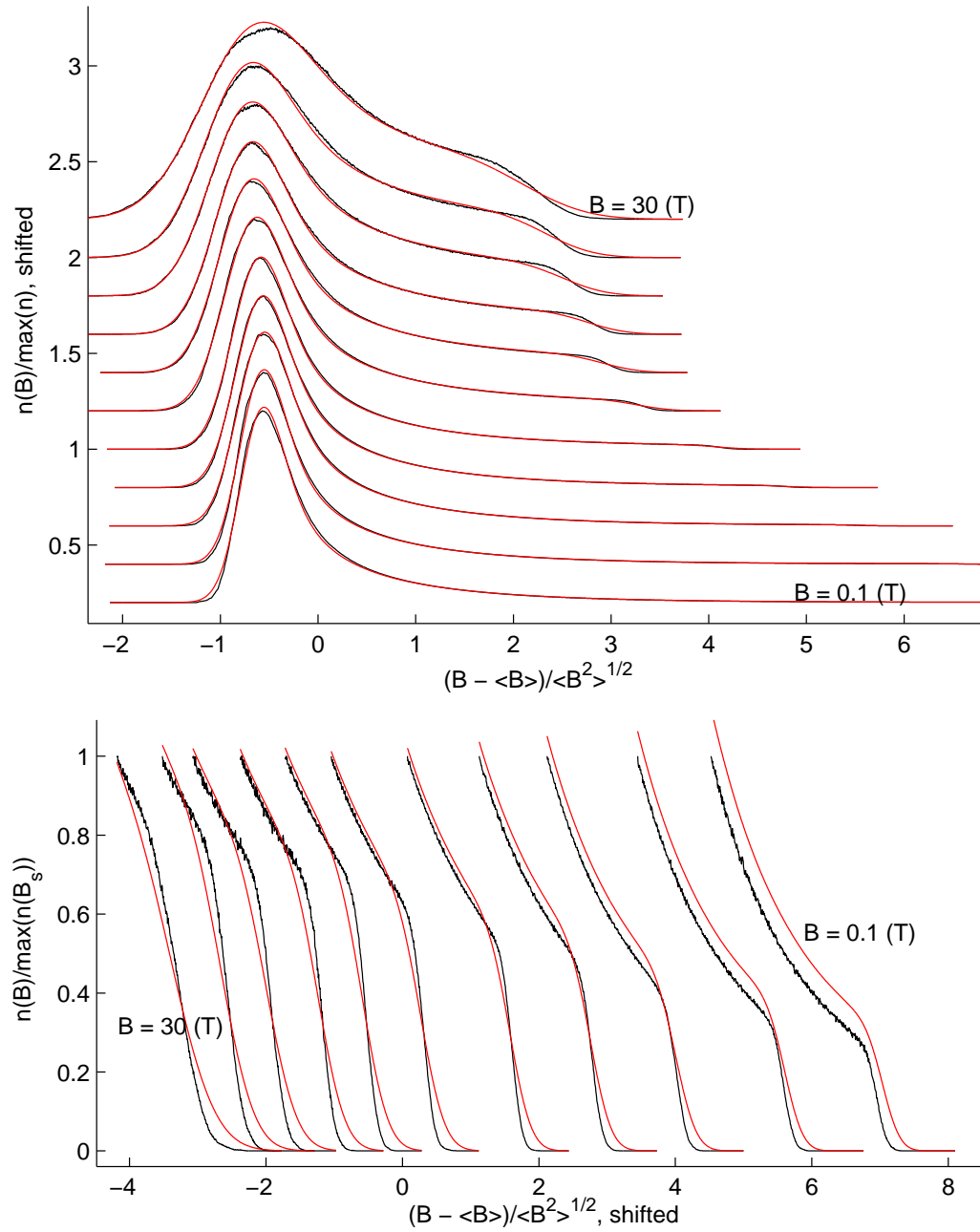


Figure 6.5: Magnetic field distribution for the dirty 3D system at  $T = 4$  (K) obtained from the simulation (black lines) and fits (red lines). Those distributions are averaged over 10 realizations of the disorder. The bottom graph is a zoom on the high field tails. Top: the top curve is for the highest field. Bottom: the leftmost curve is for the highest field.

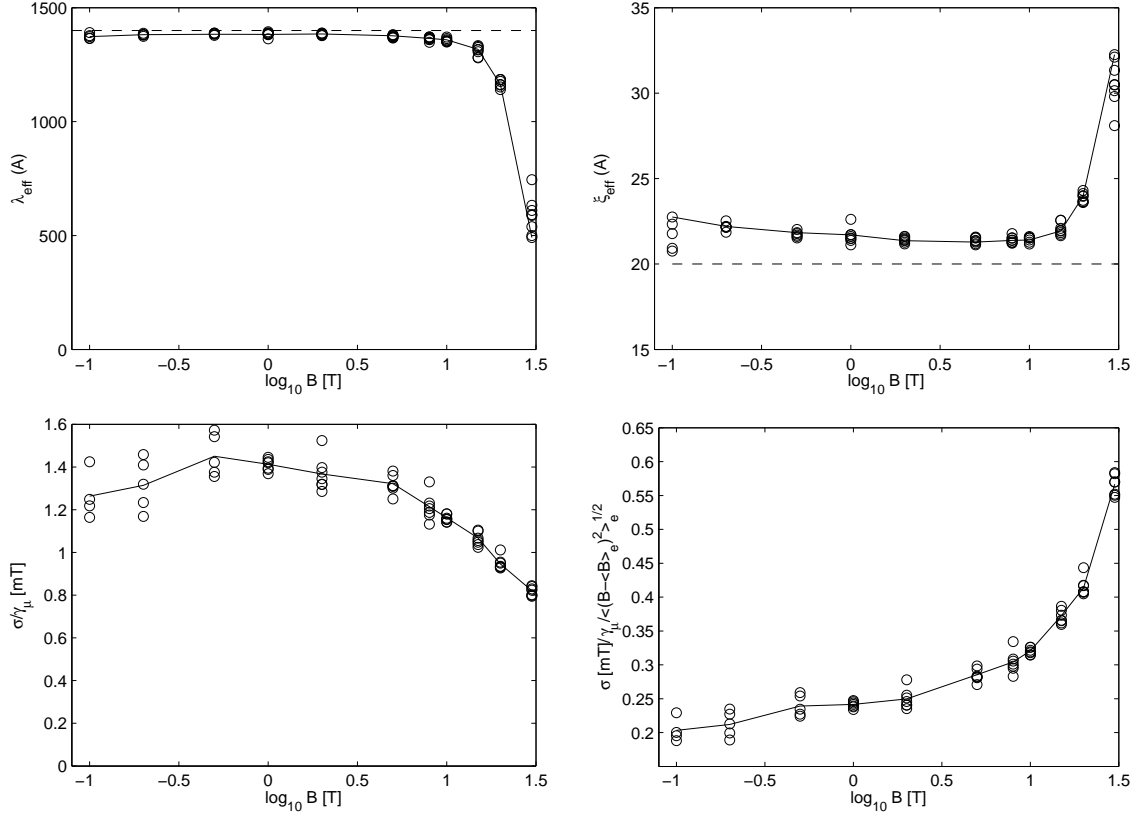


Figure 6.6: The three fitted parameters for the dirty system at  $T = 4$  (K). The points linked by a solid line are fits on the field distributions averaged over disorder. They correspond to the distributions shown on Figure 6.5. The circles are fits to independant disorder realizations. The horizontal dashed line represents the actual values of  $\lambda$  and  $\xi$  used in the simulation.

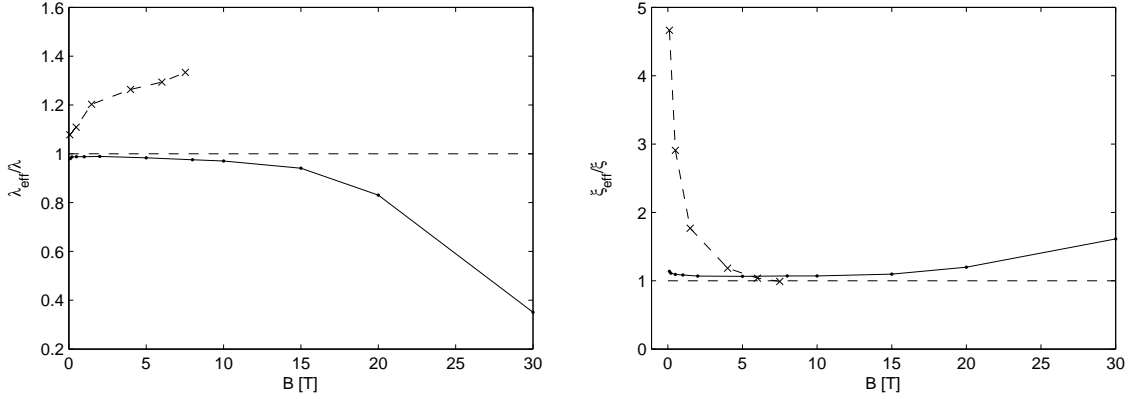


Figure 6.7: The crosses are respectively  $\lambda(B)/\lambda(0)$  and  $\xi(B)/(18.5\text{\AA})$  obtained by Sonier [8] by fitting experimental  $\mu\text{SR}$  lineshapes. The solid line are respectively  $\lambda_{\text{eff}}(B)/\lambda$  and  $\xi_{\text{eff}}(B)/\xi$  from our simulation, as on Figure 6.6.

simulated annealing starting from slightly above the clean system's melting temperature. We cooled the system from  $1.2T_m$  to 4 Kelvin through 30 equally spaced temperature steps with a total of  $10^6$  iterations (Figure 6.3). Also the annealing was performed with a constant field penetration depth  $\lambda$   $1400\text{\AA}$  (equal to the value for YBCO at small temperatures) and a constant coherence length  $\xi = 20\text{\AA}$ . The fact that we use a value for  $\lambda$  independent of temperature should be irrelevant provided that we reach equilibration at low temperature.

The data (Figure 6.4) are the result of averaging over an additional  $2 \cdot 10^5$  iterations at 4 (K). In addition the simulation has been run for 10 different realizations of disorder. For each disorder realization the magnetic field has been computed only on the final configuration, but taking into account the thermal fluctuations through each individual pancake's RMS position  $\delta r$  according to formula 3.14, a procedure justified by our analysis of the clean system. The average value of  $\delta r$  are reported on Figure 6.4. The RMS position fluctuation does not exceed  $\delta r$   $7\text{\AA}$ , which is small compared to the correlation length of the disorder  $\xi = 20\text{\AA}$  as well as the clean system's fluctuations at the same temperature (shown on the same graph). This indicates that the system is pinned.

The large value of  $\psi_6$  (Figure 6.4) shows that in all cases the lattice is mainly ordered,

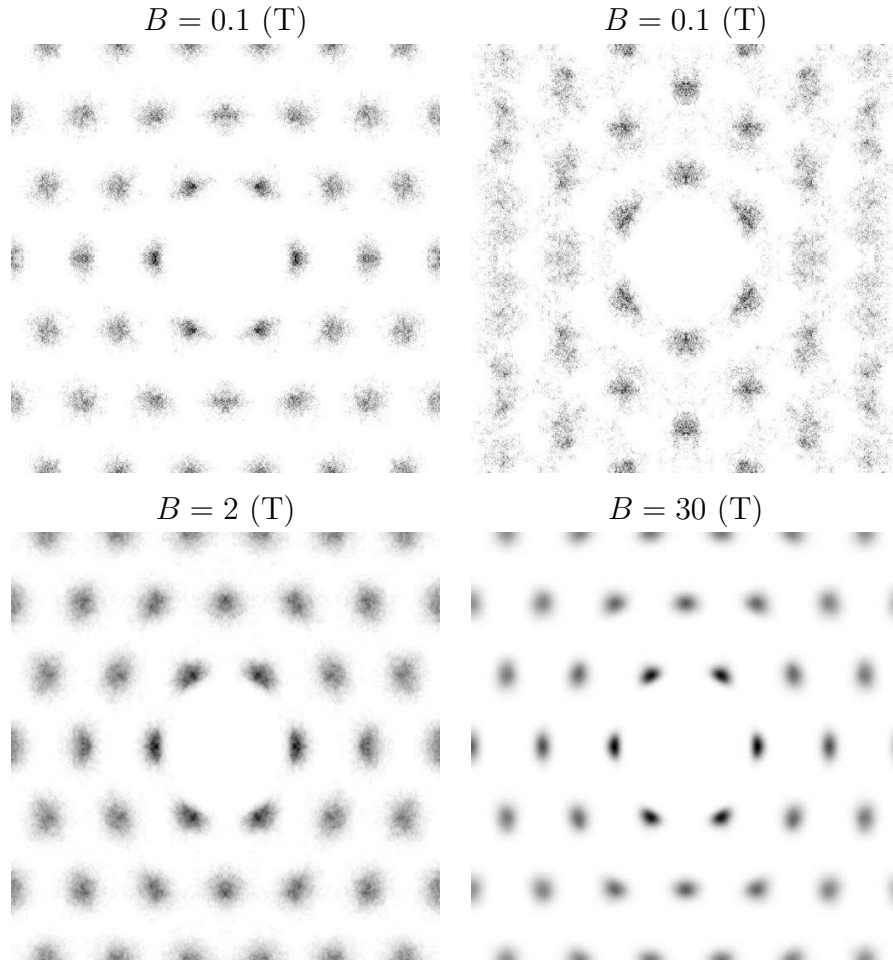


Figure 6.8: Pancake position correlation functions at  $T = 4$  (K) for the system with disorder and for a single disorder realization. The top-right figure shows a case where the system has ordered in a configuration which is not commensurate with the simulation cell's geometry, forcing the existence of defects.

as confirmed by position correlation functions (Figure 6.8).

Divakar *et al.* [29] observed a strong increase of the magnetic field variance at high external field for  $\text{La}_{1.9}\text{Sr}_{0.1}\text{CuO}_4$  that they relate to a transition to the vortex glass phase. The second moment of the field distribution (bottom-left on Figure 6.4) from our simulation, though, keeps decreasing as expected from the perfect in-plane ordering of our lattice at this regime. Indeed, position fluctuations along the  $z$  direction alone (which is all we have in the high field state of our simulation) cannot increase the distributions' width [27]. Interlayer pancake fluctuations on the other hand may increase the amplitudes of field fluctuations *between* layers but such fluctuations are neglectible because of the very large scale  $\lambda$  over which the field decays compared to the interlayer spacing  $d$  (see Section 3.3).

The fact that the order is increasing toward higher fields is suprising. We would have expected that the lattice becomes more fragile, as for the case of the clean system, because of the three- to two-dimensional crossover. However we see on Figure 6.4 that the line wandering  $\delta u(L)$  because so large as 70% of the average vortex spacing  $a_0$ , despite the increase in the hexagonal order parameter  $\psi_6$ . This shows that in this regime there are relatively large fluctuations between layers even though within each layer the order is perfectly maintained. Therefore the system finds itself in a situation dual to that encountered with the two-dimensional reentrant melting to an unentangled liquid. But here, instead of observing a correlation length in the  $z$  direction larger than the simulation box, we see a correlation length too large in the perpendicular direction.

This means that in this regime the layers can be considered as rigid lattices which are interacting between each other through an interaction 3.3 multiplied by the number  $m$  of pancakes per layer. Therefore, increasing the size of the simulation and adding more vortices in will renormalize the effective interlayer interaction by a factor proportional to the number of pancakes per layer. What would then be the state if the system was infinitely large? As more vortices are added to the system, the fluctuations  $\delta u(L)$  will decrease due to the stronger effective interlayer interaction resulting from the strongly coupled pancakes in a layer. One possibility is that in the limit of infinitely many vortices order wins and the lattice becomes as Bragg glass with no defects. The other possibility is that the pinning potential energy to be freed by shifting the layers with respect to each other will be strong enough to break the in-plane hexagonal lattice into independant domains.

Menon [76] proposed that the high field vortex glass phase is in fact a *domain glass* with solid-like domains. The defects separating domains in such a system can explain the experimentally observed field broadening [29]. If this theory applies to our system, then there is the likely possibility that our simulation box is in fact way too small to accommodate for the typical domain size.

### 6.2.1 Field distribution (dirty system)

We fitted each magnetic field distributions obtained from the simulation in the same way as for the clean system; with the field obtained from Equation 3.13, parameterized by  $\xi_{\text{eff}}$  and  $\lambda_{\text{eff}}$ , and convoluted with a Gaussian of weight  $\sigma/\gamma_{\mu}$  according to Equation 1.25. We also used the technique described in Section 10. The distributions and their best fits are shown in Figure 6.5. The agreement is always visually good, apart from the high field tail which is smoother than the model's one at high average fields.

The results of the fit are shown on Figure 6.6. Between 0.1 and 10 Teslas the fitted values of the coherence length and penetration depth are close to their actual values in the simulation. Also  $\sigma$  is typically 10 times larger than for the clean system (Figure 5.36). This is because most of the effect of thermal fluctuations was to increase  $\xi_{\text{eff}}$ . But this does not apply to static disorder and most of the effect of the static fluctuations is absorbed by  $\sigma$ .

Figure 6.7 shows a comparison between those results and the values obtained by Sonier [8] (Figure 2.1) by fitting experimental field distributions. On the region probed by Sonier the deviations due to the vortex lattice fluctuations are small compared to his results, showing that according to our model the convolution of the field distribution with a Gaussian sufficiently absorbs the effect of the thermal and static fluctuations.

Nevertheless we do observe a shift between  $\xi_{\text{eff}}$  and  $\xi$  which increases at low fields up to  $3\text{\AA}$ . This increase is not solely due to the thermal fluctuations ( $\delta r \simeq 6\text{\AA}$ , see Figure 6.4) which account only for an increase in  $\xi_{\text{eff}}$  of  $0.5\text{\AA}$  according to formula 3.15. The additional difference must be caused by the static fluctuations between neighbouring layers which effectively smears out the fields maximum at the pancake cores. This is essentially the effect predicted by Brandt in [27].

At fields much higher than 10 Teslas at which we seem to miss the experimentally

observed vortex glass, and despite the nearly perfect order of our lattice in that regime (Figure 6.4), we see strong deviations of  $\lambda_{\text{eff}}$  and  $\xi_{\text{eff}}$  from  $\lambda$  and  $\xi$ . This is linked to the bad quality of the fit at the high temperature cutoff (Figure 6.5). Indeed we see that the high field tail on the distribution from the simulation is much sharper than can be achieved by the fitting model given the large value of the Gaussian broadening  $\sigma$  which is needed for the smoothing of the saddle-point peak ( $\sigma/\sqrt{\langle B^2 \rangle} \simeq 60\%$  at the  $B = 30$  tesla.) We have seen that in this regime there is almost no relative fluctuations between pancakes in a same layer (small  $\psi_6$ ) but large fluctuations between pancakes in different layers (large  $\delta u(L)/a_0$  on Figure 6.4) The above result shows that those fluctuations between pancakes in different planes at high field cause a much larger smoothing of the distribution's peak than the high field tail. This trend is also true at lower field as can be seen on Figure 6.6. It is the opposite of what happens for thermal fluctuations (Figure 5.34) where the simulation's tail are typically less sharp than the fits.

This indicates that at fields such that  $a_0 \ll \lambda$ , the Gaussian broadening does not anymore serves its role of absorbing the effects of static fluctuations This may not be a concern in general as such fields are much higher than the one at which the vortex glass appears in YBCO. For BSCCO ( $\lambda \simeq 2000\text{\AA}$ ) or LSCO ( $\lambda \simeq 3000\text{\AA}$ ) such fields would be even higher than what can be experimentally probed.



# Chapter 7

## Conclusions

We developed a simulation with the aim to understand static and dynamic fluctuations of the magnetic flux lattice and their effect on the magnetic field distribution. No detailed studies of these effects have been done despite their strong importance in the data analysis of  $\mu$ SR experiments used to probe the underlying microscopic physics.

The simulation was developed based on a model by Ryu *et al.* [37]. We performed an extensive analysis of the regimes in which the model can be numerically explored, taking finite-size effects into account (Section 5.3). In addition we developed an approximation technique which extends the parameter space that can be numerically explored (Section 5.4). We also implemented an original algorithm for the calculation of the magnetic field in an arbitrary configuration of vortices, taking the vortex cores into account.

We first studied the melting of the model *without* disorder. We have partial evidence (Figure 5.11) that at high fields (when the interlayer RMS fluctuations reach  $\sim 25\%$  of the interlayer spacing: Figure 5.11) the melting happens together with a decoupling of the layers. The decoupling-melting is a first order transition (Figure 5.17). Because the melting temperature continues to decrease with increasing field, it must tend toward a two-dimensional field-independent melting of fully decoupled layers at  $T_m^{2D} \simeq 20$  Kelvin for YBCO (in general  $T_m^{2D} \simeq \frac{1}{155k_B} \frac{d\Phi_0^2}{2\pi\mu_0\lambda^2}$ , Section 5.2). The two-dimensional melting shows strong first-order scaling properties and no evidence that it follows the KTHNY theory [65] (figures 5.4 and 5.5), even though other simulations have shown that the finding of evidences for a KT transition may require much larger simulations (See Ref. [68] for hard

disks, or Ref. [69] for particles interacting through a Lennard-Jones potential).

The entropy jump associated with the two-dimensional melting is  $\Delta S \simeq 0.28k_B$  per vortex per layer (from the energy jump on Figure 5.6). This value decreases with decreasing fields as the correlation between layers increases. For instance the decoupling-melting transition on Figure 5.16 has an entropy jump  $\Delta S \simeq 0.18k_B$ <sup>1</sup>.

When the field is decreased below the decoupling crossover, the correlation length along  $z$  (parallel to the field, perpendicular to the layers) in the fluid largely increases, changing the decoupling melting to an *entangling* melting (Section 5.3). In this regime the melting temperature follows a simple scaling law (Section 3.4.5), in agreement with prediction from a continuum elastic theory of the vortex lattice (equation (5.3) in Ref. [56]). The simulations show that this law is still valid for the decoupling-melting when the transition temperature is far from the two-dimensional one (Figure 5.13). This melting temperature agrees with experiments on YBCO below the fields where disorder is believed to become important (Figure 5.22). On the other hand the entropy jump keeps decreasing with the increase in correlation length along  $z$  as the field decreases (Figure 5.26), in contradiction with experiments [33][47][74]. This contradiction casts serious doubts on the pertinence of the vortex-line model melting as an explanation for the observed first-order transition in YBCO. This may imply that fluctuations that have been neglected in this model play an important part in the observed transition. For instance the XY model yields a more plausible estimate of the entropy jump [75].

When the field is further decreased, past the limit where the intra-layer interaction 3.1 becomes exponential, a sample with a finite number of layers should undergo a reentrant melting to a non-entangled liquid, which is of the same nature as the two-dimensional melting (Figure 5.13). On the other hand, if the number of layers is infinite the situation is not so clear. Analytical theories predict a reentrant melting at low field [40]. But we found

---

<sup>1</sup>This value has been calculated assuming 20 layers, rather than 100. This data was originally meant to be interpreted as the melting of 100 layers, approximated with 20 layers, which means that  $\epsilon_0$  and  $\gamma$  were multiplied by  $n = 5$  compared to the parameters used. But we have seen that this value of  $n$  was too big for the approximation to be valid. Therefore this data can be interpreted in an alternative way; as a direct simulation of a system with renormalized values of  $\lambda$  (which makes up for  $\epsilon_0$ ) and  $\gamma$ . This means that such a system, at  $B = 5$  T, undergoes a decoupling melting with an entropy jump of  $0.18k_B$  per pancake.

no conclusive evidence for a reentrant melting in this limit, even with at a field 30 times lower than the limit at which the intra-layer interaction starts to weaken exponentially (Section 5.3.4). This is puzzling given that reentrance has been observed in the 2d boson model [72] which is identical to our model at low fields.

Our model is further shown to be inappropriate for the description of the low-field first-order transition in BSCCO (Figure 5.25). BSCCO is characterized by its extreme anisotropy ( $\gamma \simeq 50 - 250$ ) compared to YBCO ( $\gamma \simeq 5 - 9$ ). This makes its interlayer interactions much weaker. The first order transition temperature for BSCCO on the other hand is perfectly described based on a Lindemann criterion applied to the fluctuations of *independent* flux lines. Our model cannot account for this transition, probably because of the breakdown of the assumptions involved in the intra-layer interaction 3.1 (page 107).

From the study of the average magnetic field distribution in the clean system for parameters adapted to YBCO we concluded that over almost all of the range studied; from  $B = 0.1$  T to  $B = 5$  T and from  $T = 4$  K up to the melting temperature, the effect of thermal fluctuations is similar to an increase in the coherence length  $\xi$ , that is a broadening of the vortex core (Section 5.5.2, Figure 5.36). This means that whenever the effect of disorder can be neglected in the real system (for instance at sufficiently large temperatures),  $\mu$ SR experiments can provide a reliable value of  $\lambda$  (Figure 5.37) but a largely overestimated value of  $\xi$ .

Nevertheless our data may contradict this affirmation (about  $\lambda$ ) at the highest fields and close to the transition, in contradiction with experimental data from Sonier [8] (Figure 5.37). But our data in this regime are of poor quality compared to lower temperature. More simulations would be needed in order to reach a conclusion.

We then went on studying the same model with a disorder field based on an analysis of local critical temperature fluctuations as may be caused by oxygen vacancies [56].

At fields between 0.1 T and 10 T our model is predicted to be in the random manifold regime of the defectless Bragg glass state [46] (Section 3.2.1). At higher field we would have expected the system to enter a disordered vortex glass phase [3]. But in fact the in-plane order of our model increases (Figure 6.4). We have evidence that in this regime our simulation box is *not* large enough to show a qualitatively correct behaviour (page 140). Indeed the in-plane order increases despite strong fluctuations between layers. This

would not be possible if the layers were infinitely large because the collective interlayer energy would grow indefinitely with the system size. Nevertheless this indicates that if the infinite system is in fact disordered, it must be locally ordered over a lengthscale larger than our simulation box ( $L = 6a_0$ ).

At lower fields however, no such inconsistency is present. We concluded from our model that static and thermal fluctuations at low temperature (4 K) cause variations in  $\xi_{\text{eff}}$  and  $\lambda_{\text{eff}}$  in YBCO which are negligible compared to the variations observed by Sonier using  $\mu\text{SR}$  experiments [8] (Figure 6.7). Said differently, the effects of those fluctuations are correctly modeled by a convolution of the field distribution with a Gaussian. On the other hand there is the concern that at low fields, the value of  $\xi_{\text{eff}}$  is conditioned only by the high field tail of the field distribution which is extremely small. Our fitting procedure would not uniquely converge unless we applied an artificially big weight on the high field cutoff (Figure 5.32). It is difficult to imagine that such a small feature can be correctly resolved in an experiment.

## 7.1 Avenues for future work

Our conclusions concerning the magnetic field fluctuations all rely on the adequacy of our model [37] with our chosen parameters in the field and temperature ranges of interest. For YBCO our model is equivalent to the generally accepted vortex line model at fields below 30 Tesla (Section 3.4.2) and the melting temperature of our clean system matches experiments. Nevertheless the big discrepancy between the entropy jump at the transition in our model and the one measured in experiments is disturbing. Given that the XY model yields a much higher entropy jump, one may want to understand what is the nature of the neglected fluctuations which yield this discrepancy, and whether or not they would affect our results in the solid state. Also we are lacking a study of the finite-size scaling for the melting transition to an entangled liquid.

We have here focused on YBCO and attempted to model BSCCO as well, although we found that we could not model the experimental first-order phase transition observed in this material, perhaps due to its large anisotropy. We could try to apply our simulation to other high-temperature superconductors which have been studied with  $\mu\text{SR}$  experiments.

This is the case notably of  $\text{La}_{1.9}\text{Sr}_{0.1}\text{CuO}_4$  [19][29]. This material has an anisotropy  $\gamma \sim 20$  intermediate between YBCO and BSCCO which makes it an interesting case to consider.

Concerning the model with disorder we would like to reproduce evidence for a vortex glass at high fields, which includes the ending of the first-order melting transition [47], and the increase of the field fluctuation amplitudes [29]. Reproducing those results would be an important validation of our model and its capacity to correctly describe the magnetic field fluctuations in the Bragg glass region. We have seen that this would require to run simulations on much larger systems. We would first need to investigate how large the system should be, for instance using the work by Menon *et al.* [76]. Nevertheless, increasing the system size would be very difficult because of the rapid growth of computational burden.

Also there are uncertainties on the disorder model that we use. It was derived by Blatter *et al.* [56], based on local fluctuations of the  $\alpha$  and  $\beta$  entering the Ginzburg-Landau free energy (Equation 1.7). The magnitude of those fluctuations was derived on the hypothesis that they are caused by oxygen vacancies. Nevertheless those calculations are made on the basis of many approximations. Furthermore other sources of disorder may be important. Therefore we would also like to understand how the system's properties at large lengthscales depend on the microscopic disorder strength.



# Appendix A

## Multihistogram method, derivation

Here we derive Equation 4.1 with an original method based on Bayesian statistical inference. Before proceeding we present this approach.

### A.1 Bayesian statistical inference

Let us assume that we have a model of a stochastic process depending on some parameter  $\mu$ . We have a function  $f(x, \mu)$  giving the probability of an event  $x$  when the parameter  $\mu$  is given:

$$p(x|\mu) = f(x, \mu).$$

We would like to perform some experiments in order to infer what the parameter  $\mu$  is. The result of the experiment is a particular event  $x$ . Therefore, we would like to know what is the probability of a certain  $\mu$  when  $x$  is given, which is the converse of the what we have above. Probability theory tells us that

$$p(x|\mu) = \frac{p(x, \mu)}{p(\mu)}$$

and

$$p(\mu|x) = \frac{p(x, \mu)}{p(x)}$$

where  $p(x, \mu)$  is the joint probability. Therefore

$$p(\mu|x) = \frac{p(x|\mu)p(\mu)}{p(x)}.$$

If furthermore the event  $x$  is replaced by a series of  $N$  independent events  $x_1, \dots, x_N$  then we have

$$p(\mu|x_1, \dots, x_N) = \frac{\prod_i p(x_i|\mu)p(\mu)}{\prod_i p(x_i)}$$

$p(\mu|x_1, \dots, x_N)$  is what we want; the probability that a given  $\mu$  is the real physical value of the parameter given the series of events  $x_i$ . But we do not know  $p(\mu)$  nor  $p(x_i)$ . The term  $\prod_i p(x_i)$  is not important because it does not depend on our variable  $\mu$  and therefore is just a normalization factor. On the other hand the term  $p(\mu)$  is more subtle. It is known as the *a priori* distribution. The idea is that in general the final conditional probability should converge independently of our choice for  $p(\mu)$  when  $N \rightarrow \infty$  so that we can choose  $p(\mu)$  arbitrarily. Of course we do not want to set  $p(\mu)$  to zero for any possible value of  $\mu$ . In general a sensible choice is the uniform distribution  $p(\mu) \propto 1$ . With this choice  $p(\mu)$  also enters the global normalization factor. Therefore we are left with

$$p(\mu|x_1, \dots, x_N) \propto \prod_i f(x_i, \mu).$$

Now that we have this probability distribution we may want to find the parameter  $\mu$  which has maximal probability given our events  $x_1, \dots, x_N$ . In good conditions it would be given by solution to the equation

$$\partial_\mu \prod_i f(x_i, \mu) = 0.$$

A more general case is the one in which we have some constraint  $g(\mu) = 0$  on the possible values of  $\mu$ . In this case we will need to perform a constrained optimization with Lagrange multiplier  $\lambda$ :

$$\partial_\mu \left( \prod_i f(x_i, \mu) - \lambda g(\mu) \right) = 0.$$

In the case where there is no constraint we can rewrite the condition as

$$\sum_i [\partial_\mu \ln f(x_i, \mu)] \prod_j f(x_j, \mu) = 0$$

or simply

$$\boxed{\sum_i [\partial_\mu \ln f(x_i, \mu)] = 0} \quad (\text{A.1})$$

## A.2 Derivation

I now apply this techniques in order to derive Equation 4.1. For the simplicity of the exposition I will only consider the energy density of state  $\Omega(E)$ . The generalization is straightforward. Here our events  $x$ 's are particular realizations of the instantaneous energy  $E$  and inverse temperature  $\beta$  within a simulation run. The model is fully parametrized by the density of state  $\Omega$ . In order to avoid mathematical subtleties we assume that  $\Omega$  is discretized so that  $\Omega_i = \Omega(E_i)$  for some series  $E_i$ . Therefore our model only gives the probability of values of  $E$  within this series. The probability to obtain event  $E_K$  at temperature  $\beta$  is therefore

$$f(K, \beta, \Omega) = \frac{\Omega_K e^{-\beta E_K}}{\sum_i \Omega_i e^{-\beta E_i}}$$

Now Equation A.1 yields, for the derivation with respect to each  $\Omega_n$ ,

$$\sum_{is} [\partial_{\Omega_n} \ln f(K_{is}, \beta_s, \Omega)] = 0$$

where  $K_{is}$  codes for the fact that the event number  $i$  at temperature number  $s$  yielded energy  $E_{K_{is}}$ . Replacing  $f$  and  $g$  by their above expressions and simplifying yields

$$\sum_{is} \left[ \frac{\delta_{nK_{is}}}{\Omega_n} - \frac{e^{-\beta_s E_n}}{\sum_l \Omega_l e^{-\beta_s E_l}} \right] = 0.$$

Therefore

$$\Omega_n = \left[ \sum_{is} \delta_{nK_{is}} \right] / \sum_{is} \frac{e^{-\beta_s E_n}}{\sum_l \Omega_l e^{-\beta_s E_l}}$$

that we can rewrite as

$$\Omega_n = \left[ \sum_s n_s(E_n) \right] / \sum_s \frac{w_s e^{-\beta_s E_n}}{\sum_l \Omega_l e^{-\beta_s E_l}}$$

where we used the definition of the histogram for inverse temperature  $\beta_s$ :  $n_s(E_n) = \sum_i \delta_{nK_{is}}$  and its total number of steps  $w_s$ . This is a discrete version of expression 4.1.



# Bibliography

- [1] J. Bardeen, L. N. Cooper, and J. R. Schrieffer, *Phys. Rev.* **108**, 1175 (1957).
- [2] F. London, *Superfluids* (John Wiley and Sons, Inc., New York, 1950).
- [3] D. S. Fisher, M. P. A. Fisher, and D. A. Huse, *Physical Review B (Condensed Matter)* **43**, 130 (1991).
- [4] J. Ketterson and S. N. Song, *Superconductivity* (Cambridge University Press, The Edinburgh Building, Cambridge, UK, 1999).
- [5] Tinkham, *Superconductivity* (Robert E. Krieger Publishing Company, Krieger Drive, Florida, 1980).
- [6] V. G. Kogan, *Physical Review B (Condensed Matter)* **24**, 1572 (1981).
- [7] L. Krusin-Elbaum *et al.*, *Physical Review B (Condensed Matter)* **39**, 2936 (1989).
- [8] J. E. Sonier *et al.*, *Physical Review Letters* **83**, 4156 (1999).
- [9] J. L. Tallon *et al.*, *Physical Review Letters* **74**, 1008 (1995).
- [10] J. R. Clem, *Physical Review B (Condensed Matter)* **43**, 7837 (1990).
- [11] J. E. Sonier, J. H. Brewer, and R. F. Kiefl, *Reviews of Modern Physics* **72**, 769 (2000).
- [12] A. Schenck, *Muon Spin Rotation Spectroscopy: Principles and Applications in Solid State Physics* (Adam Hilger, Bristol, England, 1985).
- [13] J. E. Sonier, Ph.D. thesis, University of British Columbia, 1998.

- [14] M. V. Indenbom *et al.*, *Physica C* **222**, 203 (1994).
- [15] P. L. Gammel *et al.*, *Physical Review Letters* **59**, 2592 (1987).
- [16] J. R. Kirtley, V. G. Kogan, J. R. Clem, and K. A. Moler, *Physical Review B (Condensed Matter)* **59**, 4343 (1999).
- [17] T. M. Riseman *et al.*, *Physical Review B (Condensed Matter)* **52**, 10569 (1995).
- [18] J. E. Sonier, *J. Phys.: Condens. Matter* **16**, S4499 (2004).
- [19] R. Kadono *et al.*, *Physical Review B (Condensed Matter)* **69**, 104523 (2004).
- [20] J. E. Sonier *et al.*, *Physical Review B (Condensed Matter)* **61**, R890 (2000).
- [21] C. M. Aegerter *et al.*, *ArXiv Condensed Matter e-prints*, cond-mat/0305593 (2003).
- [22] W. N. Hardy *et al.*, *Physical Review Letters* **70**, 3999 (1993).
- [23] M. H. S. Amin, I. Affleck, and M. Franz, *Physical Review B (Condensed Matter)* **58**, 5848 (1998).
- [24] V. G. Kogan and N. V. Zhelezina, *Physical Review B (Condensed Matter and Materials Physics)* **71**, 134505 (2005).
- [25] .
- [26] E. Brandt, *Journal of Low Temperature Physics* **73**, 355 (1988).
- [27] E. H. Brandt, *Physical Review Letters* **66**, 3213 (1991).
- [28] M. Kohandel and M. J. P. Gingras, *ArXiv Condensed Matter e-prints*, cond-mat/0309091 (2003).
- [29] U. Divakar *et al.*, *Physical Review Letters* **92**, 237004 (2004).
- [30] .
- [31] E. H. Brandt, *Rep. Prog. Phys.* **58**, 1465 (1995).

- [32] D. R. Nelson, *Journal of Statistical Physics* (1989).
- [33] A. Schilling *et al.*, *Nature* **382**, 791 (1996).
- [34] E. Zeldov *et al.*, *Nature* **375**, 373 (1995).
- [35] K. Kadowaki and K. Kimura, *Physical Review B (Condensed Matter)* **57**, 11674 (1998).
- [36] L. P. Viana, E. P. Raposo, and M. D. Coutinho-Filho, *Physical Review B (Condensed Matter)* **70**, 134516 (2004).
- [37] S. Ryu, Ph.D. thesis, Edward L. Ginzton Laboratory, Stanford University, Stanford, California, 1994.
- [38] A. K. Kienappel and M. A. Moore, *Physical Review B (Condensed Matter)* **60**, 6795 (1999).
- [39] J. Kierfeld and V. Vinokur, *Physical Review B (Condensed Matter)* **69**, 024501 (2004).
- [40] G. Blatter, V. Geshkenbein, A. Larkin, and H. Nordborg, *Physical Review B (Condensed Matter)* **54**, 72 (1996).
- [41] H. Nordborg and G. Blatter, *Physical Review B (Condensed Matter)* **58**, 14556 (1998).
- [42] M.-C. Miguel and M. Kardar, *Physical Review B (Condensed Matter)* **62**, 5942 (2000).
- [43] A. M. Ettouhami, *Physical Review B (Condensed Matter)* **68**, 214510 (2003).
- [44] S. Ryu and D. Stroud, *Physical Review B (Condensed Matter)* **54**, 1320 (1996).
- [45] J. Yeo and M. A. Moore, *Physical Review B (Condensed Matter)* **65**, 144515 (2002).
- [46] T. Giamarchi and P. L. Doussal, *Physical Review B (Condensed Matter)* **52**, 1242 (1995).
- [47] F. Bouquet *et al.*, *Nature* **411**, 448 (2001).
- [48] T. Klein *et al.*, *Nature* **413**, 404 (2001).

- [49] T. Giamarchi and P. L. Doussal, *Physical Review Letters* **72**, 1530 (1994).
- [50] A. van Otterlo, R. T. Scalettar, and G. T. Zimanyi, *Physical Review Letters* **81**, 1497 (1998).
- [51] J. W. Schneider, S. Schafroth, and P. F. Meier, *Physical Review B (Condensed Matter)* **52**, 3790 (1995).
- [52] M. Feigel'man, V. Geshkenbein, and A. Larkin, *Physica C* **167**, 177 (1990).
- [53] O. Waldmann *et al.*, *Physical Review B (Condensed Matter)* **53**, 11825 (1996).
- [54] M. Tinkham, *Helv. Phys. Acta* **61**, 443 (1988).
- [55] G. J. Dolan *et al.*, *Physical Review Letters* **62**, 827 (1988).
- [56] G. Blatter *et al.*, *Reviews of Modern Physics* **66**, 1125 (1994).
- [57] L. P. Gor'kov, *Sov. Phys. JETP* **37**, 998 (1960).
- [58] A. Larkin, *Sov. Phys. JETP* **31**, 784 (1970).
- [59] D. E. Farrell *et al.*, *Physical Review Letters* **64**, 1573 (1990).
- [60] J. D. Jorgensen *et al.*, *Physical Review B (Condensed Matter)* **36**, 3608 (1987).
- [61] G. I. Menon, C. Dasgupta, and T. V. Ramakrishnan, *Physical Review B (Condensed Matter)* **60**, 7607 (1999).
- [62] D. R. Nelson, *Physical Review Letters* **60**, 1973 (1988).
- [63] A. M. Ferrenberg and R. H. Swendsen, *Physical Review Letters* **63**, 1195 (1989).
- [64] S. W. Sloan and G. T. Houlsby, *Advanced Engineering Software* **6**, (1984).
- [65] K. J. Strandburg, *Reviews of Modern Physics* **60**, 161 (1988).
- [66] N. D. Mermin and H. Wagner, *Physical Review Letters* **17**, 1133 (1966).

- [67] M. Plischke and B. Bergersen, *Equilibrium Statistical Physics, Physical and Life Sciences* (Prentice Hall, Englewood Cliffs, New Jersey, 1989).
- [68] A. Jaster, Physical Review E (Statistical Physics, Plasmas, Fluids, and Related Interdisciplinary Topics) **59**, 2594 (1999).
- [69] K. Chen, T. Kaplan, and M. Mostoller, Physical Review Letters **74**, 4019 (1995).
- [70] K. Binder, Rep. Prog. Phys **50**, 783 (1987).
- [71] J. Lee and J. M. Kosterlitz, Physical Review B (Condensed Matter) **43**, 3265 (1991).
- [72] L. Xing, Physical Review B (Condensed Matter) **46**, 11084 (1992).
- [73] B. Davoudi and M. Kohandel, Physical Review B (Condensed Matter) **61**, 14727 (2000).
- [74] M. Roulin, A. Junod, A. Erb, and E. Walker, Physical Review Letters **80**, 1722 (1997).
- [75] R. E. Hetzel, A. Sudbo, and D. A. Huse, Physical Review Letters **69**, 518 (1992).
- [76] G. I. Menon, Physical Review B (Condensed Matter) **65**, 104527 (2002).

# Index

- $\mu$ SR lineshape, 16
- 2D boson model, 26
- Abrikosov, 10
- BCS, 22
- Bessel function, 8, 9
- bilinear interpolation, 70
- Bitter decoration experiments, 22
- Boltzmann ensemble, 61
- Bragg glass, 39
- canonical momentum, 4
- carriers, 4
- Cartesian distance, 121
- coexistence region, 78
- coherence length, 1, 6
- complex order parameter, 4
- Cooper pair, 23
- copper-oxide planes, 13
- current density, 5
- d-wave, 23
- decay, 15
- defects, 35
- density of carriers, 4
- depolarization, 17
- discretization, 70
- disorder potential, 38
- distance, 120
- domain glass, 140
- energy gap, 23
- energy landscape, 36
- entangle, 87
- entangled liquid, 89
- even, 69
- external magnetic field, 4
- extreme type II, 6
- field penetration depth, 1
- flux line lattice, 9
- flux quantization, 7
- fluxoid quantum, 7
- free energy, 4
- gauge, 4
- generic phase diagram, 12
- Ginzburg-Landau equations, 5
- ground state, 4, 9, 10
- Hankel function, 8
- hard-sphere, 75
- hexagonal lattice, 10

hexatic phase, 75  
hysteresis, 78  
isotropic superconductor, 15  
Josephson effect, 13  
Josephson healing length, 34  
KTHNY, 75  
lattice constant, 10  
Lawrence-Doniach Model, 13  
Lennard-Jones, 75  
lifetime, 15  
Lindemann criterion, 26  
Lindemann number, 107  
line wandering, 88  
London equations, 3  
London gauge, 4  
lowest critical field, 12  
magnetostatic, 3  
Meissner effect, 3  
Meissner phase, 11, 12  
melting, 26  
Mermin-Wagner-Hohenberg theorem, 74  
Metropolis algorithm, 61  
microscopic assumptions, 5  
mixed phase, 11, 12  
Monte Carlo step, 61  
multihistogram method, 82  
muon gyromagnetic ratio, 17  
Muon Spin Rotation, 15  
neutrinos, 15  
NMR, 22  
nodes, 23  
Nuclear Magnetic Resonance, 22  
number of virtual layers, 50  
Ohm's law, 3  
open boundary conditions, 46  
oxygen vacancies, 35  
pancake, 9  
pancakes, 13, 14  
penetration depth, 4  
periodic boundary conditions, 46  
pile, 9, 15  
piles, 14  
pinning centers, 36  
point defect, 36  
positron, 15, 16  
quantum, 4  
quasi long-range order, 75  
random field, 36, 38  
reciprocal vectors, 69  
reconnection, 90  
reconnection moves, 61  
relative displacement, 39  
renormalization, 50  
repulsive interaction, 9  
resistivity, 3  
s-wave, 22  
SANS, 21

skewness, 26, 119  
Small Angle Neutron Scattering, 21  
STS, 22  
Superconductivity, 3  
Surface Tunneling Spectroscopy, 22

thin film, 75  
three-dimensional liquid, 89  
time series, 63  
transition, 4  
type I superconductors, 6  
type II superconductors, 6

unentangled liquid, 87  
upper critical field, 12

vector potential, 4  
vortex, 8, 9  
vortex core size, 22  
vortex line, 9

weakly pinned flux lattice, 39